STRUCTURAL CHARACTERISATION OF APATITE-LIKE MATERIALS

JIANGLING LI

A thesis submitted to the School of Metallurgy and Materials for the degree of

MRes in Biomaterials

Supervisor: Dr. A. Stamboulis

College of Engineering and Physical Sciences, University of Birmingham, UK

October 2009

Abstract

Hydroxyapatite (HA) is an important material for biomedical applications and has found application as bone substitute and implants coating due to the high similarity to the inorganic material of bone and tooth. Usually the HA lattice in living organism is substituted by different cations in order to help maintaining a normal metabolism. Once the type of substitution or substitution concentration is below or beyond the required level, severe problems may subsequently occur. Therefore, it is a great importance to understand the effect of different substitutions on the HA structure as well as the substitution levels in the HA structure.

In this work, the effect of ionic substitutions of Zn^{2+}, Mg^{2+}, Sr^{2+}, Si/ SiO_4^{4-}, and CO_3^{2-}, on the HA structure was studied. Emphasis was given to changes in the crystallite size and crystallinity of apatite samples produced by three different methods: chemical precipitation method, hydrothermal method, and bacterial biosynthesis. A general observation was that all samples contained a certain amount of CO_3^{2-}, HPO_4^{2-}, and in some cases residual nitrates depending on the method of synthesis. The presence of CO_3^{2-} is particularly interesting because it seems that CO_3^{2-} can easily be present in the apatite lattice replacing either OH^- and/or PO_4^{3-}. XRD, FTIR, Raman and ^{31}P MAS-NMR spectroscopy in Zn-HA (S7) and Si-HA (S8-S12) did not show strong evidence of Zn and Si substitution in the apatite lattice most likely because the concentration of Zn and Si was very small in the above mentioned samples. On the other hand, in the case of Mg substitution from 0.7 to 9.1 wt%, the information received by XRD, FTIR, Raman and ^{31}P MAS-NMR spectroscopy was valuable suggesting that 0.7 wt% Mg substitution did not cause strong effect on the apatite structure but a phase transformation from HA to Mg-whitlockite was favoured at and above 1.6% of Mg substitution (S2-S4). Sr substitution was easier (S15-S19) and incorporation of Sr into the apatite lattice was complete at 100 mol% Sr substitution. Rietveld analysis confirmed that substitution of Sr for Ca in the apatite lattice resulted in an increase in

the lattice parameters a and c. Interestingly small Sr-HA crystallite size was measured when Sr substitution reached 50 mol%, whereas the largest crystallite size was measured once the Sr substitution reached 100 mol%. In the case of CO_3^{2-} substituted HA samples (S13-S14), increasing CO_3^{2-} substitution from 0 to 21 wt% resulted in a decrease of the crystallite size from 42 to 16 nm, and formation of $CaCO_3$ was observed in the case of S14, when CO_3^{2-} reached 21 wt% substitution. The bacterially derived biological HA (S20) contained both A- and B-type CO_3^{2-} due to the bio-mineralisation process during the biological synthesis. The biological HA exhibited the smallest crystallite size (8 nm) and lower degree of crystallinity compared to the other HA samples.

Acknowledgments

I would like to especially thank my supervisor, Dr. Artemis Stamboulis, who gave me tremendous academic support and constant encouragement during the whole period of time of my Master project. This included guiding of the project direction, discussing the project work, and checking English grammars.

Sincere thanks are given to the project collaborator, Dr. Jawwad Darr's group, Department of Chemistry, The London's Global University, for providing 14 synthetic apatite samples and other relevant information.

Sincere thanks are also gone to Dr. K. Natalia and Dr. R. Law, Department of Materials, Imperial College London, for their kindly helping with operating the ^{31}P MAS-NMR technique.

Special thanks are given to Dr. Adrian Wright, Department of Chemistry, University of Birmingham, for helping with the Rietveld analysis on the 25 mol% Sr substituted HA sample.

Acknowledgements are given to Mr. Frank Biddlestone, who gave me the demonstration of FTIR experiment procedures.

Last, I'd like to deeply thank my fiancé, who gave me so much support and understanding, during the whole period time of my thesis writing.

Abbreviations and Symbols

$Ca_{10}(PO_4)_6(OH)_2$ or HA	Hydroxyapatite
$Ca_{10}(PO_4)_6F_2$ or FAp	Fluorapatite
CDHA	Calcium deficient hydroxyapatite
°C	Degree Celsius
c	Velocity of light in a vacuum $= 2.998 \times 10^8$ ms^{-1}
DCPA	Dicalcium phosphate anhydrous
DFT	Density function theory
DI	Distortion index
E_a	Activation energy
f	Frequency of vibration
G2P	Glycerol 2-phosphate
g	Gram
h	Hour
k	Bonding force constant
k	Reaction rate constant
nm	Nanometer $= 10^{-9}$ m
Pa or p. s. i.	Pascal $= 1$ N/m^2
P	Inorganic phosphate
T	Temperature
TEOS	$Si(OCH_2CH_3)_4$
TCP	Tricalcium phosphate
β-TCP	β- Tricalcium phosphate
μ	Reduced mass of two bonding atoms
μm	Micrometer/ Micron $= 10^{-6}$ m

Contents

List of Figures

List of Tables

1. Introduction

1.1. Synthetic hydroxyapatite

Hydroxyapatite [$Ca_{10}(PO_4)_6(OH)_2$, HA] has attracted much attention, since it is similar to the inorganic phase of bones and teeth [1]. Therefore, using as biomaterial, it exhibiting excellent biocompatibility, good bioactivity, and osteoconductivity [2], but poor mechanical properties [3].

To compare with conventionally crystalline HA, the nano-crystallized HA exhibited great biological efficacy [4], which included promoting osteoblast adhesion, proliferation, ossteointegration, and the deposition of calcium-containing mineral on its surface. Additionally, *Webster and co-workers* indicated that nano-sized HA showed better bioactivity than the coarser ones [5]. Moreover, *Bose and co-workers* believed that nano-sized HA ceramics can improve the sintering kinetics and subsequently enhance mechanical properties, since its higher surface area [6]. As a result, a large effort has been focused on the synthesis of nano-sized HA powders [7].

1.1.1. Synthesis and morphology of HA

Numerous of routes have been applied to prepare HA material, and these methods are generally fallen into two categories: chemical method [8-24], and biosynthesis [25, 26].The chemical method is purely using chemical reagents, and it can be further divided into dry chemical method [8-10] and wet chemical method [11-24]. On the contrary, the biosynthesis is referring the HA crystal formed during the matural metabolism of bacterial [25, 26].

1.1.1.1. Dry chemical method

Many authors prepared HA by using a dry chemical methods [8-10], such as solid-state reaction [8, 9], and mechanical alloying method [10].

Solid-state reaction

Suda and co-workers prepared HA sample by using stoichiometric amounts of $CaHPO_4 \cdot 2H_2O$ and $CaCO_3$ via a solid-state reaction [8]. In order to obtain a pure and stoichiometric HA in the monoclinic form, the complex procedures and multiple heat-treatments were required [8]. *Rhee* also prepared HA by solid-state reaction, but using different chemical reactants, $Ca_2P_2O_7$ and $CaCO_3$ [9]. The above reactants were mixed in acetone and water, respectively [9]. However, they found the single phase of HA was only obtained with powder that was milled in water, and plus the subsequent heat-treatment at 1100 °C for 1h without the additional supplied of water vapour [9].

Mechanical alloying method

Silva and co-workers investigated five different experimental procedures to prepare nanocrystalline HA samples in a pure dry environment, by using mechanical alloying method [10]. By using such method, the heat-treatment was not required, instead, the long milling time up to 60 h was needed [10]. *Rhee* indicated that the dry chemical synthesized HA was advantageous in the mass production due to high reproducibility and low processing costs, and a high degree of crystallinity [9]. In the meantime, he also suggested that the risk of contamination during the milling was involved in the dry chemical methods [9].

1.1.1.2. Wet chemical method

More choices for the preparation of HA were given by using wet chemical methods [11-24], such as hydrothermal [11-15], precipitation [16-20], and sol-gel approach [16, 21-24].

Hydrothermal method

Hydrothermal treatment is one of the earliest synthesized methods that was used to produce HA, by using fluroapatite [$Ca_{10}(PO_4)_6F_2$, FAp] under a pressure of 5000 p.s.i and in the temperature range of 920-1230 °C [11]. Hydrothermal method was also attempted by *Zhang and co-workers*, who managed to prepare HA rods by employing the chemical reagents of dicalcium phosphate anhydrous ($CaHPO_4$, DCPA) and $CaCO_3$ with the temperature range from 120 to 180°C [12]. They found the resulted material exhibited most product was HA with the reaction temperature at 140 °C for 24 hours, however, they noticed a small amount of β-TCP was also presented as a by-product [12]. Figure 1 shows the morphology of HA rods with width of approximately 200 nm and length of several microns [12].
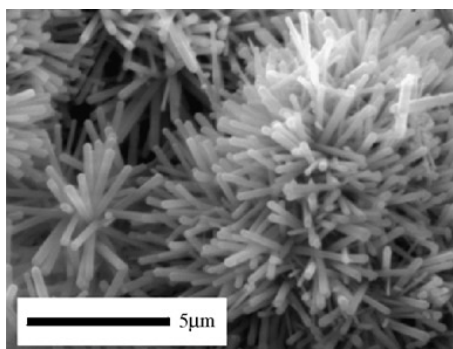
Figure 1: SEM image of HA rods synthesized by a hydrothermal reaction between DCPA and calcite at 140 °C for 24 h [12].

Liu and co-workers investigated the synthesis of HA by using Ca(OH)2 and CaHPO4·2H2O via hydrothermal reaction, which is expressed by Equation 1 [13].

$$4Ca(OH)_2 + 6CaHPO_4 \cdot 2H_2O \rightarrow Ca_{10}(PO_4)_6 + 18H_2O \qquad \textit{(1)}$$
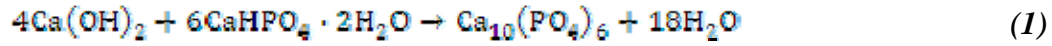
In order to evaluate the influence of pH and temperature on the structure and morphology of HA, the different pH values ranging from 6 to 14, and the different temperatures in the range from 60 to 140 °C , were used, during the synthesis [13]. They indicated that pH exhibited the effect on the morphology, crystallite size and crystallinity of HA, and SEM images of the resulted HA samples synthesized at 140°C with pH at 6, 9, and 14, are presented in Figure 2 (a-c) [13].
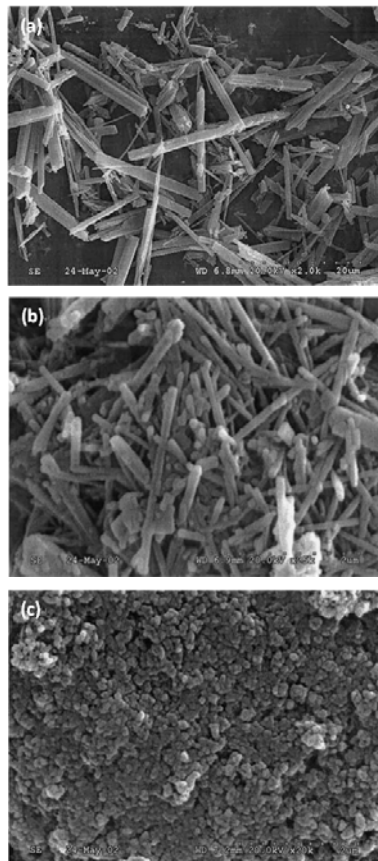
Figure 2: SEM images of HA whiskers and crystals with a different pH value at 140 °C: (a) pH = 6, (b) pH = 9, (c) pH =14 [13].

With pH at 6 and 9, the resulted HA exhibited an almost whisker morphology, whereas the HA synthesized with pH at 14 shown a completely different morphology [13]. HA whiskers had the aspect ratio (i.e. length/diameter) of 3-10, and the median diameter of 2 μm and the length of 20 μm, which was synthesized with pH at 6 [13]. The whiskers became much thinner with aspect ratio > 20, and the typical diameter of 100 nm and length of 2 nm, as the pH increased to 10 [13]. When pH reached to 14, the average particle size of HA at 150 nm was obtained [13]. In addition, they also suggested that the single phase of HA was only obtained at 120°C, when pH of the reaction was kept at 9 [13]. This single phase HA exhibited nano-sized whiskers with the aspect ratio of 8-20, and had the median diameter and length was 40 and 600 nm, as presented in Figure 3 [13].
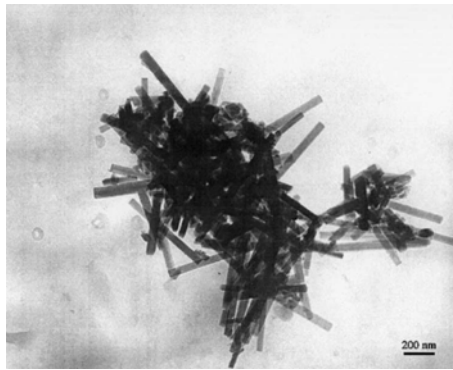
Figure 3: TEM image of HA crystals synthesized at 120 °C for 24h [13].

Hench reported that dense HA ceramics lack the strength when compared with that of the human bones [27]. Due to the low dislocation density, whiskers generally have a good tensile strength [28], therefore, the whisker-like or needle-like HA crystal is considered to exhibit better fracture toughness over HA with other morphologies [13].

The hydrothermal method was again used to study the temperature effect on the HA morphology, by *Kothapalli and co-workers* [14]. During this study, the reactants of calcium nitrate and ammonium hydrogen orthophosphate solutions were applied at temperature range from 25 to 250 °C and time duration from 2 to 10h [14]. *Kothapalli*

and co-workers reported that with increased reaction temperature, the aspect ratio was increased whereas the agglomerate size was decreased [14]. They realized that the temperature at 170°C was critical in their synthesis; as they observed the length of HA crystal was increased when the temperature reached to 170 °C, and it stated to decrease when the temperature was beyond 170 °C [14]. Furthermore, they noticed that with increased aging time and reaction temperature actually exhibited positive effect on the sintered density and the flexural strength of HA [14].

More recently, a new system, named as three pump continuous hydrothermal flow system, was used to prepare HA crystals, reported by *Chaudhry and co-workers* [15]. In order to result phase pure nano-sized HA with high degree of crystallinity, the reagents of calcium nitrate and ammonium phosphate were employed in that new system at 400°C and 24MPa [15]. By using this new system, the aging step or subsequent heat-treatment was not necessarily [15]. Figure 4 shows that resulted HA crystals exhibited rod-like shape in nano domain [15].
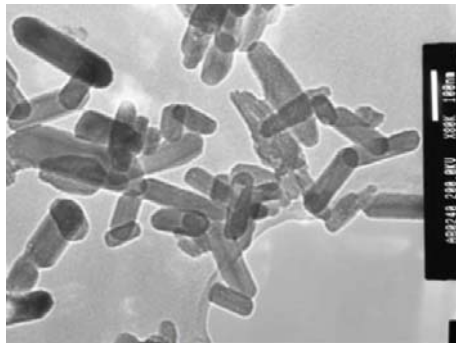
Figure 4: TEM image of nano HA rods prepared by using a three pump continuous hydrothermal flow system at 400°C and 24MPa (bar = 100nm) [15].

Precipitation method

The precipitation method is known as the most commonly used technique for the preparation of HA, due to its simplicity and low processing temperature [16, 17]. The common reactant combinations were orthophosphoric acid with calcium hydroxide [18], diammonium hydrogen phosphate with calcium nitrate [17] and calcium hydroxide with calcium hydrogen phosphate hydrate [19]. Among these combinations, the reaction occurred between orthophosphoric acid and calcium hydroxide was suggested as a valuable method for the industrial production of HA, since the by-product was water [18]. This reaction is expressed in Equation 2 [18].

$$5Ca(OH)_2 + 3H_3PO_4 \rightarrow Ca_{10}(PO_4)_6OH_2 + 9H_2O \qquad (2)$$
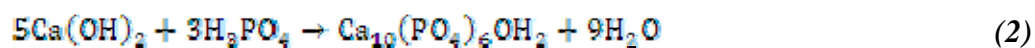
On the other hand, by using precipitation method, the control on the pH value of the reaction was rigid, according to the literature reported by *Jillavenkatesa and co-workers*, who pointed out that the pH was required to be higher than 9, otherwise, the formation of calcium deficient hydroxyapatite (CDHA) was occurred accompanied with a decrease in pH value [16]. In addition, in order to complete the formation of HA, sintering was required. However, decomposition of HA and subsequent formation of tricalcium phosphate (TCP) was resulted by the elevated temperature during the sintering process [16]. Therefore, obtaining HA without subsequent heat-treatment or sintering would be very important. Recently, *Bigi and co-workers* prepared HA crystals by using $Ca(NO_3)_2 \cdot 4H_2O$ and $(NH_4)_2HPO_4$ as the source of calcium and phosphate ions, via a precipitation method [20]. During the synthesis, the pH value of the solution was kept at 10 by using NH_4OH, and the reaction temperature was maintained at 90 °C for 5h [20]. Without a further heat-treatment, the formation of a single phase HA crystals with plate-like shape was evidenced by SEM image, as shown in Figure 5 [20].
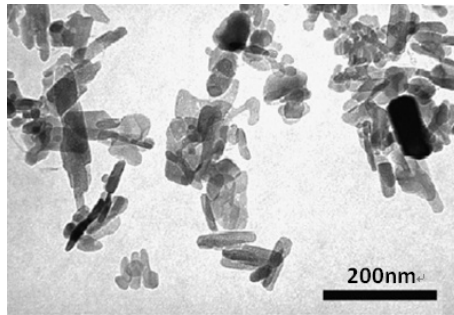
Figure 5: TEM image of HA nanocrystals [20].

Sol-gel approach

Sol-gel approach is also frequently used to prepare HA [16, 21-24], as it offers control over the formation of particular phases and the purity of the formed phase, and allows processing at low temperature [16]. Common reactants include $Ca(NO_3)_2 \cdot 4H_2O$ with $(C_2H_5O)_3PO$ [21], $Ca(OEt)_2$ with $(PO(OEt)_3$ [22], $Ca(NO_3)_2$ with $(HOOCCH_2PO(OH)_2$ [23], and $Ca(NO_3)_2 \cdot 4H_2O$ with P_2O_5 [24]. However, the shortcoming of using this method is that the HA material formed can contain secondary phases, such as CaO, which is reported to exhibit adverse effects on the biocompatibility of HA [21]. As a solution to the above problem, CaO can be converted to $CaCl_2$, which can be subsequently removed by filtration, by treating HA with HCl [21]. Furthermore, other shortcomings of the sol-gel approach were also reported including high cost of alkoxide-based starting materials, complicated steps in order to complete the dissolution of starting materials [24] etc.

Although wet synthesis methods are widely used [11-24], there is a possibility of contamination of HA with impurities leading to the formation of non-stoichiometric HA and resulting in changes of HA structural characteristics and properties [29-32]. Therefore, the control of processing parameters, such as pH, temperature, concentration of reactants during the synthesis are very important as these parameters may induce changes in crystallinity, morphology and particle size which consequently influence the

applications of HA [13, 14, 33-36].

1.1.1.3. Bacterial biosynthesis

It was reported that bacterial species such as *Serratia*. Sp, can release a high local concentration of inorganic phosphate (Pi), stimulated by using glycerol 2-phosphate (G2P) [37, 38]. *Dean* noticed that calcium phosphate was precipitated when the value of calcium and phosphate ions of the product was above its solubility product [39]. Thus *Yong and co-workers* attempted to prepare HA by using *Serratia*. sp [25]. During this biosynthesis, the calcium and phosphate sources were provided by using $CaCl_2$, and inorganic Pi, which was produced enzymatically from *Serratia*. sp by adding G2P [25]. As indicated in Figure 6, the HA material was successfully precipitated on the surface of the bacterial *Serratia*. sp by using such method, and the HA crystallite size was measured as ~25 nm [25]. More recently, *Bagheriasl* studied the effect of different level of phosphatise activity *Serratia*. sp cells on the production of HA [26].
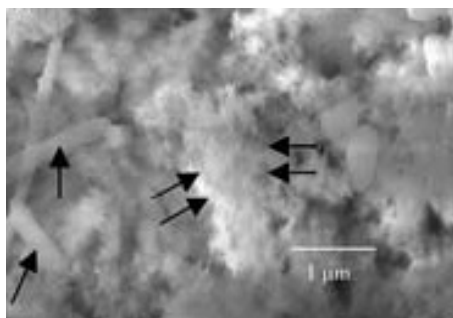
Figure 6: SEM image of the bacterial derived HA, indicated by double arrows [25].

1.1.2. Structural characterization of HA

Posner, Perloff and Diorio reported that the space group and the lattice parameters of synthetic HA was $P6_3/m$, and $a = b = 9.432$ Å, $c = 6.881$ Å, respectively [40]. Figure 7 shows a general view of HA structure in the hexagonal system [17].

Looking at the HA chemical formula, $Ca_{10}(PO_4)_6(OH)_2$, a single unit cell comprise of 44 atoms, including 10 calcium atoms, 6 PO_4 tetrahedra, and 2 OH^- groups that are well organized in a hexagonal system [40-43] and is shown in Figure 7 [17]. It should be noted, that there are some corner-atoms and side-atoms shared with different unit cells [41]. Depending on the crystallographic position of the constituent atoms in the unit cell, 10 Ca atoms are classified into Ca(I) and Ca(II), whereas the O atoms are corresponded to O_I, O_{II}, and O_{III} [44], hence, a more precise chemical formula of HA was suggested as $Ca(I)_4Ca(II)_6(PO_IO_{II}(O_{III})_2)_6(O_{OH}H)_2$ [41].
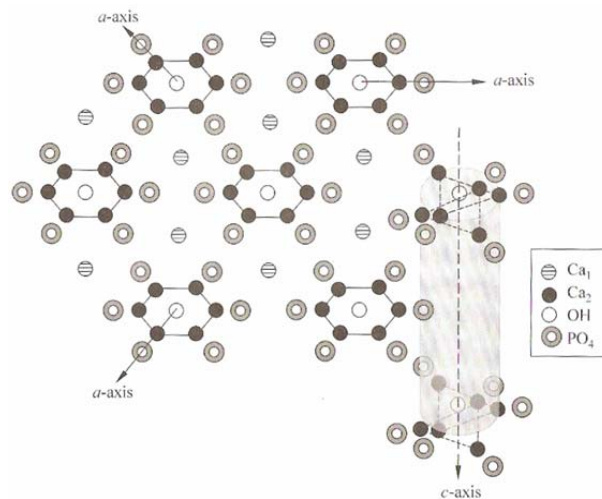
Figure 7: The schematic diagram of hexagonal structure of HA crystal [17].

Hughes and Rakovan reported that the atomic arrangement of apatite was consisted of three cation polyhedra, including PO_4 tetrahedron, $Ca(I)O_9$ polyhedron, and $Ca(II)O_6O_{OH}$ polyhedron [45]. As shown in Figure 8, the central phosphorus atom is

located in the *6h* special position, which is coordinated to 4 oxygen atoms, including $1O_I$, $1O_{II}$, and $2O_{III}$, in the form of a PO_4 tetrahedron [45].
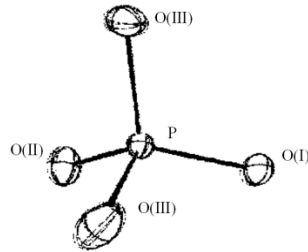
Figure 8: The chemical environment of P atom in one PO_4 tetrahedron [45].

The 4/10th Ca(I) atoms are situated in the *4f* (1/3, 2/3, Z) position, which is coordinated to 9 O atoms in the form of a tri-capped trigonal prism [45], and these 9 coordinated O atoms are from 6 different PO_4 tetrahedra [40, 41], as shown in Figure 9 [44, 46, 47].
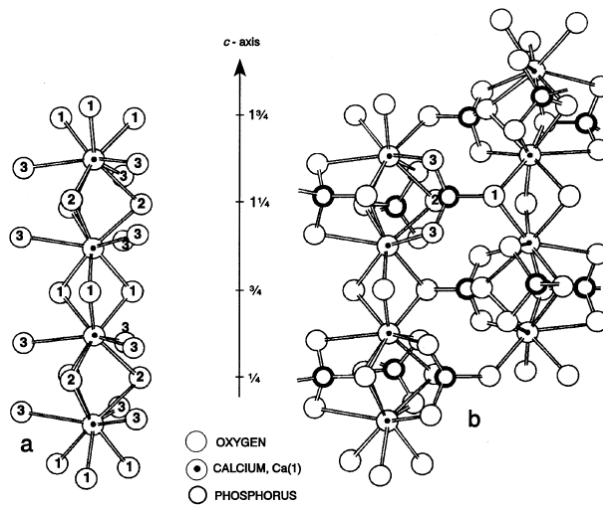
Figure 9: (a) Oxygen coordination of Ca(I) atoms. (b) Ca(I) atoms are coordinated O atoms via P atoms [44, 46, 47].
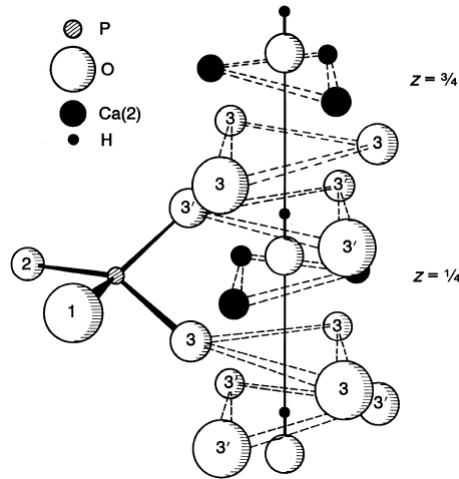
Figure 10: The crystallographic locations of Ca-II atoms and PO$_4$ tetrahedra in the apatite structure [44, 48].

The remaining 6/10th Ca(II) atoms are occupied in the *6h* special position [45], which are coordinated to 7 O atoms of 6 O atoms from 5 PO$_4$ tetrahedra and one from the OH$^-$ group [40, 41]. *Kay and co-workers* suggested that 6 Ca(II) atoms are arranged into two Ca(II) triangles on the mirror planes at z = 1/4 and z = 3/4, and the successive Ca-II triangles were rotated 60° about *c*-axis [17, 49], which is depicted in Figure 7 [17] , and 10 [44, 48]. Similar to Ca(II) atoms, 6 PO$_4$ tetrahedra are also arranged themselves into two PO$_4$ triangles on the mirror planes at z = 1/4 and z = 3/4, and it is hence giving the stability in the HA structure [17, 49].

As illustrated in Figure 7 and Figure 10, the OH$^-$ groups are situated in the *4e* position [50] and occur in the centre of HA column or channel parallel to *c*-axis [49], and this specific position is closely related with the reactivity of HA material, reported by *Arcos and co-workers* [50]. The atomic position of OH$^-$ groups are very interesting in the HA structure, the size of OH$^-$ groups are too large to fit in the space, which is created by the Ca(II) atoms on the mirror planes, and hence the OH$^-$ groups are presented in two-fold statistical disordered about the mirror planes of the Ca-II triangles at z = 1/4 and z = 3/4 with O about 0.3 Å above or below the mirror planes [49]. In addition, the orientation of OH$^-$ groups was suggested to be always away from the mirror planes in the HA

structure [49]. In fact, *Kay and co-workers* proposed two different models, the disordered model and the ordered model, of the OH⁻ groups' arrangements within the column, based on their neutron diffraction data [49]. In the disordered model, the orientation of the OH⁻ groups were suggested to be reversed at different place, whereas the ordered model meant that the orientation of OH⁻ groups was the same, but the choice the orientation was random [49]. The disordered model was preferred in their studies, due to the presence of impurity, F⁻ ions, in their HA sample, therefore, they suggested the possible disordered arrangements of OH⁻ groups in the HA structure can be caused by F impurity present in the reversal point, that was for their case [49]. Alternatively, they indicated that the presence of vacancies at reversal points in the F-free synthetic HA can also lead to the disordered model [49]. Furthermore, they suggested the ordered model should be applied in otherwise [49]. Figure 11 list the possible disordered arrangements of OH⁻ groups in HA [49, 51].
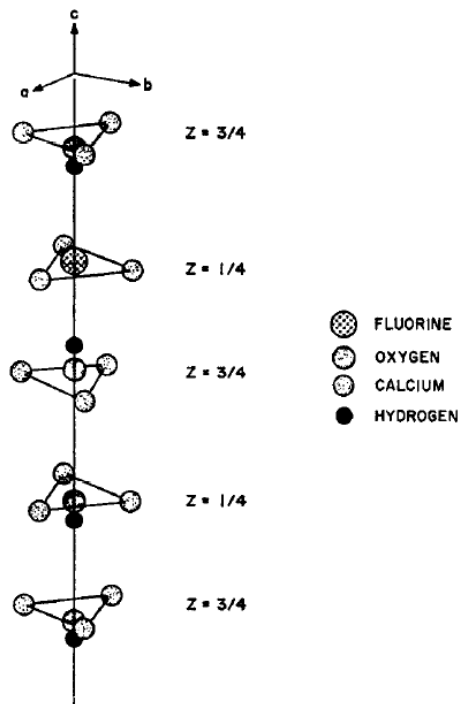
Figure 11: Possible arrangements of OH⁻ groups within the HA column [49, 51].
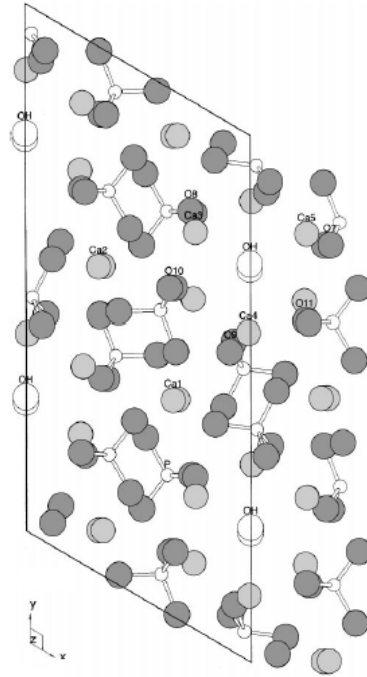
Figure 12: Projection of refined monoclinic HA on (001) plane. Light gray balls indicate calcium; gray balls, oxygen; white balls, hydroxyl oxygen; small white balls, phosphorus [52].

Later, *Elliott and co-workers* confirmed the other possible structure form for the HA than hexagonal structure [53]. The alternative structure was monoclinic structure, which was also reported by *Ikoma and co-workers* [52], who found their HA sample exhibited monoclinic symmetry with the space group of $P2_1/b$, and had the lattice parameters a = 9.426 Å [51], b = 18.856 Å, c = 6.887 Å [53], and γ = 119.97° [54]. Figure 12 shows the projection of monoclinic HA on the (001) plane [52].

In order to clarify the relations between the hexagonal and monoclinic HA, the phase transition between the above two structures were extensively studied [8, 55]. *Suda and co-workers* reported that the monoclinic-hexagonal phase transition was highly dependent on the temperature [8]. The HA exhibited monoclinic structure at room temperature, and the appearance of hexagonal structure was started as the temperature increased to 473 K, and when the temperature reached to 483 K the hexagonal became

predominant phase [8]. Additionally, they also indicated the phase transition process was reversible as it changed back to monoclinic phase once the temperature was cooled down to room temperature [8]. Similar observation was also reported by *Van Rees and co-workers* [55]. Despite the influence brought by temperature, the presence of sufficient of impurities, such as F^-, or/ and vacancies also led HA structure changed from monoclinic to hexagonal [45, 49].

Ikoma and co-workers pointed out that the greatest structural difference between monoclinic and hexagonal HA was due to the arrangements of the OH^- groups [52], which was previously proposed by *Kay and co-workers* [49]. In the monoclinic HA structure, OH^- groups appearing in the form of O-H, O-H, O-H in one column and H-O, H-O, H-O in another column [53], reflecting the ordered structure [52]. In the hexagonal HA system, the OH^- groups exhibiting in the order of H-O, O-H, H-O, O-H along the *c*-axis, stabilizing the two-fold disordered arrangement [49], due to the presence of the mirror planes at $z = 1/4$ and $z = 3/4$, and the occupancy factor of the O of the OH^- groups was 1/2 [17, 49, 52]. Finally, they summarized the ordered or disordered atomic arrangement of OH^- groups were essential to stabilize the monoclinic or hexagonal structure of HA and it subsequently influenced the physical and chemical properties of HA [52].

1.1.3. Applications of HA

HA is similar to the main constituent of mineral phase of bone and teeth, therefore it showing excellent biocompatibility, good bioactivity, and osteoconductivity properties [2], and hence creating wide range of applications in many fields, in particularly in the biomedical field [56-58].

Heise and co-workers reported HA ceramics with interconnected porous system was used as bone substitutes for grafting in bone replacement [56]. No incompatibility or rejection of this implanted material was observed [56]. *Kuo and co-workers* suggested HA can be applied on the metallic substrate as coating [3]. In this case, the resulted material can maintain the biocompatibility, but also exhibit better mechanical properties [3]. *Khairoun and co-workers* prepared bio-cements by mixing precipitated HA, α-tertiary, and monetite [57]. They proposed such cement can be applied in orthopaedics, plastic, and reconstructive surgery [57]. In addition, other possible clinical applications were also given, such as maxillofacial surgery [57]. *Zhu and co-workers* prepared nanocrystalline HA particles by a precipitation hydrothermal technique [58]. Such HA particles exhibited biocompatibility in *vitro* and no acute toxic adverse effect was noticed in *in vivo* animal studies for two weeks time [58]. Hence, they suggested that these HA particles consist a promising biomaterial to be employed as gene carrier and vectors [58].

Except of the wide applications in the biomedical field [56-58], environmental applications were also exploited [59-62], like water purification, waste stabilization, contaminated soil remediation, and heavy metal adsorption [25, 59-62].

1.2. Bioapatites

1.2.1. HA in the body

It is known that the synthetic HA is a type of calcium phosphate that exhibit similarities to the mineralized tissues of mammal, such as bone and tooth [1, 63].

1.2.1.1.   Bone

Bone is a composite material, which is consisted of about 69 wt% calcium phosphate, 20 wt% type-I collagen fibrils, 10 wt% water, and the remains are other organic substances [17, 64-66]. Figure 13 [67] depicts the highly complex structure of bone with up to seven hierarchical levels of organization [66].

From the macroscopic point of view, bone can be described into two terms: cortical bone and cancellous bone [65, 68]. As indicated in Figure 13 (A) [67], the cortical bone usually present at the outer layer of the bone, whereas the cancellous bone is located in the core of the bone, and is surrounded by the cortical bone [65, 67, 68].

From the microscopic point of view, bone is built up by the basic building blocks, osteons, as presented in Figure 13 (B, C) [67]. As shown in Figure 13 (C), the canal is situated at the central of the osteon, which is surrounded by lamellae that are formed by bundling fibers, which are built up by many collagen fibrils in a certain array [69], as indicated in Figure 13 (D, E) [67]. As depicted in Figure 13 (G, H) [67], small platelet-like apatite crystals with the average dimensions of $\sim$30 $\times$ 50 $\times$ 2 nm, are fitted into the holes, which are created by the collagens with the *c*-axis parallel to the micorfibral long axis [66, 67, 69-72].
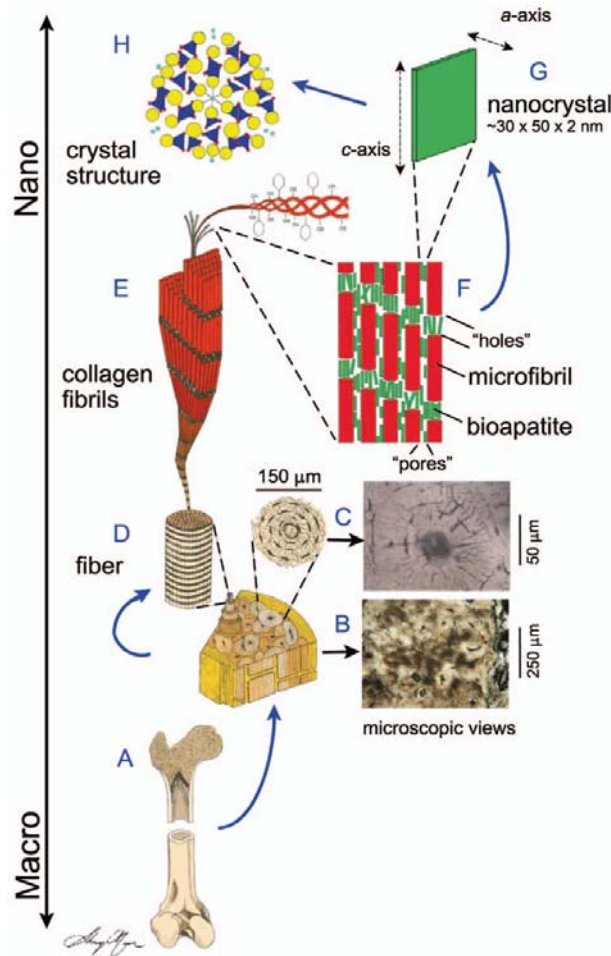
Figure 13: The schematic diagram of the hierarchical structure of the bone [67].

1.2.1.2. Tooth

As presented in Figure 14 (a), tooth can be described into two terms: enamel, the external surface, dentine, an internal region of tooth [65].

Enamel is the hardest tissue in the body and hardly contains collagen [1, 65, 73]. It contains 97 wt% of apatite crystals with the thickness of 25 nm, with the width of 40-120 nm and with the length of 160-1000 nm [1, 73]. The apatite crystal in enamel forms into well-defined needle-like rod and has the diameter of approximately 5μm [1,

73, 74]. As indicated in Figure 14 (b) [74], the enamel crystals are well arranged in a parallel fashion under the biological control [68]. Additionally, a small fraction of fluoride content about 0.01 wt% is presented on the surface of the enamel [75].

Dentine is more alike to the bone, and it contains 45 vol% mineral phase and the rests are formed by 30 vol% collagen and 25 vol% water [65]. As presented in Figure 14 (c), the main feature of dentine is the tubules, which have the diameter of approximately 1μm [76]. They are surrounded by apatite crystals with the diameter approximately of 0.5-1μm, and organized in a random array [65].
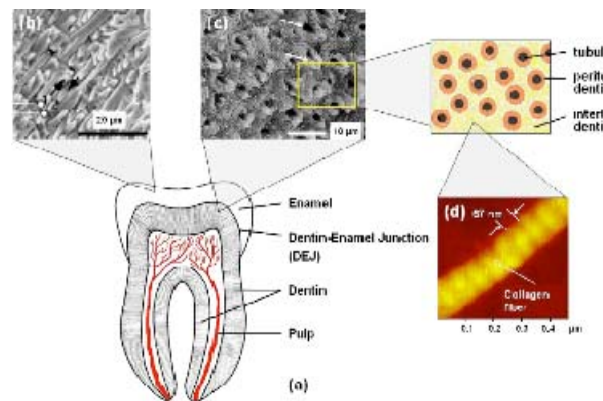
Figure 14: The hierarchical structure of a tooth. (a) The schematic sketch of a tooth [65]. (b) SEM image of a mature enamel of the mouse [74]. (c) SEM image of a dentine [76]. (d) AFM image of a collagen fiber [77].

1.2.2. Characterization of bioapatites

The certain degree of the similarities is admitted between the bioapatite, bone, teeth, and the synthetic HA [1], however, they are not necessarily to exhibit an identical crystallographic structure, chemical composition, crystallinity, crystallite size, and etc [78].

Harper and co-workers studied that the well-crystalline synthetic HA, synthetic HA

with the small crystallite size and human bone femur apatite by using XRD technique, the XRD patterns of the above specimens are shown in Figure 15 [79].
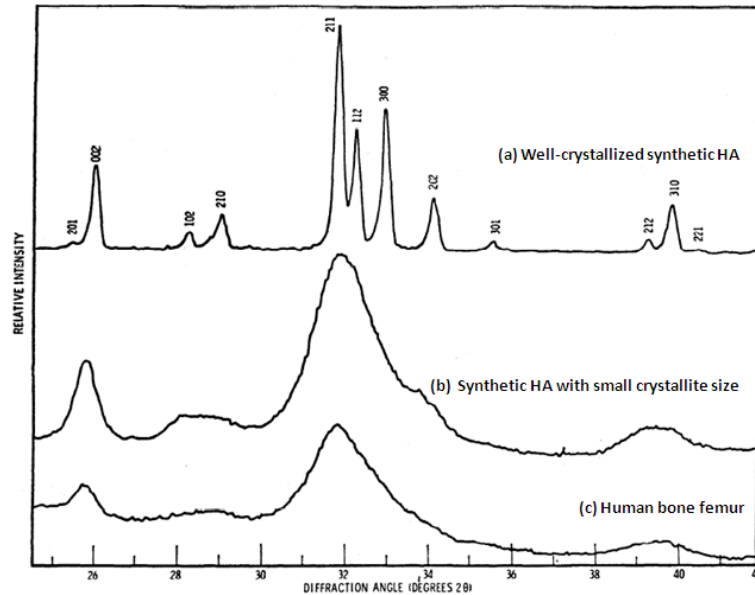
Figure 15: XRD patterns of (a) well-crystallized synthetic HA, (b) synthetic HA with small crystallite size, (c) human bone femur (The two lower samples were reproduced with the same scale whereas the higher samples were used a convenient arbitrary scale) [79].

As observed in Figure 15, *Harper and co-workers* found that the (c) human bone femur apatite exhibited similar XRD pattern to that of in (b) the synthetic HA with small crystallite size [79]. Similar XRD peak width suggested that the (c) human bone femur apatite was consisted of small crystallite size [79]. In addition, *Harper and co-workers* observed that the intensity of the XRD pattern in the (b) human bone femur apatite was lower than that of in other two HA samples (a, b), the well-crystalline HA and the synthetic HA with small crystallite size [79]. The reduced intensity in the case of (b) indicated that the human bone femur apatite was not fully crystallized and contained approximately 40 % amorphous phase [79].

Termine and co-workers suggested that amorphous phase in the bone was varied with

the age [80], as they noticed the fraction of amorphous mineral in rat femur was decreased from 69 to 36% with increased animal age from 5 to 70-days-old [80].

Unlike to synthetic stoichiometric crystalline HA, the biological apatites, bone, tooth, are usually non-stoichiometric associate with poorer degree of crystallinity, due to the incorporation of various substitutions in the apatite structure [81, 82]. One of the major substitutions in the biological apatites is CO_3^{2-}, ranging from approximately 3 to 8 %, others, such as Mg^{2+}, Na^+, K^+, F^-, Cl^-, and etc, are presented as trace elements, as listed in Table 1 [68, 83, 84].

Table 1: Chemicals and crystallographic characteristics of bioapatites and synthetic hydroxyapatite [68, 83, 84].

Composition	Enamel	Dentin	Bone	Hydroxyapatite (HA)
calcium [wt %][b]	36.5	35.1	34.8	39.6
phosphorus (as P) [wt %][b]	17.7	16.9	15.2	18.5
Ca/P (molar ratio)[b]	1.63	1.61	1.71	1.67
sodium [wt %][b]	0.5	0.6	0.9	–
magnesium [wt %][b]	0.44	1.23	0.72	–
potassium [wt %][b]	0.08	0.05	0.03	–
carbonate (as CO_3^{2-}) [wt %][c]	3.5	5.6	7.4	–
fluoride [wt %][b]	0.01	0.06	0.03	–
chloride [wt %][b]	0.30	0.01	0.13	–
pyrophosphate,(as $P_2O_7^{4-}$) [wt %][c]	0.022	0.10	0.07	–
total inorganic [wt %][c]	97	70	65	100
total organic [wt %][c]	1.5	20	25	–
water [wt %][c]	1.5	10	10	–
a axis [Å][d]	9.441	9.421	9.41	9.430
c axis [Å][d]	6.880	6.887	6.89	6.891
crystallinity index, (HA = 100)	70−75	33−37	33−37	100
typical crystal sizes [nm][1, 105, 107]	100 × 50 × 50μm	35 × 25 × 4	50 × 25 × 4	200−600
ignition products (800°C)	β-TCP + HA	β-TCP + HA	HA + CaO	HA
elasticity modulus (GPa)[26]	80	15	0.34−13.8	10
compressive strength (MPa)	10	100	150	100

[a] Because of the considerable variation found in biological samples, typical values are given in these cases. [b] Ashed samples. [c] Unashed samples [d] Lattice parameters: ±0.003 Å.

Similar to the degree of crystallinity [80], the substitution concentration in biological apatite is also changed with age [2]. For instance, the CO_3^{2-} content was reported to increased with age whereas the HPO_4^{2-} content was decreased [2].

As indicated in Table 1, the chemical environment and crystallographic structure of bioapatites are far more complicated than that of in synthetic HA or carbonate substituted HA, due to the imperfection of apatite crystals, originated from the multiple

foreign substitutions [85]. Hence, the chemical formula of bioapatites can be written as $(Ca, M)_{10}(PO_4, Y)_6(OH, X)_2$, where M represent cations, include Mg^{2+}, Na^+, K^+, Sr^{2+}, and Ba^{2+}, etc, Y represent carbonate, acid phosphate, HPO_4^{2-}, sulfates, etc, and X represent F-, Cl-, carbonate, etc , proposed by *Shi* [17].

1.3. Synthetic substituted HA

The HA structure allows the incorporation of wide range of different ionic substitutions, and it leads to different degree of alterations in the original HA structure, depending on the type of substitution and the substitution quantity [20, 86-103] . Subsequently, it results in the changes of the HA characteristics, such as the degree of crystallinity, morphology, lattice parameters, the stability of HA structure, and ultimately it exhibit different mechanical properties, as well as influence the biological response in the final applications [83, 89, 104-114].

As a consequence, synthesis of substituted HA has attracted a lot of interest [20, 86-103], as substituted HA can exhibit desirable properties and satisfy variety of needs in a wide range of applications [83, 89, 104-114].

.

1.3.1. Synthesis and morphology of synthetic substituted HA

1.3.1.1.   Zinc substituted HA (Zn-HA)

Tripathy and co-workers reported that Zn hydroxyapatite solid solution with chemical formula of $Zn_{10}(PO_4)_6(OH)_2$ was prepared by using co-precipitation method in an aqueous media [86]. However, many other researchers found that Zn actually exhibited inhibiting effect on the crystallization of HA, and hence suggested the synthesis of Zn-HA over the entire compositional range was impossible [87-89].

Bigi and co-workers attempted to synthesize a group of apatite samples with the Zn concentration in the solution, ranging from 0 to 100 atom%; however, the unique crystalline phase was obtained with the Zn concentration only up to approximately 25 atom% [87]. With increased Zn concentration the XRD exhibited amorphous structure, or other crystalline products, such as zinc and calcium phosphate, when Zn concentration reached to even higher levels [87].

Li and co-workers reported Zn-HA samples with Zn concentration of approximately 20 mol% were successfully synthesized by using the reagents of $Ca(NO_3)_2$, $(NH_4)_3HPO_4$, and $Zn(NO_3)_2$ via hydrothermal method [89]. As shown in Figure 16, the crystallite size and crystallinity of Zn-HA samples were decreased with increased Zn concentration from 0 to 15 mol%, while the numbers of the Zn-HA crystals were increased [89].
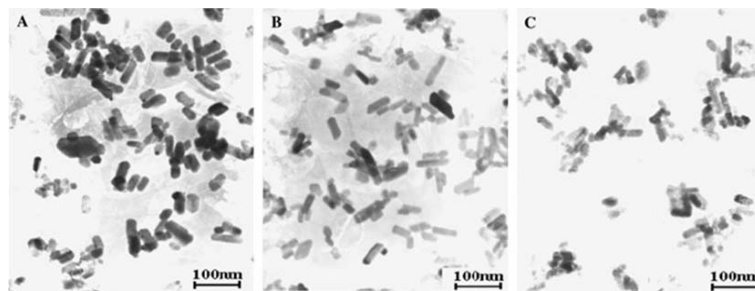
Figure 16: TEM image of Zn-HA crystals with different Zn concentration: (a) 0 mol%, (b) 5 mol%, (c) 10 mol% [89].

In order to avoid the incorporation of NO_3 or Cl^- into the apatite structure, originated from using of the reagents of calcium nitrate or calcium chloride [88]. *Miyaji and co-workers* employed $Ca(CH_3COO)_2 \cdot H_2O$, $Zn(CH_3COO)_2 \cdot 2H_2O$, and $(NH_4)_2HPO_4$ as chemical reactants to prepare Zn-HA samples via precipitation method, since the acetate ions were not incorporated into apatite structure [88, 115]. The reaction among the above reactants is described in Equation 3 [88].

$$10x\text{Ca}^{2+} + 10(1-x)\text{Zn}^{2+} + 6\text{PO}_4^{3-} + 2\text{OH}^- \rightarrow$$
$$\text{Ca}_{10}\text{Zn}_{10(1-x)}(\text{PO}_4)_6(\text{OH})_2 \quad (0.1 \leq x \leq 1.0)$$

(3)
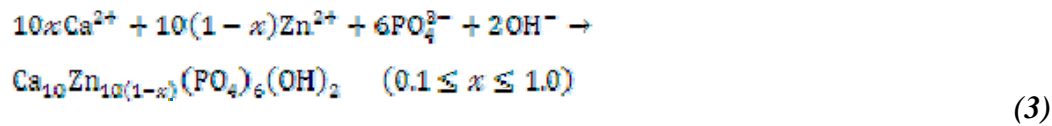
By using the precipitation method described as above, *Miyaji and co-workers* estimated that the limits of Zn substituted Ca in the apatite structure was approximately 15 mol% [88], which exhibited slightly lower substituting value compared with the one reported by *Li and co-workers*, who suggested that the small difference on the substituting limit value was attributed to the consequence of using different synthesized methods [89]. *Li and co-workers* indicated that the Zn-HA samples were more difficult to prepare by using precipitation method rather than using hydrothermal method [89].

Within the substituting limits, *Miyaji and co-workers* found that the crystallite size and crystallinity was decreased with the increased Zn substitution [88], which agreed with the work that presented by *Li and co-workers* [89]. Furthermore, *Miyaji and co-workers* suggested that the order of the produced phases with increased Zn substitution was Zn substituted apatite, amorphous phase, and amorphous phase + parascholzite ($\text{CaZn}_2(\text{PO}_4)_2 \cdot 2\text{H}_2\text{O}$) [88].

1.3.1.2.   Magnesium substituted HA (Mg-HA)

Chiranjeevirao and co-workers reported that Mg-HA solid solutions in the whole range of composition were prepared by using calcium nitrate, magnesium nitrate, and ammonium dihydroygen phosphate in an aqueous media [90]. The exchange process of calcium and magnesium in apatite was described by Equation 4 [90, 91].

$$\text{Ca}_{10}(\text{PO}_4)_6(\text{OH})_2 + n\text{Mg}^{2+} \rightarrow \text{Ca}_{10-n}\text{Mg}_n(\text{PO}_4)_6(\text{OH})_2 + n\text{Ca}^{2+}$$

(4)
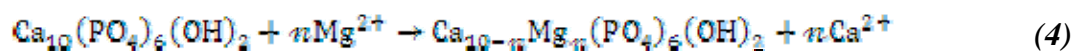
During the synthesis, the pH of the solution was maintained above 9, in order to avoid the formation of calcium deficient apatite [116]. Similar work was carried out by *Patel*,

who prepared similar Mg-HA solid solutions by using same reactants, but synthesized with the higher pH value, which was above 11 [91].

On the other hand, such results were not able to reproduce by many other researchers [92-94]. In fact, *Bigi and co-workers* pointed out that the Mg exhibited similar effect as Zn, which inhibited the crystallization of HA [87, 92].

Bigi and co-workers prepared HA samples with various Mg concentrations by using the reactants of calcium nitrate, magnesium nitrate, and ammonium dihydroygen phosphate [92]. *Bigi and co-workers* found that the unique crystalline apatitic phase was only achieved with Mg concentration in the range of 0 to 30 atom % [92]. With increased Mg concentration from 35 to 50 atom %, the completely amorphous structure was observed, and the formation of other crystalline phases, such as $Mg_3(PO_4)_2 \cdot 8H_2O$, and $NH_4MgPO_4 \cdot H_2O$, were presented, when the Mg concentration was even higher [92]. Additionally, *Bigi and co-workers* found that within the substituting limits of Mg, the crystallite size, crystallinity, and the Ca/P ratio was decreased with increased Mg concentration [92].

Different effect of Mg on the crystallite size and crystallinity of apatite was reported by *Yasukawa and co-workers*, who prepared Mg-HA solid solutions with Mg (Mg + Ca) molar ratio ranging from 0 to 0.5 by wet method, using the reagents of $Mg(NO_3)_2 \cdot 6H_2O$, $Ca(OH)_2$, and H_3PO_4 [93]. As presented in Figure 17 (a-e), the crystallite size of apatite was increased and more porous was presented with increased X_{Mg} from 0 to 0. 31 [93]. When X_{Mg} reached to 0.38, amorphous morphology was observed in Figure 17 (f) [93].
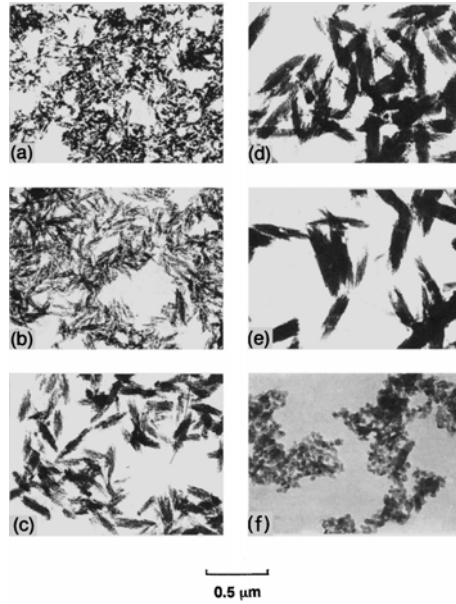
Figure 17: TEM image of Mg-HA samples with different XMg: (a) 0, (b) 0.09 mol%, (c) 0.16, (d) 0. 23, (e) 0.31, (f) 0.38 [93].

Fadeev and co-workers prepared Mg substituted HA samples with chemical formula of $Ca_{10-x}Mg_x(PO_4)_6(OH)_2$, where X< 1, by using $Ca(NO_3)_2$, $Mg(NO_3)_2$, and $(NH_4)_2HPO_4$ via wet method, as described in Equation 5 [94].

$$(10 - x)Ca(NO_3)_2 + xMg(NO_3)_2 + 6(NH_4)_2HPO_4 + 8NH_4OH \rightarrow$$
$$Ca_{10-x}Mg_x(PO_4)_6(OH)_2 + 20NH_4NO_3 + 6H_2O; \quad 0.1 \leq x \leq 1.0 \qquad (5)$$
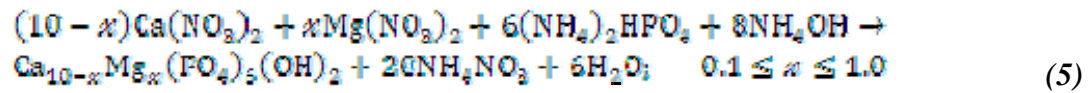
where NH_4OH was used to adjusted pH of the solution [94]. *Fadeev and co-workers* found that Mg exhibited destabilizing effect on the apatite structure, since the transition temperature from hydroxyapatite to whitlockite was decreased with increased Mg substitution from 1 to 10 atom % [94].

1.3.1.3.   Strontium substituted HA (Sr-HA)

It is generally agreed that the Sr-HA samples can be prepared in the whole range of composition [20, 95], according to the equation 6 [117].

$$Ca_{10}(PO_4)_6(OH)_4 + nSr^{2+} \rightarrow Sr_nCa_{(10-n)}(PO_4)_6(OH)_2 + nCa^{2+}$$ *(6)*
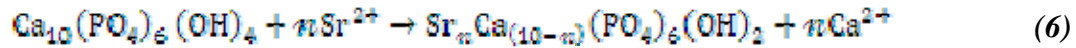
O'Donnell and co-workers prepared Sr-HA samples with Sr substitution ranging from 0 to 100% by using two different routes [95]. They found that the crystallite size of the Sr-HA samples was approached to the minimum value when the Sr substitution reached to 50 % [95]. Additionally, *O'Donnell and co-workers* pointed out that the presence of small amount of impurities, strontium pyrophosphate, was observed in the fully Sr substituted apatite sample [95].

Similar changes of the crystallite size varied with Sr substitution were reported by *Bigi and co-workers*, who synthesized a group of Sr-HA samples by using $Ca(NO_3)_2 \cdot 4H_2O$, $Sr(NO_3)_2$, and $(NH_4)_2HPO_4$ via precipitation method [20]. With increased Sr substitution from 0 to 100 %, a systematic changes of the crystallite size and crystallinity of the Sr-HA samples were evidence by the TEM micrographs, as presented in Figure 18 [20].
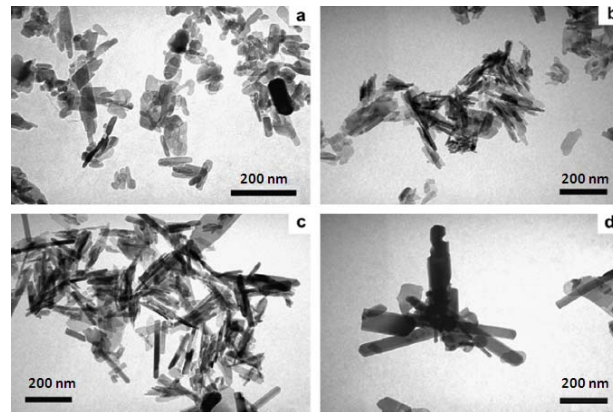
Figure 18: TEM image of Sr-HA samples with different Sr concentration: (a) HA, (b) HA with 20 % Sr, (c) HA with 70 % Sr, (d) HA with 100 % Sr [20].

As indicated by Figure 18, *Bigi and co-workers* found that the HA sample contained 0% Sr substitution exhibited plate-like crystals with mean dimension of up to approximately 200 × 40 nm [20]. By increasing Sr substitution to 20 %, the ill-defined

apatite crystals with perturb shapes were observed in Figure 14 (b) [20]. With increased Sr substitution to 70 % or higher, the apatite crystallite size was increased [20]. When the Sr substitution reached to 100 %, the fully Sr substituted apatite had crystallite size of approximately 500×100 nm with the morphology of the well-defined crystal shape, which elongated in the crystallographic *c*-axis direction [20].

1.3.1.4.   Silicon substituted HA (Si-HA)

Numerous methods were proposed to prepare Si-HA samples [96, 97, 118, 119]. However, it was seems that the synthesis of pure Si-HA samples was not easy [118, 119].

Ruys prepared Si-HA samples by using sol-gel approach, however, the resulted materials were not only containing apatite phase, it were also exhibiting other phases, such as calcium silicophosphate, and tricalcium phosphate, depending on the composition [118].

Boyer and co-workers proposed that the synthesis of Si-HA by using solid-state reaction [119]. In order to obtain the Si-HA product, the incorporation of other ions, such as La^+ or SO_4^{2-}, were needed [119]. Thus, the resulted material was not Si-HA [119].

In order to prepared phase pure Si-HA, *Gibson and co-workers* proposed that to produce the as-prepared Si-HA sample with 0.4 wt% Si substitution by using $Ca(OH)_2$, $Si(CH_3COO)_4$, H_3PO_4 via an aqueous precipitation reaction, as described in the Equation 7 [96]. With an appropriate calcining process at temperature above 700°C, the single phase of Si-HA was obtained without the formation of any other secondary phases, such as TCP, CaO, and etc [96].

$$Ca_{10}(PO_4)_6(OH)_2 + xSiO_4^{4-} \rightarrow Ca_{10}(PO_4)_{6-x}(SiO_4)_x(OH)_{2-x} + xPO_4^{3-} + xOH^- \quad (7)$$
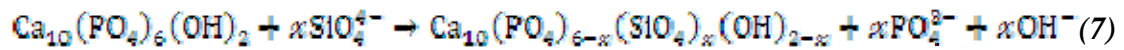
The phase pure of silica-hybridized HA with Si hybridization of SiO_2 ranging from 0 to 33 wt% was investigated by *Fujii and co-workers*, who prepared such samples from the reagents of $Ca(OH)_2$, H_3PO_4, and $[CH_3(CH_2)_3O]_4Si$ [98]. *Fujii and co-workers* pointed out that the incorporation of Si hybridization exhibited little effect on the crystallite size and morphology of silica-hybridized HA samples [98]. As presented in Figure 19, all silica-hybridized HA samples displayed needle-like apatite crystals with the dimensions of approximately 150×20 nm [98].
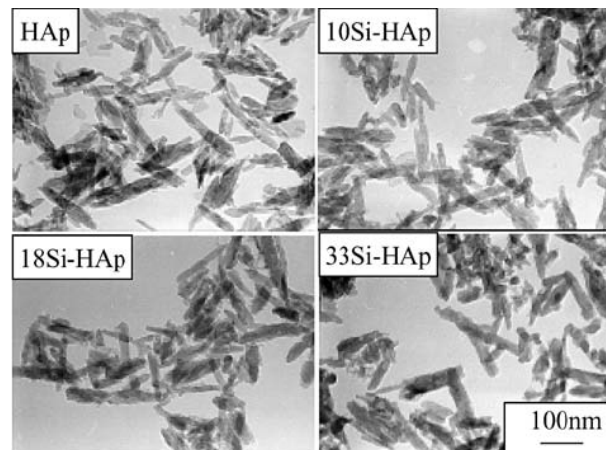
Figure 19: TEM micrographs of silica-hybridized HA samples with Si hybridization ranging from 0 to 33 wt% [98].

Tang and co-workers reported that Si-HA samples with Si substitution ranging from 0 to 4 wt% were prepared by using $Ca(NO_3)_2 \cdot 4H_2O$, $(NH_4)_3PO_4$, and $Si(OCH_2CH_3)_4$ (TEOS) via hydrothermal method [97]. As observed in Figure 20, *Tang and co-workers* noticed that the mean crystallite size of apatite was decreased with the content of TEOS, while the numbers of the need-like apatite crystals were increased [97].
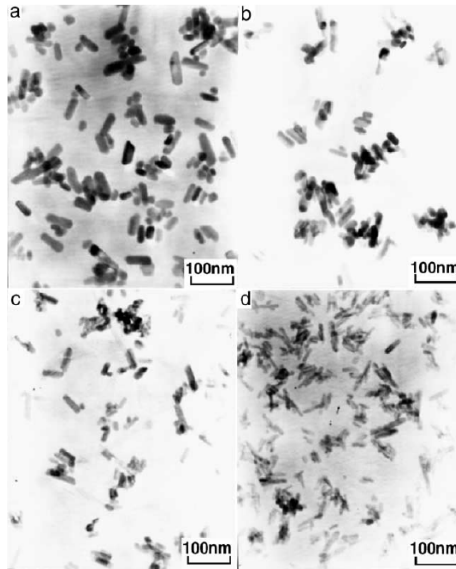
Figure 20: TEM micrographs of four Si-HA samples with different Si concentration: (a) HA, (b) HA with 0.8 wt% Si, (c) HA with 1.5 wt% Si, (d) HA with 4 wt% Si [97].

1.3.1.5. Carbonate substituted HA (CO_3-HA)

Within the HA lattice structure, the CO_3^{2-} ions either exchanged with OH^- groups in the channel site, assigned to A-type CO_3^{2-} substitution, or replaced PO_4^{3-} tetrahedra, corresponded to B-type CO_3^{2-} substitution [83, 120].

Stéphane and co-workers prepared A-type CO_3^{2-} apatite by exposing pure HA sample in the CO_2 environment at 900 °C for 3 days [99]. In order to prevent the rehydration of the apatite surface as well as to obtain the highest carbonation rate, the water vapour pressure was maintained at the lowest level [99]. The formation of A- type CO_3^{2-} apatite is represented in Equation 8 [99].

$$Ca_{10}(PO_4)_6(OH)_2 + x\,CO_2 \rightarrow Ca_{10}(PO_4)_6(OH)_{2-x}(CO_3)_x + x\,H_2O \qquad (8)$$
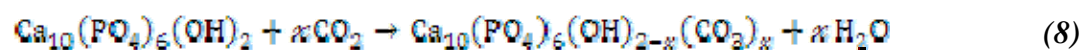
It was however indicated by Gibson, who pointed out that such method was disadvantageous in the biomedical application, since the preparation time was long, the quantities of CO_3^{2-} content were not able to be controlled easily [114]. Furthermore,

due to the uses of the ion exchange process presented in Equation 8, the carbonation on the surface was more readily to happen rather than in the bulk of the apatite materials [114].

Gibson and co-workers indicated that the synthesis of B-type CO_3^{2-} apatite was more complicated compared to the synthesis of A-type CO_3^{2-} apatite, due to the charge imbalance issue arisen by CO_3^{2-} content substituted PO_4^{3-} in the apatite lattice [114]. In order to compensate the charge difference caused by the B-type CO_3^{2-} substitution, the reagent of sodium carbonate was introduced as the source of CO_3^{2-}, and used Na to co-substitute Ca [101, 102], which is described in Equation 9 [114].

$$Na^+ + CO_3^{2-} \leftrightarrow Ca^{2+} + PO_4^{3-} \tag{9}$$

Sampath and co-workers attempted to prepare B-type CO_3-HA samples with CO_3^{2-} concentration ranging from 10 to 40 mol% by using the microwave irradiation method, among the reactants of $Ca(OH)_2$, $(NH_4)_2HPO_4$, and $CaCO_3$ [100]. They revealed that the substituting limit of CO_3^{2-} for PO_4^{3-} was approximately 20 mol% in their CO_3-HA samples, as the decomposition of apatite into HA and TCP was observed when the CO_3^{2-} beyond the substituting limit [100].

The bioapatite was recognized as AB-type CO_3^{2-} apatite [121, 122], but B-type CO_3^{2-} substitution was always considered as the prominent one [83]. Hence, Barinov and co-workers prepared biomimic apatite, containing both A-type and B-type CO_3^{2-} substitution, by using the reagents of calcium oxide, ammonium hydrogen phosphate and ammonium carbonate via the reaction, which is shown in Equation 10 [123].

$$10CaO + 6(NH_4)_2HPO_4 + (NH_4)_2CO_3 + 4H_2O \rightarrow Ca_{10}(PO_4)_{6-y}(CO_3)_x(OH)_{2-x} + 14NH_4OH; \quad 3y + x = 2 \tag{10}$$
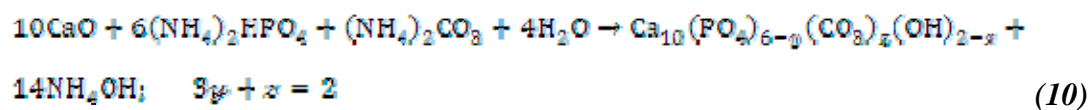
The synthesis of AB-type CO_3^{2-} apatite samples were also investigated by *Barralet and co-workers*, who prepared such samples with different reagents, tri-ammonium orthophosphate, calcium nitrate 4-hydrate, and sodium bicarbonate by using precipitation method [103]. As shown in Figure 21, *Barralet and co-workers* observed that with increased bicarbonate concentration from 10 to 160 mM, the apatite crystallite size was slightly decreased, and the morphology of the apatite was formed as needle-like shape and changed into more spheroidal [103]. Similar changes on the morphology of the carbonate apatite samples were also reported by *Legeros* [124].
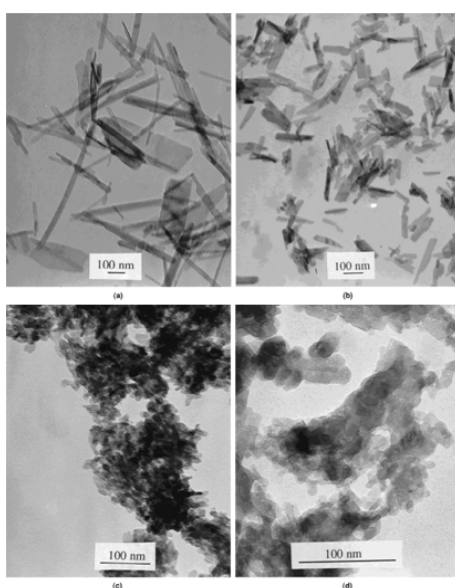
Figure 21: TEM micrographs of AB-type CO_3^{2-} apatite with different bicarbonate concentration precipitated at 70 °C: (a) 10 mM, (b) 40 mM, (c) 160 mM, and (d) 320 mM [103].

1.3.2. Structural characterization of synthetic substituted HA

1.3.2.1.　Zn-HA

Several reports indicated that the substituting of Zn^{2+} for Ca^{2+} in the HA structure was extremely difficultly, since Zn exhibited the inhibiting effect on the HA crystallization [87-89, 125] and promoting the formation of β-TCP or other Zn substituted phosphates [87-89], and that were very likely attributed to the substituent of Zn^{2+} with smaller cationic radius of (0.74 Å) in the HA structure exchanged with larger cation of Ca^{2+} (0.99 Å) [87, 89, 125].

Although Zn acted as an inhibiting role in the HA crystallization, the synthesis of apatite samples with low concentration of Zn were possibly achieved [87-89, 126]. Compared with the amount of Zn substitution in the HA structure for Ca, the greater amount of Zn content was assumed to be adsorbed on the apatite surface and/ or in the amorphous phase, suggested by *Bigi and co-workers*, as the Ca/P ratio in the solid phase was almost same as that in solution [87].

As described in *1.1.2*, two distinction sites of Ca atoms were occupied in the HA structure, denoted respectively as Ca-I and Ca-II [44]. *Matsunaga* demonstrated the first-principle studies in the substitution of Zn and Mg in the structure of HA and OCP, and he reported that both Zn^{2+} and Mg^{2+} were energetically favoured in the Ca-II site rather than Ca-I site in the HA structure ,based on simple geometry consideration and the relation between the cationic radius and coordination number [127]. *Tang and co-workers* confirmed the above mentioned and suggested that Zn preferred to replace Ca-II site than Ca-I site, by using density function theory (DFT) calculations [128].

Considering that the cationic radius of Zn is smaller than the radius of Ca [87, 89, 125], it is expected that changes should occur within the HA lattice parameters [88, 89]. *Li*

and co-workers found that with increasing Zn substitution to 10 mol%, the lattice parameter *a* was decreased but started to increase when Zn substitution was over 10 mol%, while parameter *c* was monotonously decreased [89]. *Miyaji and co-workers* also reported that the lattice parameter *a* was decreased with increasing Zn substitution up to 5 mol% but increased when Zn substitution was higher than 5 mol%, while the lattice parameter *c* was decreased monotonously with increasing Zn substitution [88]. However, *Miyaji and co-workers* reported later, that the increased lattice parameter *a* in the apatite samples with higher Zn substitution was attributed to the incorporation of increased lattice H_2O that substituted OH in the HA structure, as the lattice parameters of *a* and *c* were both decreased with increasing Zn substitution after heat-treatment at 400°C [88].

1.3.2.2.   Mg-HA

Very similar to Zn [87, 92], Mg inhibited the crystallization and crystal growth of HA, and destabilized HA structure into β-TCP [92] or other Mg substituted phosphate [94], which were possibly related to the smaller Mg cation with radius (0.65 Å) substituted larger cation of Ca (0.99 Å) in the HA structure [94].

Due to the inhibiting role of Mg on the HA crystallization [92], approximately 10 atom % of Mg was a maximum amount that entered into the HA structure for Ca, reported by *Bigi and co-workers* [129]. In addition, they also suggested the preferential site of Mg in HA structure was at Ca-II (6*h*) site [129],which was consistent with the first-principle studies by *Matsunaga* [127]. Furthermore, *Bigi and co-workers* suggested the possible locations for the presence of excess Mg content, which were adsorbed on the surface of apatite crystallites and / or presented in the amorphous phase [129]. *Bigi and co-workers* indicated that the small decreases in the *c*-axis associated with an irregular change of the a-axis in the apatite samples with increased Mg substitution from 0 to 30 atom % [92]. On the other hand, *Yasukawa and co-workers*

reported that the unit cell dimensions of *a* and *c* exhibited almost linearly decreasing trend with increased Mg substitution from 0 to 0.31 [93].

1.3.2.3.   Sr-HA

Unlike the trace elements of Zn, and Mg, the synthesis of phase pure apatite can be achieved with the incorporation of Sr substitution in the whole range of composition [20].

It was reported that the larger cation of Sr (1.18Å) substituted in the HA structure for the smaller cation of Ca (1.00 Å) [20], due to the size difference between these two cations, the modifications of the lattice parameters of HA were therefore expected [20, 95, 130]. *Li and co-workers* reported that both HA and Sr-HA sample belong to hexagonal system, $P6_3/m$, and the parameters of *a* and *c* both slightly increased with increased Sr substitution from 0 to 15% [130]. In addition, *O'Donnell's* [95] and *Bigi's* report [20] agreed well with *Li's* work [130], and they further indicated that the apatite samples with increased Sr substitution in the range from 0 to 100 mol% led to the linearly increases in both parameters of *a* and *c* of the HA lattice structure [20, 95].

In order to clarify the exact location of Sr for Ca in the HA structure, a large number of works were concentrated on this specific purpose were carried out [20, 95, 130-132]. *Kikushi and co-workers* suggested the hydrothermally derived Sr-HA sample with 1.92 atom % Sr exhibited the preferential site of Sr in HA structure was at Ca-I site [131]. On the other hand, *Li and co-workers* found their Sr-HA samples with Sr concentration, varied from 0 to 15%, were preferred to be exchanged with the Ca at Ca-II site [130]. Due to the different opinions were presented regarding to the actual locations of Sr for Ca, *Bigi and co-workers* tend to give an integrated answers [20] for the above debates [130, 131]. They indicated that the occupation of Ca-I site was more favoured when the Sr substitution at very low level, as the Sr substitution was increased, the preferential

site of Sr in HA structure was inverted from Ca-I to Ca-II site [20]. *Terra and co-workers* provided more precise information about Sr locations in the HA structure by using the combination of first-principles modelling and the experimental methods [132]. They found that the apatite sample with Sr concentration below 1 atom%, the Sr was favoured in Ca-I site over Ca-II site [132].When the Sr substitution reached about 5 atom %, the ideal statistical occupancy ratio of Sr2/Sr1 was 1.5, and the Ca-II site was progressively favoured to be occupied as Sr substitution was further increased [132].

1.3.2.4.　Si-HA

Many literatures indicated that with the incorporation of Si into HA materials did not induce direct changes in the crystallographic structure or crystallinity, as similar XRD patterns were observed in the HA samples with different Si substitution, ranging from 0 to 1.5 wt% [96, 97, 133, 134]. In order to maintain the apatite structure, the substituting limits of Si (SiO_4^{4-}) for P (PO_4^{3-}) [134] was suggested to be presented in the region of approximately 2-3 wt% [96, 97, 135].

On the other hand, the presence of Si substitution did exhibit the certain degree of modifications in the HA lattice parameters [96, 97, 133, 134]. One main mechanism of with the incorporation of Si into HA structure was proposed as that, the loss in the OH^- groups in order to compensate the extra negative charge induced by the substitution of SiO_4^{4-} for PO_4^{3-} in the HA structure [96, 97]. They both agreed that with increased Si substitution in the region of 0-1.5 wt%, small decreases and increases in the HA lattice parameters of *a* and *c*, and resulted in the slightly decreases in the cell volume of HA unit lattice [96, 97]. On the contrary, *Leventouri and co-workers* suggested that the HA unit cell with 0.4 wt% Si expanded by approximately 0.09% due to a 0.1% increases in the lattice parameter *c*, by using neutron diffraction technique [133]. Based on the neutron diffraction results, the further reduction of 13 % OH occupancy site were observed due to the charge difference caused by the substitution of SiO_4^{4-} for PO_4^{3-}

[133]. Although no remarkable changes were observed in the interatomic distance of PO_4 tetrahedron due to the presence of Si substitution, the angle distortion index (DI) was increased by 0.2% as Si substitution increased to 0.4 wt% for phosphorus in HA lattice [133].

1.3.2.5. CO_3-HA

Different as most of substitutions, such as Zn, Mg, Sr, and Si, CO_3^{2-} content was reported to be able to exchange with two possible sites in the HA structure, they were OH^- channel site and PO_4^{3-} tetrahedra, and denoted as A-type CO_3^{2-} substitution and B-type CO_3^{2-} substitution, respectively [81].

As CO_3^{2-} substitution entered into different site of HA lattice, the opposite effects on the *a*-axis and *c*-axis dimensions were noticed [101, 136]. *Legeros and co-workers* reported that with the incorporation of A-type CO_3^{2-} substitution, the lattice parameters of *a* and *c* was increased and decreased, respectively [136]. On the other hand, *Nelson and co-workers* investigated the effect of B-type CO_3^{2-} substitution in the HA lattice, the decreased *a* and increased *c* was observed [101]. Furthermore, it was worth to note that sometimes the increased lattice constant *a* was found in B-type CO_3^{2-} substituted HA sample, and that was likely attributed to incorporation of lattice H_2O or some HPO_4^{2-} [137, 138].

It is known that the biological apatites were actually composed of both A-type and B-type CO_3^{2-} substitution, which CO_3^{2-} substitution mainly exchanged with PO_4^{3-} tetrahedra, and only amount of CO_3^{2-} substituted OH^- groups [137]. An interesting mechanism due to the CO_3^{2-} incorporation into the biological apatite was proposed by *Legros and co-workers* [139]. As illustrated in Figure 22, the formation of a vacancy in O-III or O-III', was assumed, while PO_4^{3-} was exchanged with CO_3^{2-} [139]. In order to maintain the charge balance in the whole HA structure, the negative charge due to the

vacancy of O-III or O-III' was positively charged by releasing one Ca^{2+} and one OH^- [139].
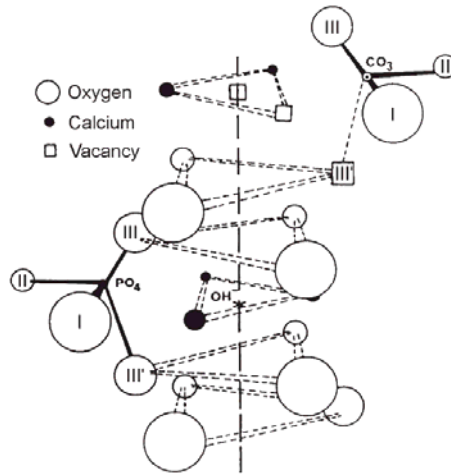
Figure 22: The schematic diagram of CO_3^{2-} substituted HA structure [140].

Similar to Zn, Mg and Si, there was a substituting limits of CO_3^{2-} substitution in the HA structure [82, 100]. When the CO_3^{2-} content beyond the substituting limits, the possible locations of excess amount of CO_3^{2-} content were suggested either to locate in the hydrated layer of the crystals [82] and / or present in the amorphous $CaCO_3$ [46]. Alternatively, it destabilized HA structure and encouraged to the formation of biphasic ceramics [100].

1.3.3. Application of synthetic substituted HA

1.3.3.1. Zn-HA

Zn is an important trace element in many animals [104], and it exists in the human bones ranging from 0.0126 to 0.0217 wt% [141].

In order to study the effect of Zn addition in a biological system, *Kawamura and co-workers* demonstrated a *vivo* studies by implanting composite ceramics of Zn-TCP/HA in the femora of New Zealand White rabbits for 4 weeks [104]. They found that such material with the presence of 0.633 wt% Zn exhibited increasing effect on the bone resorption, whereas when Zn concentration reached to 0.316 wt% in the calcium phosphate ceramics, it promoted the formation of bone [104].

Grandjean-Laquerriere and co-workers reported, that the addition of Zn content in HA led to a decrease in the inflammatory reaction [105]. *Li and co-workers* suggested that Zn substituted HA could consist a new generation of biomaterials for bone tissue engineering [89].

1.3.3.2. Mg-HA

Mg is of the essential substitutions in the biological apatite, and it present with the concentration at 0.44, 1.23, and 0.72 wt% in enamel, dentin and bone, respectively [83]. *Rercival* reported that the Mg deficiency exhibited a negative effect in all stages of skeletal metabolism, such as decreased osteoblastic and osteoclastic activities, and etc [142]. Due to the great importance of Mg content, the incorporation of Mg into HA was proposed to be used in orthopaedic and dental applications [106]. *Bonfield and Gibson* prepared bone mimetic HA ceramics with the co-incorporation of Mg and CO_3^{2-} content up to 0.5 and 1 wt%, respectively, by using precipitation method. They

expected that the resulted materials exhibited better bioactivity over pure HA, which was applied in the commercial application, such as bone implant fabrication [107]. *Dolci and co-workers* indicated that the nano-sized Mg-HA material with Mg concentration up to 25.4wt% was possible to be employed in odontostomatologic applications [108].

1.3.3.3. Sr-HA

The level of Ca, Mg, Sr element presented in the in the body of a 70-kg standard man was 1.4, 0.027, and 0.00044 wt%, respectively, which was compiled by *Nielsen* [143]. Although the concentration of Sr existed in the human body was scarce [143], the increased attention was noticed in the Sr-containing drug, such as Sr ranelate compound, which gave the positive effects combined of stimulating effect in the bone formation and decreasing effect in the bone resorption [109].

Clinical trials, that were successfully performed in female post-menopausal osteoporotic patients, led to the conclusion that an intake of 2g Sr-Ranelate per day appeared to reduce the risk of vertebral fracture effectively [109].

1.3.3.4. Si-HA

Schwarz reported that the Si concentration in biological systems varies based on the data collected from bone (100 ppm), serum (~1 ppm), and cartilage as well as other connective tissues (200-600 ppm) [144]. *Carlisle* also reported the essential involvement of Si element in bone formation and calcification [145] and *Schwarz and Milne* investigated that Si deficiency in rats led to the deformations of skull [146].

Thian and co-workers conducted in *vitro* studies and reported that the presence of Si in HA increased and promoted osteoblast-like activity [110]. Hence, they suggested that

further medical application for Si substituted HA can be in both hard and soft tissue replacement [110].

In *vivo* studies by *Porter and co-workers* showed that the dissolution rate of HA was increased with increasing Si substitution due to the formation of defects in the grain boundaries [111]. They suggested that increased dissolution was essential to improve the bioactivity of the material [111]. The incorporation of Si into HA seems to be a promising way to improve bioactivity [110-112].

1.3.3.5.   CO$_3$-HA

The CO$_3^{2-}$ ions tend to appear as one of the most important substitutions [82-84], present in the HA due to its high similarities to the mineral component of hard tissues [82, 114]. *Legeros* indicated that with the addition of CO$_3^{2-}$ content in HA material, the crystallinity was decreased, whereas the solubility was increased, observed in both *vitro* and *vivo* studies [83]. *Gibson and Bonfield* suggested that with the incorporation of CO$_3^{2-}$ content into HA ceramics can increase osseointegration rate of HA in their applications, such as bone grafting [114]. *Li and co-workers* prepared nano-sized HA with the presence of both A-type and B-type CO$_3^{2-}$ substitution by using wet method [113].They proposed such apatite material potentially can be applied as a tissue engineering scaffold [113].

1.4. Aim and objectives

1.4.1. Aim

The aim of this project is to study the effect of ionic substitutions on the apatite structure emphasising changes in the crystallite size and the degree of crystallinity of apatite samples produced by a chemical precipitation, a hydrothermal method and a biological method (bacterial synthesis).

1.4.2. Objectives

In order to achieve the aim of this project, as described above, three objectives are required to be accomplished, and they are listed below.

(1) To apply different synthesis methods in order to obtain different apatite samples.

(2) To characterize the structure of synthesised apatites by using different techniques including XRD, FTIR, Raman spectroscopy and ^{31}P MAS-NMR.

(3) To develop an understanding about the relationship between the ionic substitutions and the structural properties of apatite materials such as crystallite size and degree of crystallinity.

2. Experimental procedures

2.1. Sample preparation

20 samples were prepared by using three different methods; hydrothermal method (S1-S14), chemical precipitation method (S15-S19), and bacterial biosynthesis (S20). The phase and composition of synthesized samples from different methods are summarized in Table 2. It is worth noting that the first 14 samples were prepared by the University College London (UCL), Dr. Jawwad Darr's group. Additionally, they also provided a general description of the first 14 samples shown in Table 2. Furthermore, they indicated most of the measurements within these 14 samples were conducted by using a calibrated EDS detector attached to an SEM, besides the sample 14, which was measure by TGA, indicated by symbol *.

2.1.1. Hydrothermal method

As mentioned previously, the first 14 samples were provided by UCL and were prepared by using a continuous hydrothermal flow system, as shown in Figure 23 [15].
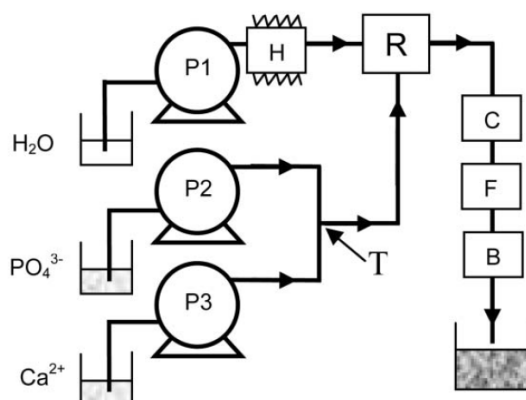
Figure 23: The schematic diagram showing the first 14 samples (S1-S14) synthesized via a continuous hydrothermal flow system [15].

Table 2: Description of 20 samples prepared by three different approaches.

Method	Sample	Phase	Composition	Measured value
Hydrothermal method	S1	Mg-HA	0.5wt%Mg expected in sample	0.7 wt% Mg
	S2	biphasic: MgHA+Mg-whitlockite	1.5wt%Mg expected in sample	1.6 wt% Mg
	S3	Mg-whitlockite	6wt%Mg expected in sample	5.8 wt% Mg
	S4	amorphous Mg-whitlockite	10wt%Mg expected in sample	9.1 wt% Mg
	S5	HA with 1.67 ratio (in reactor)	Making HA with ratio 2.0 in our reactor results in improved thermal stability i.e. with 2.0 ratio HA doesn't form TCP up to 1000 degrees	Ca/P ratio of 1.39
	S6	HA with 2.0 ratio (in reactor)		Ca/P ratio of 1.42
	S7	Zn-HA	extrapolation of Zinc content should be around 2.6 wt%	-
	S8	Si-HA	S8 means an expected silicon content of 1wt%, 2wt% for S9 and so on. XRD shows all of these to be HA. NMR for S12 shows more than one silicon environment.	0.26 wt% Si
	S9	Si-HA		0.39 wt% Si
	S10	Si-HA		0.56 wt% Si
	S11	Si-HA		0.53 wt% Si
	S12	Si-HA		0.81 wt% Si
	S13	CO_3-HA	around 5wt% carbonate content	5 wt% CO_3 *
	S14	CO_3-HA + $CaCO_3$	we use urea as a carbonate source in our reactor, a higher amount of urea results in a biphasic mixture of CO_3-HA and $CaCO_3$ (Calcite)	around 21 wt% CO_3
Chemical precipitation method	S15	HA	0 mol% Sr	-
	S16	Sr-HA	25 mol% Sr	-
	S17	Sr-HA	50 mol% Sr	-
	S18	Sr-HA	75 mol% Sr	-
	S19	Sr-apatite	100 mol% Sr	-
Bacterial biosynthesis	S20	Biological HA	CO_3 substitutions expected in the biological HA	-

* measured by TGA

During the synthesis, the basic solution of calcium nitrate and diammonium hydrogen phosphate was pumped from P2 and P3 to meet at point "T", as showed in Figure 23 [15]. The pH of the reaction was adjusted to 10-11 by adding ammonium hydroxide [15]. The temperature and pressure was maintained at 400C° and 240MPa, respectively. The mixed solution was transferred to meet superheated water at point "R", where the rapid ageing was occurred. The mixed solution was then passing through the point "C" (in-line cooler) for the cooling and "F" (a 7μ filter) for the filtering, and then the apatite suspension was collected at point "B" (back-pressure regulator) [15]. Finally, the collected particles were centrifuged and freeze-dried prior the characterization [15].

For synthetic substituted HA samples, different substitution sources were added into the basic solutions, as shown in Table 3.

Table 3: The added different reactants for producing Mg-HA, Zn-HA, Si-HA and CO_3-HA samples.

Sample	Phase	Substitution sources	
S1	Mg-HA	calcium nitrate	Mg nitrate was added into diammonium hydrogen phosphate
S2	biphasic: MgHA+Mg-whitlockite		
S3	Mg-whitlockite		
S4	amorphous Mg-whitlockite		
S7	Zn-HA	calcium nitrate	Zn nitrate was added into diammonium hydrogen phosphate
S8	Si-HA	silicon tetraacetate was added into calcium nitrate	diammonium hydrogen phosphate
S9	Si-HA		
S10	Si-HA		
S11	Si-HA		
S12	Si-HA		
S13	CO_3-HA	calcium nitrate	urea was added into diammonium hydrogen phosphate
S14	CO_3-HA + $CaCO_3$		

2.1.2. Chemical precipitation method

Five Sr-HA samples (S15-S19) were prepared with Sr substitution in the solution ranging from 0 to 100 mol%, by using chemical precipitation method, which was previously reported by *Bigi and co-workers* [20].

During the synthesis, appropriate amount of reactants of $Ca(NO_3)_2 \cdot 4H_2O$ and $Sr(NO_3)_2$, and $(NH_4)_2HPO_4$ were used in order to form solution A and solution B. The weights of reactants were used to prepare Sr-HA samples are summarized in Table 4.

Table 4: The weights of reactants for chemical precipitation method for a series of (Sr_xCa_{1-x}) $5(PO_4)_3OH$ samples, where x varied from 0 to 1.

Sr (x)	$Ca(NO_3)_2 \cdot 4H_2O$	wt.%	mol%	$Sr(NO_3)_2$	wt.%	mol%	$(NH_4)_2HPO_4$	wt.%	mol%
0	15.3 g	74.63	62.20	0g	-	-	5.2g	25.37	37.80
0.25	11.5g	57.21	46.76	3.4g	16.92	15.43	5.2g	25.87	37.81
0.5	7.7g	38.89	31.18	6.9g	34.85	31.17	5.2g	26.26	37.65
0.75	3.8g	19.69	15.45	10.3g	53.37	46.74	5.2g	26.94	37.81
1	0g	-	-	13.7g	72.49	62.18	5.2g	27.51	37.82

Solution A was prepared by dissolving proper amount of $Ca(NO_3)_2 \cdot 4H_2O$ and /or $Sr(NO_3)_2$ in 60ml distill water, depending on the required composition. The total concentration of $[Ca^{2+}] + [Sr^{2+}]$ of solution A was kept at 1.08M. The pH value of the solution A was maintained at 10 by using NH_4OH. As shown in Figure 24, the 50 ml solution A was transferred into a three-neck flask, and then was heated at 90℃. Solution B was formed by dissolving $(NH_4)_2HPO_4$ in 60ml distilled water. Again, the pH of solution B was adjusted to 10 by using NH_4OH. Then 50 ml solution B was taken and poured into solution A from the top of the condenser. The mixed A-B solution was heated and stirred at 90℃ for 5h.
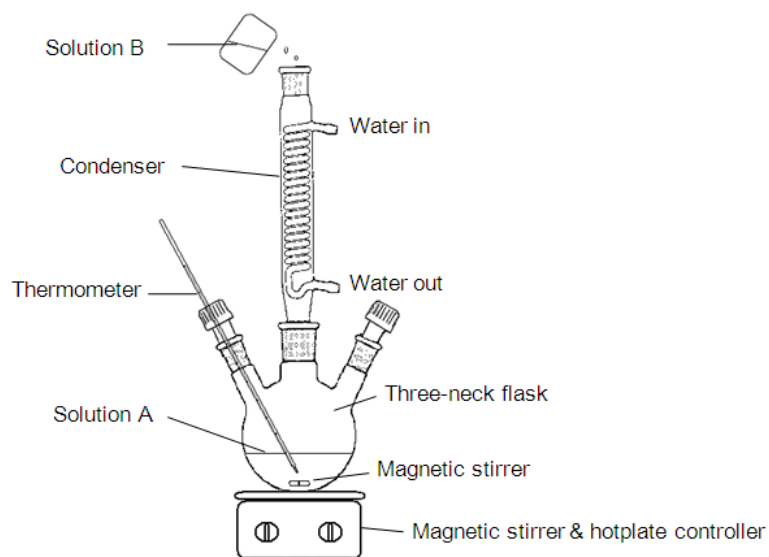
Figure 24: The schematic diagram showing the experimental equipment setup, used for the preparation of Sr-HA samples (S15-S19) via a chemical precipitation method.

In order to obtain precipitates, the resulted solutions were centrifuged for 13mins with rate of 100000rpm at room temperature. Then the formed precipitates were washed with distill water up to 10 times. Finally, the washed precipitates were dried overnight in air. Enable to be characterized by different techniques, the dried HA precipitates were grounded into the powders.

2.1.3. Bacterial biosynthesis

The biological HA sample (S20) was provided by master student, *Bagheriasl*, who produced biological HA by using bacterial biosynthesis [26]. The details of this biological HA and its experimental procedures were precisely recorded in his thesis in 2008 [26]. During the bacterial biosynthesis, an appropriate amount of Serratia sp, glycerol 2-phosphate (G2P), calcium chloride ($CaCl_2$), and sodium citrate were applied [26], and the weights of the starting material and resulted biological HA are listed in Table 5.

Table 5: Weight, or concentration and volume of the relevant materials were used to produce biological HA through the bacterial precipitation method [26].

	Serratia sp	G2P	CaCl$_2$	Sodium citrate	Biological HA
Dry weight (mg)	367	-	-	-	2200-2600
Concentration (mM)	-	10	4	2	-
Volume (ml)	-	7.44	7.44	7.44	-

In general, the bacterial, *Serratia*. sp, was fed daily by adding 7.44ml of each additive, 10mM G2P, 4mM $CaCl_2$, and 2mM sodium citrate [26]. In order to obtain the precipitates of biological HA on the surface of bacterial, *Serratia*. sp was cultured for 9 days by using same additives with the same quantities [26], as shown in Table 7. The feeding was carried out at room temperature, and the pH of the reaction was maintained at 9.2 [26].

2.2. Characterisation

2.2.1. X-Ray Diffraction (XRD)

The phase composition was characterized by using X-ray diffraction (XRD) with a Bruker D8 Advance, with Cu-Kα radiation, 40kV/40mA, λ = 1.5406 nm. The average crystallite size was calculated by using the Scherrer equation, as represented in Equation 11 [147].

$$d = 0.95\lambda / (\beta \cos(\theta)) \qquad (11)$$

Where λ is wavelength (~1.541Å), β is the breadth (in 2θ radians) for a given reflection (hkl), and 2θ is the diffraction angle.

For the biphasic samples, including S2, and S14, the phase composition was calculated by the intensities of the strongest peaks, using the equation 12 [147].

$$W_m = 1 / (1 + 0.88(I_s / I_m)) \qquad (12)$$

Where I_m is the strongest peak intensity of main phase, and I_s is the strongest peak intensity of secondary phase. As there are three samples containing two different phases, the strongest peak intensity of the main phase and the secondary phase of these three samples are summarized in Table 6.

Table 6: The strongest peak intensity of the main phase and the secondary phase of two samples.

Sample	Main phase	Secondary phase	I_m (°)	I_s (°)
S2	HA	Mg-whitlockite	31.8	31.3
S14	HA	$CaCO_3$	31.8	29.4

2.2.2. ^{31}P MAS-NMR

The ^{31}P MAS-NMR measurements were conducted at a resonance frequency of 81.0 MHz by using the Bruker 200 MHz (4.7 T) spectrometer. The sample powder was packed into 4 mm zirconia rotor. The spinning rate of the samples at a magic angle was approximately 4.5 kHz. The recycle time was 49 s for ^{31}P MAS-NMR. The reference material for the chemical shift (in ppm) was 85 % H_3PO_4 for ^{31}P and its chemical shift was adjusted to 0 ppm.

2.2.3. Fourier Transform Infra-red Spectroscopy (FTIR)

The functional groups were characterized by FTIR technique using Nicolet 8600 FTIR spectrometer. FTIR spectra were recorded from 400 to 4000 cm^{-1} at 4 cm^{-1} resolution averaging 100 scans. 2 mg of each sample was mixed with 300 mg of KBr and was pressed into a disk for the measurement.

2.2.4. Raman Spectroscopy

The functional groups were characterized by Raman spectroscopy using Ramanscope-1000, with an excitation wavelength of $\lambda_{ex} = 633$ nm.

3. Results and Discussion

3.1. Effect of synthesis on the apatite structure

3.1.1. X-ray diffraction studies

Figure 25 shows the powder XRD patterns of four different samples, S15, S20, S5 and S6, which were prepared by using the chemical precipitation method, bacterial biosynthesis and hydrothermal method, respectively. According to the XRD measurements, the above four samples are identified as single phase HA. All four HA samples exhibit XRD patterns that are in good agreement with the HA pattern reported by *Koutsopoulos* [29].
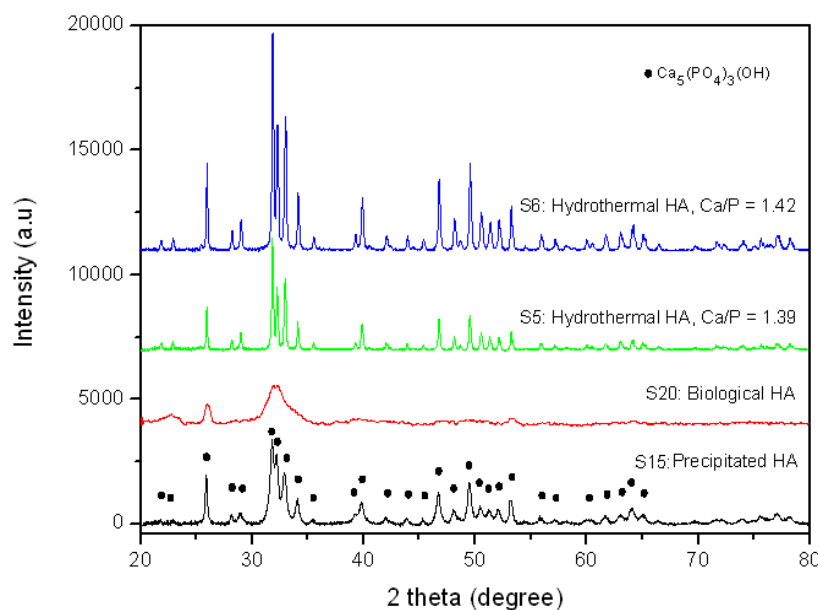
Figure 25: Powder XRD patterns of four different HA samples: (S15) precipitated HA, (S20) biological HA, (S5) hydrothermal HA, Ca/P = 1.39, (S6) hydrothermal HA, Ca/P = 1.42.

As presented in Figure 25, the biological HA sample S20 exhibits the broadest peaks with the lowest intensity compared to the XRD patterns of all other HA samples. On the

other hand, the sharpest peaks with the highest intensity are observed in the XRD patterns of S5 and S6, which have different Ca/P values and were prepared by a hydrothermal method. The precipitated HA S15 exhibits an intermediate size of peak intensity and peak width compared to the biological HA and the two hydrothermally derived HA samples. The above differences in peak width and peak height were also observed by other researchers [36, 78, 79, 148-150]. *Posner* observed a significant peak broadening together with a decrease in the peak intensity of the XRD patterns, associated with decreased HA crystallite size [78]. In addition, *Harper and Posner* found that the bone mineral HA exhibited much lower peak intensities compared to a synthetic crystalline HA [79]. They suggested, that the lower peak intensity observed in the case of bone mineral HA was due to the presence of a relatively large amount of disordered phase, referred to as a phase of smaller degree of crystallinity [79]. As a consequence, the smallest peak width together with the lowest peak intensity exhibited in the biological HA are most likely due to the smaller size of HA crystals associated with lower degree of crystallinity in comparison to the other three HA samples.

In order to confirm the above, the crystallite size of all four different HA samples were calculated from the XRD data by using the Scherrer equation and are presented in Table 7. As shown in Table 7, the crystallite size of the four HA samples can be arranged in the order of S20< S15 <S6 <S5. In the case of S5 and S6 the crystallite size difference is small. It is worth noticing, that both samples were prepared by the hydrothermal method and therefore it is reasonable to conclude that HA crystal size is strongly dependent on the synthesis method.

Apart from using the chemical precipitation method, bacterial biosynthesis, or hydrothermal method, there are many other techniques reported in the literature used to prepare HA [10, 24, 151]. *Silva and co-workers* produced HA powders by using a mechanical alloying method [10]. They reported that the resulted HA powders exhibited nanocrystalline features with a crystallite size of 22-39 nm [10]. *Kim and Kumta* prepared nanostructured HA powders by using a simple sol-gel approach [24]. Upon the heat-treatment at 900 °C for 12h, a single phase of HA was obtained with crystallite size in the range of 50 to 150 nm [24]. *Siddharthan and co-workers* prepared HA particles by using a microwave irradiation technique [151]. They reported, that the resulted material was a calcium deficient HA (CDHA), which exhibited a crystallite

length of 16-39 nm and width of 7-16 nm [151].

Table 7: Synthesis, phase identification, and crystallite size of four different HA samples.

Sample	Description	Synthesis	Phase identification	Crystallite size (nm)
S15	Chemical precipitated HA	Chemical precipitation	HA	16
S20	Biological HA	Bacterial biosynthesis	HA	8
S5	Hydrothermal HA, Ca/P = 1.39	Hydrothermal	HA	42
S6	Hydrothermal HA, Ca/P = 1.42	Hydrothermal	HA	39

According to the literature [10, 24, 151], it seems that different HA synthesis methods resulted in different HA crystallite size as well as in other crystal characteristics. Comparing our HA reported in this work with HA reported in the literature [10, 24, 151], the biological HA (sample S20) remains the one that has the smallest crystallite size associated also with poor crystallinity. *Fathi and co-workers* [150] and *Webster and co-workers* [4] reported, that small crystallite domains and poor crystallinity of HA result in a better contact reaction and stability at the interface between the implanted HA and the natural bone as well as in greater promotion effect on the early bone in-growth, and consequently S20 may be a good candidate for this type of application. On the other hand, there were numerous research papers [12-14, 148, 152, 153], that reported hydrothermal, chemical precipitation and bacterial synthesis of HA similar to the methods reported in this work. The characteristics of the HA crystal formed were different compared to the HA samples in our studies [12-14, 148, 152, 153]. Hence, this leads to review the details of each synthesis in order to understand the main driving force that caused the differences in the HA characteristics, in particular the HA crystallite size and degree of crystallinity. As suggested in the literature [13, 14, 36], the HA characteristics were highly dependent on the following factors: temperature, pH, time and reactants concentration. Thus, in order to study the effect of different synthesis methods on the crystallite size of HA and perhaps also the crystallinity, the above mentioned factors for the four different HA samples studied in this work are listed in Table 8.

Table 8: Methods, factors and crystallite size for four different HA samples: (S15) precipitated HA, (S20) biological HA, (S5) hydrothermal HA, Ca/P = 1.39, and (S6) hydrothermal HA, Ca/P = 1.42.

Sample	Method	Reactants	Synthesis temperature (°C)	Processing time	pH	Crystallite size (nm)
S5	Hydrothermal	$Ca(NO_3)_2$, $(NH_4)_2HPO_4$	400	very short	10-11	42
S6						39
S15	Chemical precipitation	$Ca(NO_3)_2 \cdot 4H_2O$, $(NH_4)_2HPO_4$	90	5 hours	10	16
S20	Bacterial biosynthesis	Serratia. Sp, G2P, $CaCl_2$, Sodium citrate	25	9 days	9.2	8

As shown in Table 8, decreasing the temperature from 400 to 25°C, increasing the processing time up to 9 days, and slightly decreasing the pH of the reaction from 10-11 to 9.2, leads to a decrease in the HA crystallite size from 42 to 8 nm. Although all the above four factors seem to influence the HA crystal size, *Shi* reported that the temperature must have an important influence on the crystal growth and consequently the crystallite size of HA taking into consideration the equation 13 [154]:

$$\text{Crystal growth rate } \propto \exp\left(-\frac{E_a}{kT}\right)$$

(13)

where E_a = activation energy, k = reaction rate constant, and T = temperature [154].

In the current studies, the hydrothermally derived HA samples (S5 and S6) were produced at higher temperature and had larger crystallite size than that of the chemical precipitated HA (S15). The effect of temperature on the HA crystallite size was also investigated by other authors, who observed similar changes in the crystallite size [36, 148]. For example, *Prakash and co-workers* found that during an acid-base reaction precipitation of HA increasing the reaction temperature from 45 to 100°C resulted in an increase in the crystallite size and the degree of crystallinity of the produced HA, evidenced by XRD [36]. As reported by *Mobasherpour and co-workers*, the crystallite size of HA produced by a precipitation method increased with increasing the

heat-treatment temperature from 100 to 1200°C [148]. Furthermore, *Kothapalli and co-workers* also suggested that increasing the reaction precipitation temperature induced an increase in the HA crystallinity, as indicated by the increased peak intensity in the XRD patterns of HA [33].

The biological HA produced during the present work should be considered however a different case, due to its unique apatite formation mechanism. As described in *2.1.3*, the biological HA was precipitated and obtained at the surface of bacteria via a complicated biological process that involved feeding of different substances at fixed quantities and therefore the size and the degree of crystallinity of the biological HA would be expected to be more dependent on the conditions of the biological process [26, 155]. In addition, it is generally accepted that the biological apatite crystal size is always smaller than the crystal size of the synthetic apatite.

3.1.2. FTIR spectroscopy studies

Figure 26 shows the FTIR spectra of four HA samples prepared by using three different preparation methods. The absorption band positions and their assignments are summarized in Table 9. As observed in Figure 26, the two intense absorption bands that appear at 1029 and ~1095 cm^{-1} are due to the stretching vibration mode v_3 of P-O, whereas the absorption band that appears at 963 cm^{-1} is associated with the stretching vibration mode v_1 of P-O [36, 156-158].
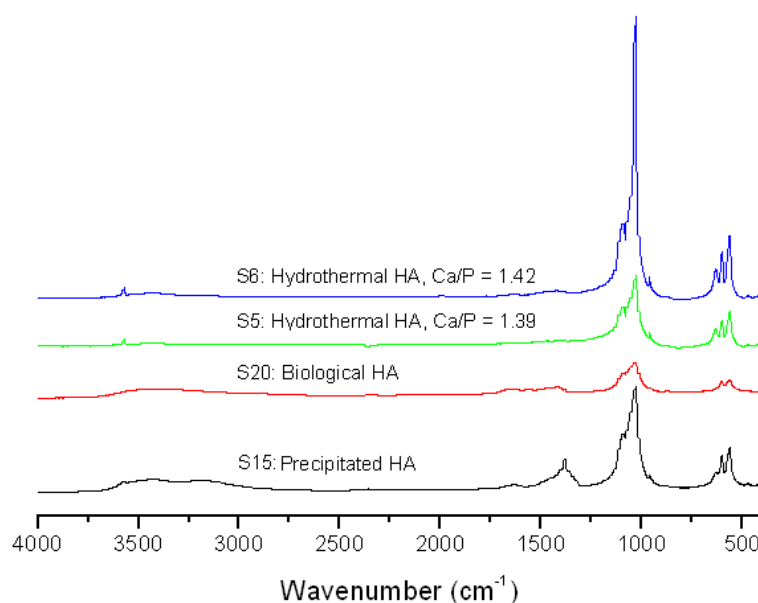
Figure 26: FTIR spectra of four different HA samples: (S15) chemical precipitated HA, (S20) biological HA, (S5) hydrothermal HA, Ca/P = 1.39, (S6) hydrothermal HA, Ca/P = 1.42.

The doublet present at around 601-561 cm^{-1} is attributed to the O-P-O bending mode v_4, whereas a small band at around 470 cm^{-1} is ascribed to the O-P-O bending mode v_2 [36, 156-158].

As shown in Figure 27 (a) and (b), the stretching and libration mode of OH$^-$ appear at 3571 and 634 cm^{-1}, respectively [20, 36, 148, 157] and are observed in all cases, except of S20, the biological HA sample. A similar FTIR spectrum of biological HA was reported by *Sammons and co-workers*, who also observed the lack of the OH$^-$ stretching

and libration mode in the spectrum of biological HA [156].
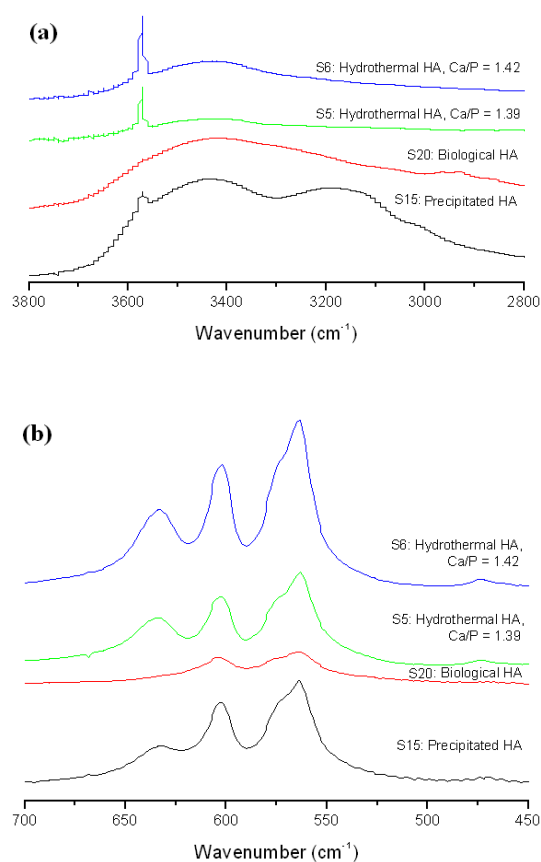
Figure 27: FTIR spectra of four different HA samples (a) in the region of 3800-2800 cm-1 and (b) in the region of 700-450 cm^{-1}.

In the case of biological HA, S20, the HA structure is slightly different compared to the synthetic HA most likely due to the presence of CO_3^{2-} ions in the OH$^-$ column site, evidenced by the presence of the characteristic bands at 1562 and 1582 cm^{-1} associated with A-type CO_3^{2-} [158]. In addition, the absorption bands at around 878 cm^{-1} and in the region of 1411-1450 cm^{-1} that are observed in all cases, are assigned to B-type CO_3^{2-} vibration mode v_2 and v_3 [113, 159, 160]. It is suggested that a certain amount of CO_3^{2-} ions are also present in the PO_4^{3-} tetrahedra within the HA structure [83, 120]. Due to the lack of CO_3^{2-} sources during the synthesis of all HA samples under study with the exception of hydrothermal HA, the incorporation of CO_3^{2-} ions into the HA structure for the HA samples is caused probably by carrying out all the experimental steps in air [106], and hence the amount of the incorporated CO_3^{2-} ions are expected in small quantities. In the case of S20, the presence of both A-type and B-type CO_3^{2-} however is

expected to be originated from the biological process during bio-mineralisation. The hydrothermal HA on the other hand, exhibits a small amount of CO_3^{2-} most likely because of impurities contained in the starting materials as they were not degassed prior to use them.

The broad asymmetric bands in the range of 3431 to 3010 cm^{-1} together with an absorption band centred at approximately 1634 cm^{-1} are assigned to the presence of adsorbed water molecules on the HA crystallite surface [158, 161] and are observed in all samples. As observed in Figure 27 (a), such water bands are particularly large in the case of S15 and S20 reflecting probably the lower reaction temperatures used during the synthesis of precipitated HA and biological HA [89, 133], in contrast with the hydrothermally derived HA samples.

The FTIR spectra of all four different HA samples in the region from 900 to 800 cm^{-1} are shown in Figure 28. As observed in Figure 28, a common absorption band at around 878 cm^{-1} is present in all cases, whereas two additional bands at 826 and 831 cm^{-1} are only present in the case of S15, the precipitated HA sample. *Raynaud and co-workers* suggested that the absorption bands at 820 and 1380 cm^{-1} were attributed to the presence of residual nitrate groups [152]. Similarly, *Kannan and co-workers* indicated that the band at 875 cm^{-1} can be assigned to the presence of nitrates and other residual species, such as NO_3^- and NH_4^+, which were possibly originated from precursors or reactants used during the synthesis [161].
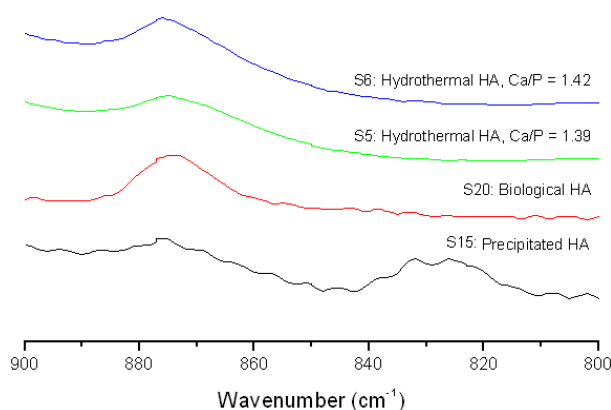
Figure 28: The FTIR spectra of four HA samples in the region of 900-800 cm^{-1}.

Considering the presence of a band at approximately 1384 cm^{-1} observed in the case of S5, S6 and S15, in addition to the bands at around 871 or/ and 831, and 826 cm^{-1}, one can suggest that nitrates or other residual species, such as NO_3^- and NH_4^+, are likely to be present in the HA structure. It is interesting to mention, that the absorption band at around 871 cm^{-1} has been also assigned to the presence of CO_3^{2-} substitution [151, 152, 162]. *Raynaud and co-workers* reported that the band at 875 cm^{-1} was ascribed to the presence of HPO_4^{2-}, which suggested the formation of calcium deficient HA [152, 162]. *Siddharthan and co-workers* reported that the conversion of HPO_4^{2-} to $P_2O_7^{4-}$ was occurred when the HA sample was heat-treated above 200°C shown by the appearance of a band at 725 cm^{-1} [151]. *Raynaud and co-workers* further reported that $P_2O_7^{4-}$ band appeared at 720 cm^{-1} when the HA sample was heat treated at 400°C [152]. In the present work, an absorption band at around 871 cm^{-1} is observed in all samples. Considering, that the hydrothermally synthesized HA samples do not exhibit a band at 725 cm^{-1} assigned to the presence of $P_2O_7^{4-}$, it is suggested that most likely the band at around 871 cm^{-1} is attributed to the presence of CO_3^{2-} ions or/ and nitrates and other residual species in the apatite structure without of course ruling out the possibility that a small amount of HPO_4^{2-} groups might be present, especially in the case of S15 and S20. The presence of HPO_4^{2-} groups in the case of S20 was also confirmed by *Sammons and co-workers*, who reported a similar peak at 870 cm^{-1} assigned to HPO_4^{2-} in a biological HA sample [156].

It is also worth noticing, that three additional bands at 2851, 2924, and 2964 cm^{-1} are present in the biological HA sample (S20). Similar bands were also observed in the FTIR spectra of the biological HA samples synthesized by *Sammons and co-workers* [156]. *Li and co-workers* suggested that the band at 2880 cm^{-1} can be assigned to the CH_2 stretching vibrations in poly-ethylene-glycol (PEG) [113], and therefore the above mentioned three additional bands observed in the FTIR spectrum of S20 were initially considered as vibrations originated by organic elements present on the bacterial cell walls. However, *Sammons and co-workers* sintered the bacterially derived HA sample at 1200 C°, but the bands around 2940 cm^{-1} were still present [156]. It was expected that at 1200°C all organic elements would not be present indicating that the peaks around 2940 cm^{-1} are unlikely to be due to the presence of organic elements. Further investigation is required in order to assign these bands in the biological HA (S20).

Table 9: Assignment of the main peaks in the FTIR spectra of (S15) precipitated HA, (S20) biological HA, (S5) hydrothermal HA, Ca/P = 1.39 and (S6) hydrothermal HA, Ca/P = 1.42.

S15: Precipitated HA	S20: Biological HA	S5: Hydrothermal HA, Ca/P = 1.39	S6: Hydrothermal HA, Ca/P = 1.42	Assignment	Reference
470	470	476	476	O-P-O bending mode v_2	[36, 156-158]
561-601	568-601	561-601	561-601	O-P-O bending mode v_4	[36, 156-158]
634	-	634	634	OH$^-$ libration mode	[20, 36, 148, 157]
878	878	871	871	B-type CO_3^{2-} vibration mode v_2 / HPO_4^{2-}	[113, 159, 160]/ [152, 156, 162]
963	963	963	963	P-O stretching vibration mode v_1	[36, 156-158]
826, 831, 878, 1378	-	871, 1384	871, 1384	Residual nitrate	[152, 161]
1029, ∼1095	1029, ∼1095	1029, ∼1095	1029, ∼1095	P-O stretching vibration mode v_3	[36, 156-158]
∼1443	1411-1450	1424-1483	1424-1469	B-type CO_3^{2-} vibration mode v_3	[113, 159, 160]
-	1562, 1582	-	-	A-type CO_3^{2-} vibration mode	[158]
1634, 3010, 3188, 3431	1654, 3424	1641, 3424	1634, 3431	Adsorbed water	[158, 161]
-	-	2359	-	CO_2 in air	[106]
-	2851	-	-	CH_2 stretching vibration mode	[113]
3571	-	3571	3571	OH$^-$ stretching mode	[20, 36, 148, 157]
-	2924, 2964	-	-	Unassigned	

3.1.3. Raman spectroscopy studies

Figure 29 shows the Raman spectra of three HA samples prepared by using two different methods. The Raman peak positions and their assignments are summarized in Table 10.
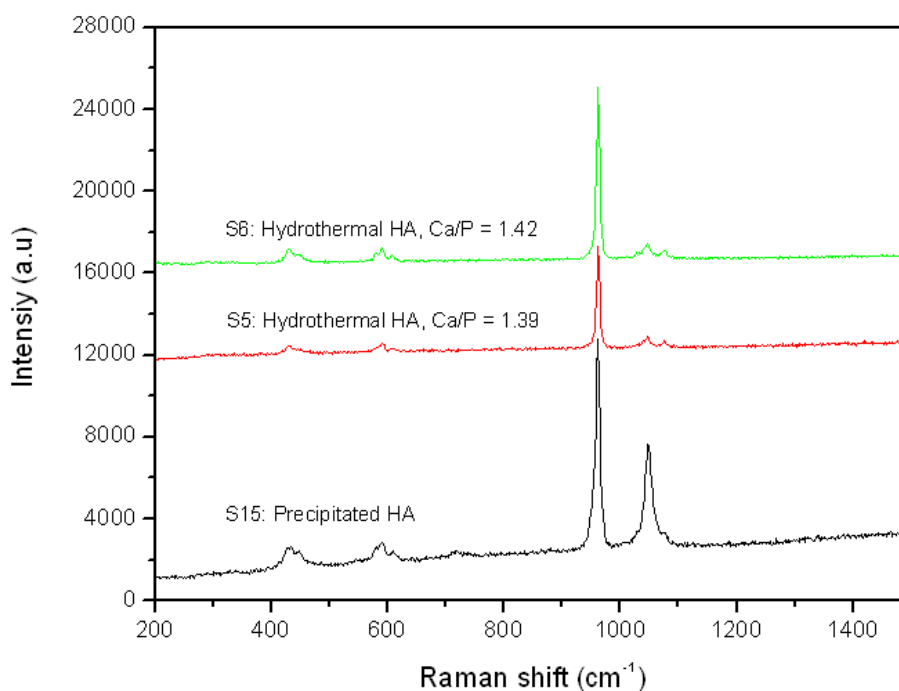
Figure 29: Raman spectra of three different HA samples: (S15) precipitated HA, (S5) hydrothermal HA, Ca/P = 1.39, (S6) hydrothermal HA, Ca/P = 1.42.

The characteristic Raman peak of HA was reported to be present in the region between 963 and 961 cm^{-1}, assigned to the v_1 PO$_4^{3-}$ mode [10, 121]. Similar peak at around 963 cm^{-1} is observed for all three HA samples S5, S6 and S15. In addition, three other PO$_4^{3-}$ modes are present in the region of 450-400 cm^{-1} (PO$_4^{3-}$ v_2), 1076-1028 cm^{-1} (PO$_4^{3-}$ v_3), and 610-579 cm^{-1} (PO$_4^{3-}$ v_4) [10, 121], which also appear in Figure 29 for all samples. The above observations tend to agree with the XRD and FTIR data suggesting that the above samples generally exhibit a HA structure. *Penel and co-workers* pointed out that the Raman peak at 1070 cm^{-1} was not able to be assigned to the PO$_4^{3-}$ v_3 mode solely, as the A-type and B-type CO$_3^{2-}$ mode v_1 was also present at a similar peak position at 1107 and 1070 cm^{-1}, respectively [121]. Considering the above, one can say that a small amount of CO$_3^{2-}$ inclusions are possibly present in all three cases, suggested by the

appearance of FTIR peaks at around 878 cm^{-1} and 1411-1450 cm^{-1} in Figure 26. Hence, the Raman peak at around 1076 cm^{-1} observed in all HA samples can be assigned to both PO$_4^{3-}$ v_3 mode [10, 121] and B-type CO$_3^{2-}$ v_1 mode [121], in the current Raman studies.

Smith and co-workers [163], reported two weak peaks at 763 and 694 cm^{-1} that were not possible to be assigned and were observed also in the case of the synthetic apatite S15. A weak Raman peak at around 716 cm^{-1} was also observed in the case of S15. However, similar peaks at around 690, 716, and 751 cm^{-1} were also present in the precipitated carbonate-containing apatite samples with the CO$_3^{2-}$ concentration ranging from 6.4 to 12.4 wt%, as well as the human enamel sample, observed by *Nishino and co-workers*, who actually suggested that the appearance of the above peaks in the laser-Raman spectra were clearly due to the CO$_3^{2-}$ mode v_4 vibrations [164]. In the current study, the Raman peak at around 716 cm^{-1} corresponding to CO$_3^{2-}$ ions was only observed in the case of S15, and therefore it could be recognized as a typical CO$_3^{2-}$ peak of the HA samples that were exclusively prepared by using a chemical precipitation method as it can be shown in Figure 29.
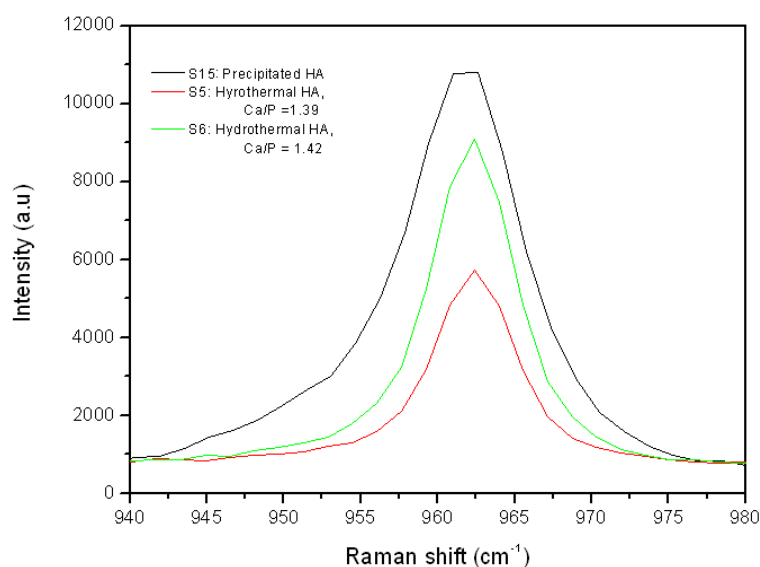
Figure 30: The Raman spectra details of three HA samples in the domain of the PO$_4^{3-}$ mode v_1.

De Mul and co-workers indicated that the Raman peak width in the v_1 PO$_4^{3-}$ mode at

963cm^{-1} is a function of the overall CO$_3^{2-}$concentration in the apatite samples [82]. Therefore, the amount of CO$_3^{2-}$ inclusions in the three HA samples can be evaluated, by comparing the peak width of the v_1 PO$_4^{3-}$ mode, as shown in Figure 30. It is clear, that in the case of S15 the bandwidth at 963 cm^{-1} is much larger compared to the bandwidth of the other two HA samples, indicating that most likely S15 exhibits a higher CO$_3^{2-}$ content compared to the other two hydrothermally synthesized HA samples (S5 and S6) [82]. In addition, *De Aza and co-workers* suggested that the crystallinity of the materials tested was directly dependent on the Raman peak intensities and the width (a sharper peak indicates higher degree of crystallinity) [165]. In this work, the Raman peak intensities seem to be higher in the case of S15 than in the case of S5 and S6 indicating therefore, that S15 should have higher degree of crystallinity. This however is not in good agreement with the XRD data that show clearly that S15 exhibit broader peaks of lower intensity compared to the other two HA samples. As reported by *Dorozhkin*, the structure of the apatite crystals is actually consisted of four different hierarchical levels and the XRD technique is only able to detect the second level, described as X-ray coherent scattering blocks with a size of 50-80 nm [166]. In this case, the lower intensity XRD peaks of S16 might reflect the higher degree of the overall apatite crystal imperfection induced by the higher CO$_3^{2-}$ concentration or even the smaller crystal size. Hence, the Raman observations in this work can be in alignment with the XRD results.

Table 10: Peak assignment of Raman spectra for (S15) precipitated HA, (S5) hydrothermal HA, Ca/P = 1.39, and (S6) hydrothermal HA, Ca/P = 1.42.

S15: Precipitated HA	S5: Hydrothermal HA, Ca/P = 1.39	S6: Hydrothermal HA, Ca/P = 1.42	Assignment	Reference
430, 446	428, ~446	431, ~450	PO$_4^{3-}$ mode v_2	[10, 121]
578, 594, 610	~579, 591, ~609	579, 592, 608	PO$_4^{3-}$ mode v_4	[10, 121]
961	963	963	PO$_4^{3-}$ mode v_1	[10, 121]
1048, 1076	1048, 1076	1028, 1047, 1076	PO$_4^{3-}$ mode v_3	[10, 121]
1076	1076	1076	B-site CO$_3^{2-}$ mode v_1	[121]
~716	-	-	CO$_3^{2-}$ mode v_4	[164]

3.1.4. ^{31}P MAS-NMR spectroscopy studies

Figure 31 shows the ^{31}P MAS-NMR spectra of four HA samples prepared by using three different methods. The ^{31}P chemical shifts and their peak width at half maximum (FWHM) are listed in Table 11.
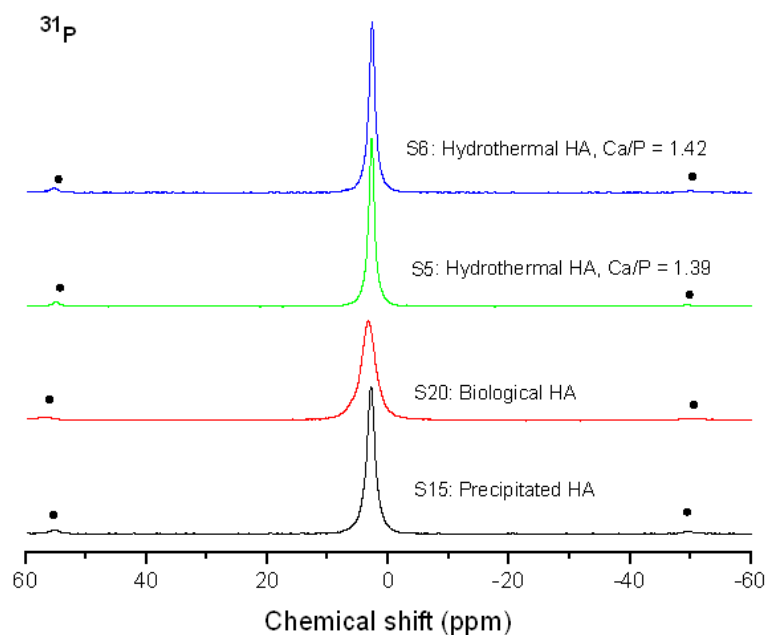

Figure 31: 31P MAS-NMR spectra of four different HA samples: (S15) precipitated HA, (S20) biological HA, (S5) hydrothermal HA, Ca/P = 1.39, (S6) hydrothermal HA, Ca/P = 1.42. The side bands are indicated by •

In the case of the chemical precipitated S15, the very intense peak at 2.9 ppm is due to phosphorus in an orthophosphate environment typical for HA as reported by *Miquel and co-workers* [167]. All samples exhibit a similar peak suggesting that phosphorus is present in a similar orthophosphate environment. Only small differences in terms of peak width and peak height can be noticed among these four HA samples and the FWHM of the above HA samples are listed in Table 11. As shown in Table 11, the hydrothermally derived S5 and S6 HA samples show the smallest FWHM, whereas the biological HA (S20) exhibits the largest FWHM and the chemical precipitated HA sample S15 exhibits an intermediate FWHM. As suggested by *Miquel and co-workers*, two reasons could cause the increase in the peak width of the ^{31}P MAS-NMR spectra of

the apatite samples: (1) a disordered P environment of apatite due to the calcium deficient apatite structure; (2) a low degree of crystallinity of the apatite materials [168]. In addition, *Jäger and co-workers* reported, that decreased crystallite size could also result in an increase in the peak width [169].

In this work, the smallest FWHM was observed for the hydrothermally derived HA samples (S5 and S6) and is possibly due to the larger crystallite size associated with the higher degree of crystallinity. In the contrary, the other two HA samples exhibit smaller crystallite size demonstrated by the XRD graphs and the larger FWHM in the ^{31}P MAS-NMR spectra of both biological HA (S20) and chemical precipitated HA (S15), associated with lower degree of crystallinity. The ^{31}P MAS-NMR peak broadening observed in the case of S15 and S20 is possibly caused by a disordered P environment, due to the calcium deficiency in the apatite structure, suggested by *Miquel and co-workers* [168]. *Miquel and co-workers* also reported that the presence of calcium deficiency in the apatite structure could be originated from the presence of HPO_4^{2-} groups, evidenced by a peak at 7 ppm in the ^{1}H MAS-NMR spectrum of a calcium deficient HA sample [168]. The FTIR results presented in paragraph *3.1.2* showed that most likely all HA samples might be calcium deficient as they all contain a small amount of HPO_4^{2-}, evidenced by the presence of an FTIR band at around 878 cm^{-1}. Furthermore, the presence of HPO_4^{2-} in the case of the biological S20 was also confirmed by *Sammons and co-workers*, who reported an HPO_4^{2-} FTIR peak at 870 cm^{-1} in a similar biological HA sample [156].

The local apatite structure, in other words differences in the apatite lattice would have an effect also on the chemical shift in the ^{31}P MAS-NMR spectra. In Table 11 one can observe, that the chemical shift of the hydrothermal Ca deficient apatites is lower compared to both chemical precipitated and biological apatites with the biological apatite having the highest chemical shift. *Miquel and co-workers* reported, that the stoichiometric HA has a chemical shift of 2.9 ppm [168], (in good agreement with the data presented in this work) whereas the deficient HA and the poorly crystallized hydroxyapatite have a chemical shift of 3.0 and 3.3 ppm, respectively. The chemical shift of the Ca deficient hydrothermal apatite samples reported here was 2.7 and 2.8 lower than the values reported in the literature for Ca deficient apatites [170] however, the biological apatite that is considered to be poorly crystallized as well as it contains a

higher amount of CO_3^{2-} and most likely is calcium deficient exhibited a chemical shift (3.3 ppm) considerably higher than the other HA samples. The latter is in good agreement with the values reported for poorly crystallized HA in the literature [168]. It is worth mentioning, that generally the CO_3^{2-} substitution and lower degree of crystallinity can push the chemical shift in ^{31}P MAS-NMR spectra to higher ppm values [170].

Table 11: ^{31}P MAS-NMR chemical shift and the peak width at half maximum (FWHM) of four HA samples: (S15) precipitated HA, (S20) biological HA, (S5) hydrothermal HA, Ca/P = 1.39, and (S6) hydrothermal HA, Ca/P = 1.42.

Sample	Description	Chemical shift (ppm)	FWHM (ppm)
S15	Precipitated HA	2.9	1.65
S20	Biological HA	3.3	2.89
S5	Hydrothermal HA, Ca/P = 1.39	2.8	1.11
S6	Hydrothermal HA, Ca/P = 1.42	2.7	1.11

3.2. Effect of Zinc substitution on the apatite structure

3.2.1. X-ray diffraction studies

Figure 32 shows the powder XRD patterns of a hydrothermal HA sample (S5) and a Zn substituted HA sample (S7). As described in paragraph *3.1.1*, the XRD peaks in the case of S5 are assigned to the single HA phase. By introducing 2.6 wt% of Zn, no major differences are observed in the XRD pattern of S7 indicating that the apatite crystal lattice has not been affected by the presence of 2.6 wt% of Zn. This is in good agreement with the published literature [87-89, 126]. *Miyaji and co-workers* reported that the HA structure can tolerate up to 15 mol% of Zn substitution [88].
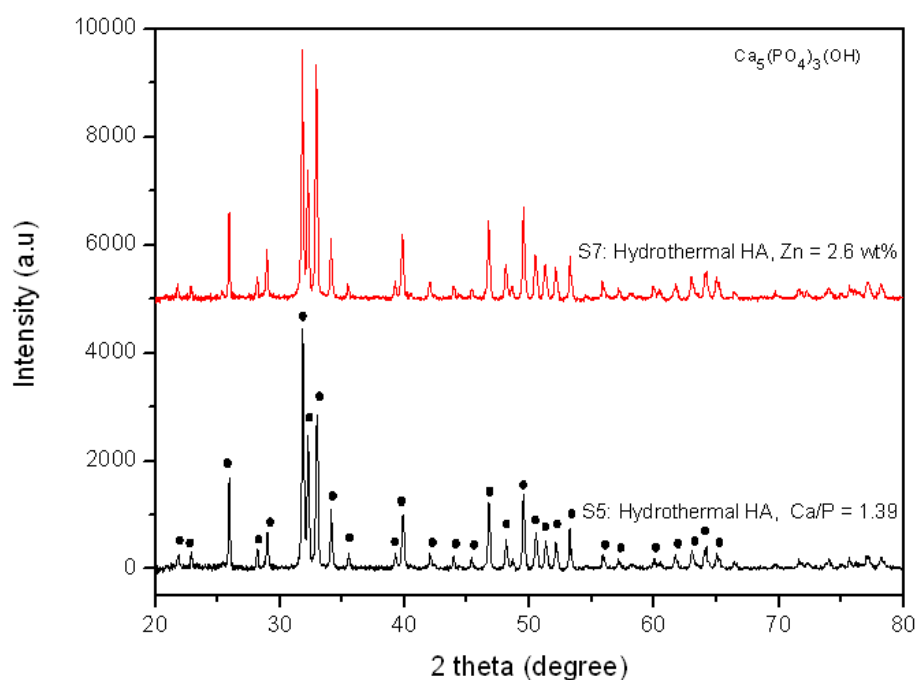
Figure 32: Powder XRD patterns of (S5) hydrothermal HA, Ca/P = 1.39 and (S7) hydrothermal HA, Zn = 2.6 wt%.

In addition, they also indicated that within the substituting limits of Zn in HA structure, the crystallite size and crystallinity of apatite was decreased with increasing Zn concentration [88]. Although little differences can be found in the XRD patterns of S5 and S7 (the intensity of the peak at $2\theta=32.89$ is increased in the case of Zn substituted

apatite), the crystal size seems to be very similar as shown in Table 12.

Table 12: Extrapolated Zn substitution, phase identification, and crystallite size of (S7) hydrothermal HA, Zn = 2.6 wt%, and (S5) hydrothermal HA, Ca/P = 1.39.

Sample	Extrapolated Zn substitution (wt%) in the solid phase	Phase identification	Crystallite size (nm)
S5	-	HA	42
S7	2.6	HA	43

Bigi and co-workers [87] reported that Zn can be also located on the apatite crystal surface or present in the amorphous phase. Considering that no obvious changes were observed in the XRD pattern of the Zn substituted sample, it is likely that the Zn substitution in the lattice is either very small or almost negligible. Another possibility is that Zn has not entered the HA lattice and is present only on the hydrated layer of the apatite surface or within the amorphous phase [87].

3.2.2. FTIR spectroscopy studies

Figure 33 shows the FTIR spectra of the S5 hydrothermal HA sample and the S7 Zn substituted HA sample. The absorption band positions and their assignments are summarized in Table 13. As discussed previously in paragraph *3.1.2*, the FTIR peaks present in the spectrum of S5 are generally assigned to HA, due to the presence of four PO_4^{3-} vibration modes at: 963 (PO_4^{3-} mode v_1), 470 (PO_4^{3-} mode v_2), 1029 and ~1095 (PO_4^{3-} mode v_3), and 601-561 cm^{-1} (PO_4^{3-} mode v_4) [36, 156-158], as well as the presence of OH$^-$ stretching and libration modes at 3571 and 634 cm^{-1}, respectively [20, 36, 148, 157]. A small fraction of CO_3^{2-} is also present indicated by the B-type CO_3^{2-} vibration modes v_2 and v_3 at 871 and 1424-1483 cm^{-1} [113, 159, 160].
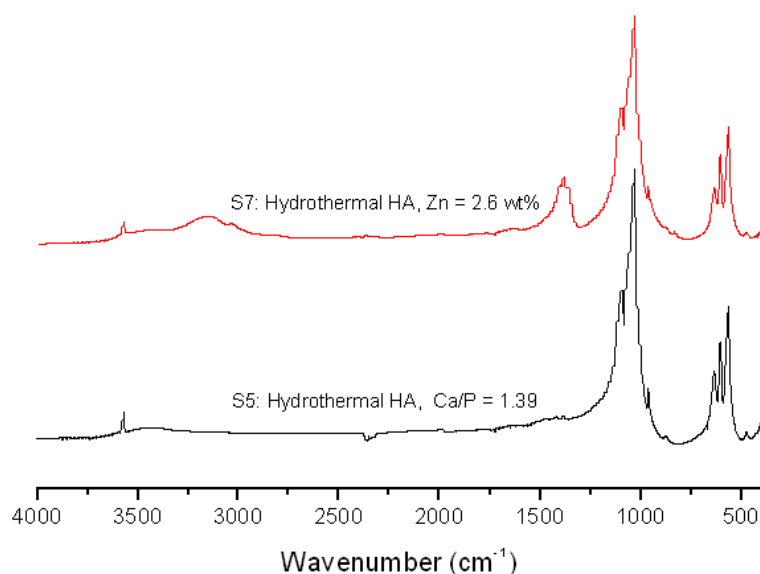
Figure 33: FTIR spectra of (S5) hydrothermal HA, Ca/P = 1.39 and (S7) hydrothermal HA, Zn = 2.6 wt%.

The addition of 2.6 wt% Zn into HA results in the appearance of a new broad peak in the region of 1517-1306 cm^{-1} and two additional water bands at around 3155 and 3037 cm^{-1}. A new very small almost negligible peak at 831 cm^{-1} is also present. No other significant change was observed. According to *Raynaud and co-workers,* the peaks at 820 and 1380 cm^{-1} can be assigned to residual nitrate groups [152]. Hence, the new band appeared at 831 cm^{-1} and the intensive band centred at 1384 cm^{-1} in the region of 1575-1279 cm^{-1} in the case of S7, can be attributed to the incorporation of more nitrates in the apatite structure during the hydrothermal process. It has been also reported, that the CO_3^{2-} mode v_3 is present in the region of 1570-1410 cm^{-1} [114], and therefore it might overlap with the band in the region of 1575-1279 cm^{-1}, which is already ascribed to the presence of residual nitrates [151, 152], as described above. In the case of S7, it is very likely that CO_3^{2-} is present especially when the CO_3^{2-} mode v_2 at 871 cm^{-1} is also present in the FTIR spectrum [114].

Table 13: Explanation of the FTIR spectra for (S5) hydrothermal HA, Ca/P = 1.39, and (S7) hydrothermal HA, Zn = 2.6 wt%.

S5: Hydrothermal HA, Ca/P = 1.39	S7: Hydrothermal HA, Zn = 2.6 wt%	Assignment	Reference
476	470	O-P-O bending mode v_2	[36, 156-158]
561-601	561-601	O-P-O bending mode v_4	[36, 156-158]
634	634	OH⁻ libration mode	[20, 36, 148, 157]
871	871	B-type CO_3^{2-} vibration mode v_2/ HPO_4^{2-}	[113, 159, 160]/ [152, 156, 162]
963	963	P-O stretching vibration mode v_1	[36, 156-158]
871, 1384	831, 871, 1384	Residual nitrate	[152, 161]
1029, ∼1095	1029, 1102	P-O stretching vibration mode v_3	[36, 156-158]
1424-1483	1517-1306	B-type CO_3^{2-} vibration mode v_3	[113, 159, 160]
1641, 3424	1634, 3037,3155	Adsorbed water	[158, 161]
2359	-	CO_2 in air	[106]
3571	3571	OH⁻ stretching mode	[20, 36, 148, 157]

It is also worth mentioning that both case of S5 and S7 are suspected to contain minor amount of HPO_4^{2-}, as similar FTIR peak at 875 cm⁻¹ has been assigned to HPO_4^{2-}, reported by *Raynaud and co-workers* [152, 162]. Furthermore, the two additional bands at 3155 and 3037 cm⁻¹ indicate that in the case of S7 water molecules are adsorbed on the apatite crystal surface [158, 161].

3.2.3. Raman spectroscopy studies

Figure 34 shows the FTIR spectra of HA sample (S5) and the Zn substituted HA sample (S6). The Raman peak positions and their assignments are summarized in Table 14. As observed in Figure 34, in the case of S5, four PO_4^{3-} vibration modes are present at 961 (v_1 PO_4^{3-} mode), 450-400 (v_2 PO_4^{3-} mode), 1076-1028 (v_3 PO_4^{3-} mode) and 610-579 cm⁻¹ (v_4 PO_4^{3-} mode) [10, 121], respectively. The 2.6 wt% of Zn substitution did not

result in significant changes in the case of S7, indicating that the apatite structure can tolerate the presence of 2.6 wt% Zn, and hence supporting the XRD observations reported above.
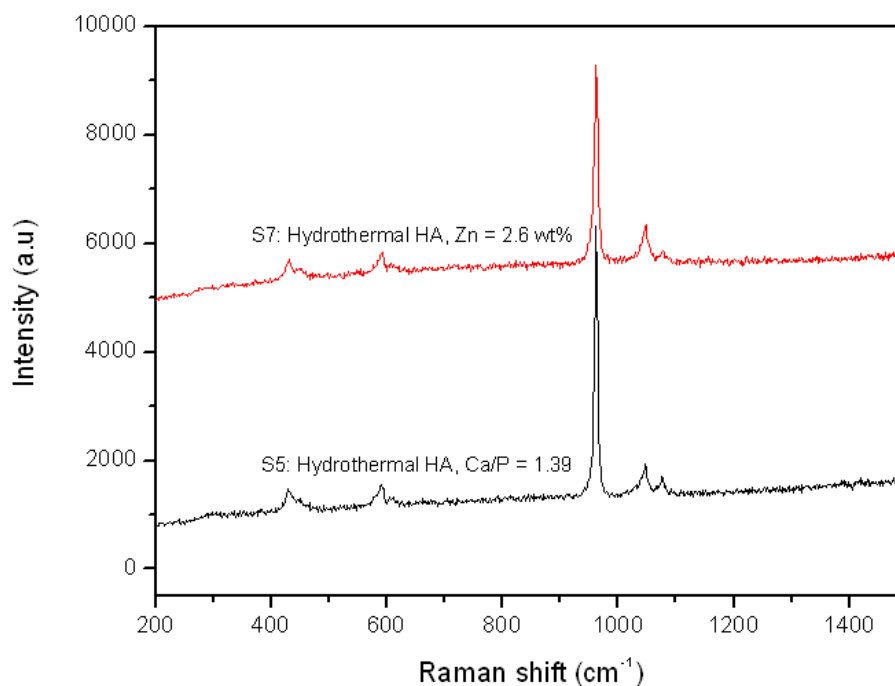
Figure 34: Raman spectra of (S5) hydrothermal HA, Ca/P = 1.39 and (S7) hydrothermal HA, Zn = 2.6 wt%.

In the case of S5 and S7 a small fraction of CO_3^{2-} might be present due to the appearance of a peak at 1076 cm^{-1} which although it has been already assigned to the PO_4^{3-} mode v_3 [10, 121] it can overlap with the peak assigned to B-type CO_3^{2-} v_1 vibration mode [121]. This is also supported by the FTIR spectra that exhibited two peaks at 1570-1410 and 871 cm^{-1} (Figure 33) corresponding to the CO_3^{2-} mode v_3 and v_2 [114] as described above in paragraph *3.2.2*. In order to compare the amount of the CO_3^{2-} content present in the case of S5 and S7, the details of the Raman peak at 963 cm^{-1}, corresponding to the PO_4^{3-} mode v_1[10, 121], is represented in Figure 35.

As observed in Figure 35, in the case of S7 there is a larger FWHM of the Raman peak in the PO_4^{3-} mode v_1 compared to the FWHM of the same peak in the case of S5 indicating that S7 contains a higher amount of CO_3^{2-} compared to S5 [82]. In addition, it is noticed that the Raman peak intensity is lower in the case of S7 than in the case of S5 indicating that S7 exhibits also a lower degree of crystallinity [165]. This is in good

agreement with Miyaji and co-workers who reported that the degree of crystallinity of apatite decreases with increasing the Zn content [88].
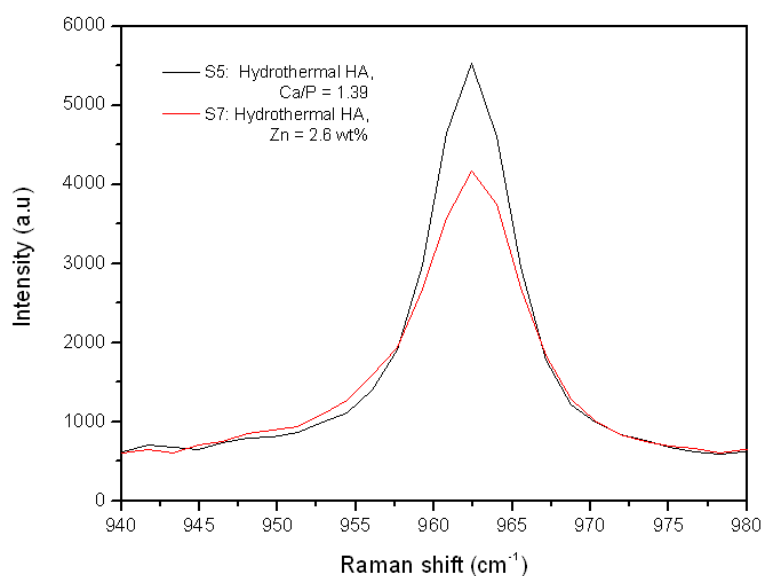
Figure 35: PO_4^{3-} mode v_1 in the Raman spectra of two HA samples: (S5) hydrothermal HA, Ca/P = 1.39 and (S7) hydrothermal HA, Zn = 2.6 wt%.

Table 14: Explanation of the Raman spectra for (S5) hydrothermal HA, Ca/P = 1.39 and (S7) hydrothermal HA, Zn = 2.6 wt%.

S5: Hydrothermal HA, Ca/P = 1.39	S7: Hydrothermal HA, Zn = 2.6 wt%	Assignment	Reference
428	430, ~448	PO_4^{3-} v_2 mode	[10, 121]
592	578, 592, ~608	PO_4^{3-} v_4 mode	[10, 121]
963	963	PO_4^{3-} v_1 mode	[10, 121]
1047, 1076	1047, 1076	PO_4^{3-} v_3 mode	[10, 121]
1076	1076	B-site CO_3^{2-} mode v_1	[121]

3.2.4. ^{31}P MAS-NMR spectroscopy studies

Figure 36 shows the ^{31}P MAS-NMR spectra of HA sample (S5) and the Zn substituted HA sample (S7). The ^{31}P chemical shift and the peak width at half maximum for each sample are listed in Table 15.
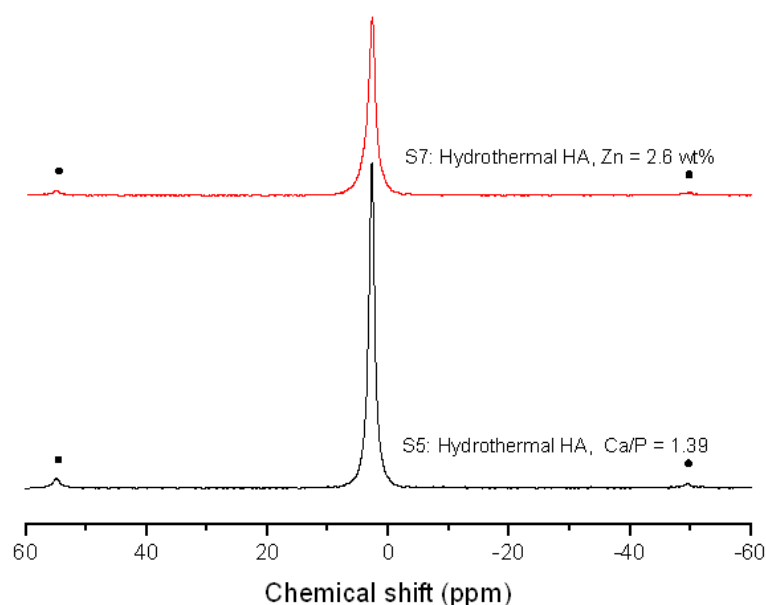
Figure 36: ^{31}P MAS-NMR spectra of (S5) hydrothermal HA, Ca/P = 1.39 and (S7) hydrothermal HA, Zn = 2.6 wt%. The side bands are indicated by •

From Figure 36 it is clear, that both samples have phosphorus in an orthophosphate environment as expected. Comparing the chemical shift of S7 with S5 it is worth noticing, that the main phosphorus peak for S7 appears at 2.6 ppm, only a few ppm lower than the peak for S5. *Fujii and co-workers* reported a similar observation when they looked at the Zn substitution in precipitated HA [126]. In this work, although we noticed a decrease in the chemical shift in the case of Zn substituted apatite, we did not notice a decrease in crystallinity as the FHWM is the same for both samples. On the other hand, it has been reported that the degree of crystallinity in Zn substituted apatites decreases with increasing the Zn content [88, 89]. In addition, the crystal size seems to decrease with Zn substitution [87-89]. In the present work however, we did not notice any evidence of decrease in the crystallinity of the Zn substituted apatite. As mentioned above, even the XRD pattern of the Zn substituted apatite is similar to the control HA

sample. This points to the conclusion, that Zn substitution is either very small or Zn substitution did not take place at all during the hydrothermal process and Zn is located on the surface of the apatite crystals. It has been reported, that Zn substitution by the hydrothermal process is more difficult than substitution by other chemical methods [89]. *Li and co-workers* reported that the measured amount of zinc in Zn substituted apatites was much smaller than the amount of zinc used during the hydrothermal process [89].

Table 15: ^{31}P MAS-NMR chemical shift and peak width at half maximum (FWHM) of two hydrothermal HA samples: (S5) Ca/P = 1.39, and (S7) Zn = 2.6 wt%.

Sample	Description	Chemical shift (ppm)	FWHM (ppm)
S5	Hydrothermal HA, Ca/P = 1.39	2.8	1.11
S7	Hydrothermal HA, Zn = 2.6 wt%	2.6	1.11

3.3. Effect of Magnesium substitutions on the apatite structure

3.3.1. X-ray diffraction studies

Figure 37 shows the powder XRD patterns of five HA samples with different Mg substitutions. Both S5 and S1 exhibit the characteristic XRD pattern of HA. This suggests that the presence of 0.7 wt% Mg in the case of S1 does not disturb the apatite structure and substitutes Ca successfully. This is in good agreement with reported Rietveld XRD analysis, that defines the substitution limit of Mg for Ca(II) in the apatite structure around 10 atom% [129, 171].
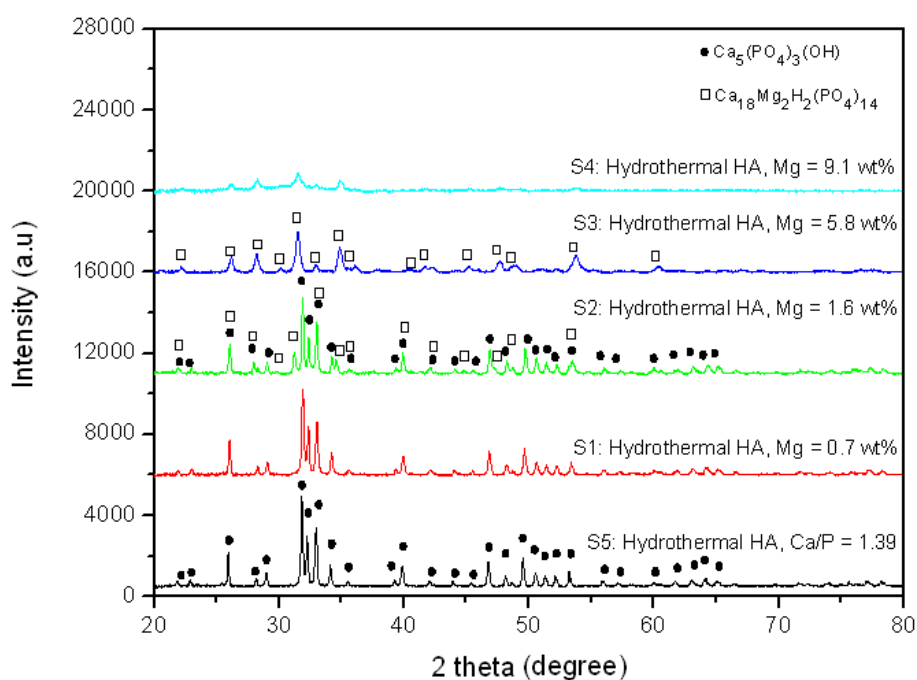
Figure 37: Powder XRD patterns of hydrothermal HA samples with different Mg substitutions: (S5) Ca/P = 1.39, (S1) Mg = 0.7wt%, (S2) Mg = 1.6wt%, (S3) Mg = 5.8wt%, (S4) Mg = 9.1wt%.

In the case of S2 as Mg substitution increased to 1.6 wt%, two phases were observed; HA and Mg-whitlockite ($Ca_{18}Mg_2H_2(PO_4)_{14}$). The phase composition of S2 was calculated according to Equation 12 and is presented in Table 16. The formation of

Mg-whitlockite in the case of S2 indicates that the degree of Mg substitution in the apatite lattice is very small and that increasing the Mg content results in inhibiting the CaMg-HA formation and favouring the formation of Mg-whitlockite. Unfortunately, there is no available literature on Mg substituted apatites formed by a hydrothermal method but it seems that chemical precipitation methods are a better approach to form Mg substituted apatites. For example, *Yasukawa and co-workers* claimed that CaMg-HA particles could be received by a chemical precipitation method up to a limit where Mg/(Mg+Ca) $\leq$ 0.31 [93]. They also claimed that cations larger than Ca could occupy the cation (II) sites in the apatite lattice, whereas the smaller cations like Mg preferred the cation (I) sites [93, 172]. The main reason for this was that the nearest distance between cation (I) sites was smaller than that between cation (II) sites [93, 172]. On the other hand, *Bigi and co-workers* conducted Rietveld structure refinement in Mg substituted HA produced by a chemical precipitation method and reported that the degree of Mg substitution for Ca in the apatite structure could be at a max 10 atom% and that Mg substituted Ca preferentially in the Ca(II) sites of the apatite lattice [129]. They also reported, that the broadening of the diffraction peaks increased with increasing the total Mg content in the solid phase which was always significantly higher than the amount incorporated in the HA structure and the excess of Mg was located either in the amorphous phase or on the surface of the apatite crystal [129].

Table 16: Measured Mg substitution, phase compositions, and crystallite size of 5 hydrothermal HA samples with different Mg substitutions: (S5) Ca/P = 1.39, (S1) Mg = 0.7wt%, (S2) Mg = 1.6wt%, (S3) Mg = 5.8wt%, (S4) Mg = 9.1wt%.

Sample	Measured Mg substitution (wt%) in the solid phase	Phase composition	Crystallite size (nm)
S5	-	HA	42
S1	0.7	HA	33
S2	1.6	81 wt% HA	43
		19 wt% Mg-whitlockite	37
S3	5.8	Mg-whitlockite	18
S4	9.1	Mg-whitlockite	16

Increasing further the Mg substitution to 5.8 wt% and 9.1 wt% (S3 and S4,

respectively), it results in the formation of a single Mg-Whitlockite phase. The intensity of the peaks decreases and the peaks appear broader. This can be due to the decrease of the crystal size with increasing Mg substitution as shown in Table 16. This is in good agreement with *Bigi and co-workers* who also found a decrease in the degree of crystallinity and crystallite size in the Mg substituted apatites [92]. It is worth noticing, that in the case of S2 the crystal size of the HA phase is similar to the crystal size observed in the case of S5. It is possible, that in the case of S2, Mg would preferably form Mg-Whitlockite and would not substitute Ca in the apatite phase and therefore the crystal size of the HA phase would remain similar to the pure HA phase in S5.

3.3.2. FTIR spectroscopy studies

Figure 38 shows the FTIR spectra of five HA samples with different Mg substitutions. The absorption band positions and their assignments are summarized in Table 17. As described in paragraph *3.1.2*, S5 exhibits only one phase (HA), which contains a small amount of CO_3^{2-} most likely B-type CO_3^{2-}.
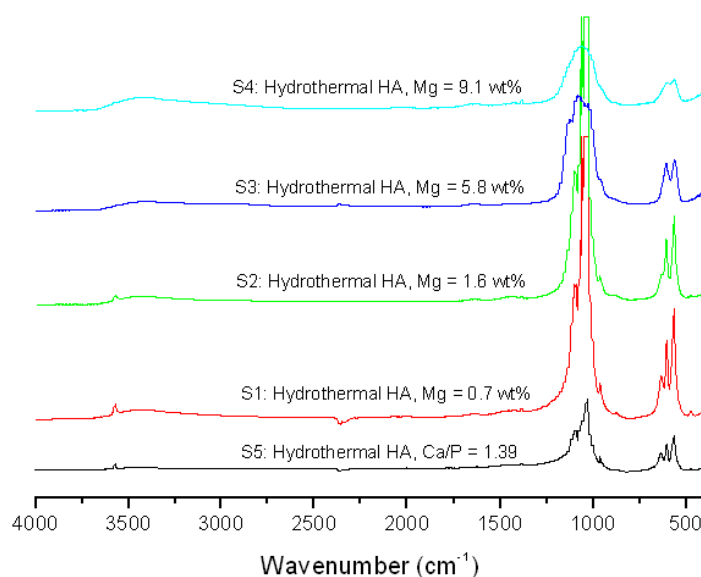
Figure 38: FTIR spectra of five HA hydrothermal samples with different Mg substitutions: (S5) Ca/P = 1.39, (S1) Mg = 0.7wt%, (S2) Mg = 1.6wt%, (S3) Mg = 5.8wt%, (S4) Mg = 9.1wt%.

Increasing the Mg substitution to 0.7 wt% (sample S1), all the FTIR absorption bands are present at similar positions as the absorption bands in the case of S5. This indicates that 0.7 wt% Mg substitution did not induce any significant change in the apatite structure of S1. Increasing the Mg substitution to 1.6 wt% (sample S2), the FTIR bands assigned to the four PO_4^{3-} modes appear at similar wavenumbers as these in S5 and S1. However, a reduction in the resolution at around 634 cm^{-1} assigned to OH$^-$ libration mode [20, 36, 148, 157] is observed in the case of S2. Such observations may reflect the formation of Mg-whitlockite in addition to the main phase of HA, as identified by XRD in paragraph *3.3.1*.

Increasing further the Mg substitution to 5.8 wt% (sample S3), the OH$^-$ libration and stretching bands at around 634 and 3571 cm^{-1} [20, 36, 148, 157], respectively, disappear as observed in Figure 43. In addition, the FTIR peaks at around 1029 and 1059 cm^{-1} assigned to PO_4^{3-} mode v_3 vibrations [36, 156-158], are gradually merged into a broad peak centred at around 1062 cm^{-1}. These changes imply, that the phase transformation from Mg substituted apatite to Mg substituted phosphate is completed when Mg content reaches 5.8 wt%. As Mg substitution reaches 9.1 wt% (sample S4), the FTIR spectrum of S4 shows a similar pattern to that of S3 but exhibits poorer resolution.

It is generally observed, that the peak broadening is more significant in the case of higher Mg substitution samples, which suggests that the apatite structure is somehow distorted by increasing the Mg substitution [106]. In addition, at higher Mg substitutions, ranging from 5.8 to 9.1, Mg favours the formation of Mg-whitlockite, as observed in the case of S3 and S4, rather than Mg substituted HA formed in both S1 and S2.

Table 17: Peak assignment of FTIR spectra for (S5) hydrothermal HA, Ca/P = 1.39, (S1) hydrothermal HA, Mg = 0.7wt%, (S2) hydrothermal HA, Mg = 1.6wt%, (S3) hydrothermal HA, Mg = 5.8wt%, (S4) hydrothermal HA, Mg = 9.1wt%.

S5: Hydrothermal HA, Ca/P = 1.39	S1: Hydrothermal HA, Mg = 0.7wt%	S2: Hydrothermal HA, Mg = 1.6wt%	S3: Hydrothermal HA, Mg = 5.8wt%	S4: Hydrothermal HA, Mg = 9.1wt%	Assignment	Reference
476	476	476	-	-	O-P-O bending mode v_2	[36, 156-158]
561-601	561-601	561-608	561-608	561-608	O-P-O bending mode v_4	[36, 156-158]
634	634	∼634	-	-	OH⁻ libration mode	[20, 36, 148, 157]
871	∼875	874	877	876	B-site CO_3 vibration mode v_2/ HPO_4^{2-}	[113, 159, 160]/ [152, 156, 162]
963	963	963	-	-	P-O stretching vibration mode v_1	[36, 156-158]
871, 1384	871, 1384	871, 1384	∼898, 1384	871, 1384	Residual nitrate	[152, 161]
1029, ∼1095	∼1035, ∼1102	∼1035, ∼1102	∼1029, ∼1128	1062	P-O stretching vibration mode v_3	[36, 156-158]
1424-1483					B-site CO_3 vibration mode v_3	[113, 159, 160]
1641, 3424	1634, 3424	1634, 3418	1634, ∼3404	1634, 3418	Adsorbed water	[158, 161]
-	-	-	2371	-	CO_2 in air	[106]
3571	3571	3571	-	-	OH⁻ stretching mode	[20, 36, 148, 157]

3.3.3. Raman spectroscopy studies

Figure 39 shows the Raman spectra of five HA samples with different Mg substitutions. The Raman peak positions and their assignments are summarized in Table 18.
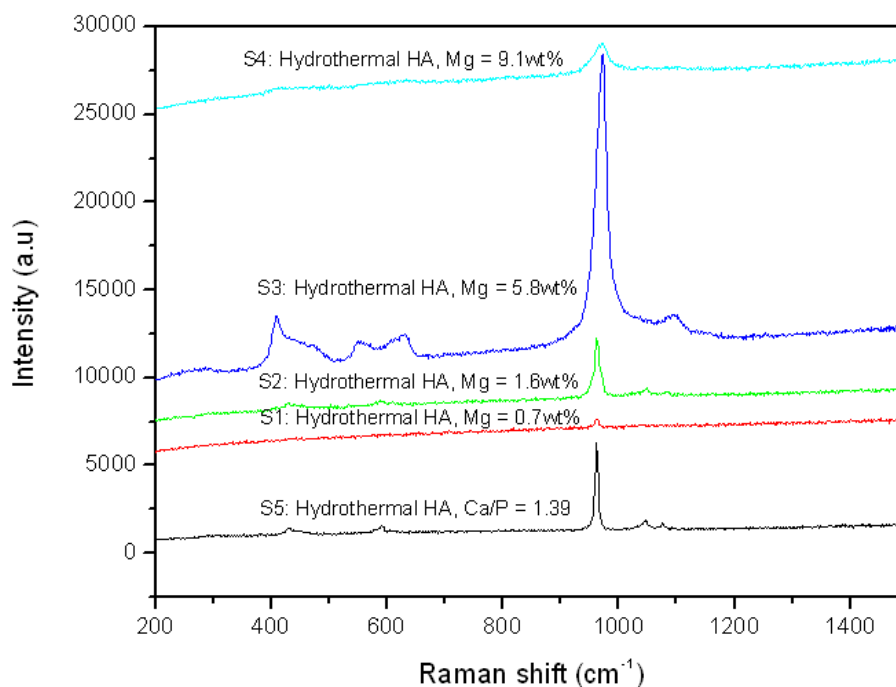
Figure 39: Raman spectra of five hydrothermal HA samples with different Mg substitutions: (S5) Ca/P = 1.39, (S1) Mg = 0.7 wt%, (S2) Mg = 1.6 wt %, (S3) Mg = 5.8 wt%, (S4) Mg = 9.1 wt%.

An intense Raman peak at around 963 cm^{-1} assigned to PO_4^{3-} mode v_1, known as the characteristic peak of HA [10, 121] is observed in the spectra of S5, S1 and S2 with Mg substitution ranging from 0 to 1.6 wt%. This observation is also supported by XRD and FTIR spectra that showed the presence of a similar apatite phase present in S5, S1 and S2. It should be noted, that the intensity of the HA characteristic Raman peak in the case of S1 is very low and the resolution of the peak quite poor. The appearance of a very low Raman peak intensity in the case of S1 may imply that the degree of crystallisation in this sample is much lower compared to S2 and S5. In addition, the lower resolution of the Raman spectrum in the case of S1 may be caused by the high signal to noise ratio. Better resolved Raman spectra are observed in the case of higher Mg substituted

samples, ranging from 1.6 to 9.1 wt%. Such change reflects the presence of a new crystalline phase, Mg-whitlockite formed in the case of S2, S3 and S4. As indicated also by the XRD results in paragraph *3.3.1*, HA and Mg-whitlockite are both present in the case of S2 and the peak at 963 cm^{-1} assigned to HA appears broader compared to S1 and S5. On the other hand, in the case of S3 and S4, where only Mg-whitlockite is present as evidenced by the XRD graphs, the intense peak assigned to HA at around 963 cm^{-1} now shifts to the higher energy band at 973 cm^{-1}. This shift clearly reflects the phase transformation from Mg-HA to Mg-whitlockite, which is favoured at higher Mg substitutions.

A general Raman peak broadening is observed in Figure 39, and it is particularly obvious in the samples with higher Mg substitutions (e.g., S3 and S4), which exhibit the typical Raman peaks for Mg-whitlockite. A similar Raman peak broadening with increasing Mg concentration was also reported by *Sprio and co-workers*, who suggested that this was an indication for a less ordered structure material [173]. Other reasons for the Raman peak broadening can be the segregation of Mg outside the HA lattice [173] or the presence of CO_3^{2-}, as reported by *De Mul and co-workers* who found that the Raman peak width in the PO_4^{3-} mode v_1 was increased with increased CO_3^{2-} concentration [82].

Table 18: Peak assignment of Raman spectra for (S5) hydrothermal HA, Ca/P = 1.39, (S1) hydrothermal HA, Mg = 0.7wt%, (S2) hydrothermal HA, Mg = 1.6wt%, (S3) hydrothermal HA, Mg = 5.8wt%, (S4) hydrothermal HA, Mg = 9.1wt%.

S5: Hydrothermal HA, Ca/P = 1.39	S1: Hydrothermal HA, Mg = 0.7wt%	S2: Hydrothermal HA, Mg = 1.6wt%	S3: Hydrothermal HA, Mg = 5.8wt%	S4: Hydrothermal HA, Mg = 9.1wt%	Assignment	Reference
430, 446	-	427	408, ∼474	∼409	PO_4^{3-} v_2 mode	[10, 121]
578, 594, 610	-	590	552, 630	∼633	PO_4^{3-} v_4 mode	[10, 121]
961	963	963	973	973	PO_4^{3-} v_1 mode	[10, 121]
1048, 1076	-	1046, 1085	1096	-	PO_4^{3-} v_3 mode	[10, 121]
1076	-	-	-	-	B-site CO_3^{2-} mode v_1	[121]

3.3.4. ^{31}P MAS-NMR spectroscopy studies

Figure 40 shows the ^{31}P MAS-NMR spectra of five HA samples with different Mg substitutions. The ^{31}P chemical shifts and their peak width at half maximum are listed in the Table 19.
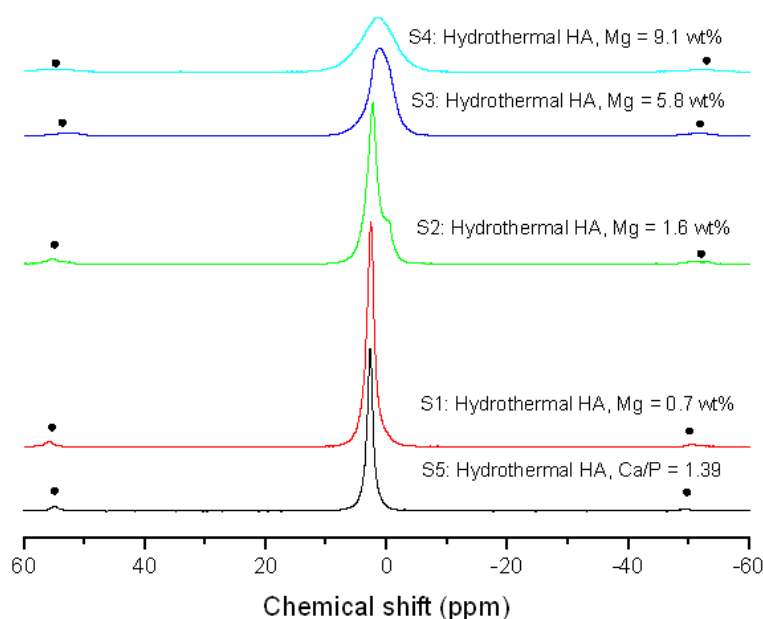
Figure 40: ^{31}P MAS-NMR spectra of five hydrothermal HA samples with different Mg substitutions: (S5) Ca/P = 1.39, (S1) Mg = 0.7wt%, (S2) Mg = 1.6wt%, (S3) Mg = 5.8wt%, (S4) Mg = 9.1wt%. The side bands are indicated by •

A single sharp peak at 2.8 ppm assigned to phosphorus in a Q^0 environment and attributed to the presence of well crystallised HA [174] is observed in the case of S5. Increasing Mg substitution to 0.7 wt%, the peak is slightly shifted from 2.8 ppm in the case of S5 to 2.6 ppm in the case of S1. This indicates that both S5 and S1, exhibit a similar phosphorus environment. Increasing further the Mg substitution to 1.6 wt% (sample S2), two peaks appear at 2.4 ppm and -0.3 ppm assigned to a Q^0 environment in apatite [174, 175] and Mg-whitlockite, respectively. *Aramendía and co-workers* on the other hand, assigned the peak at -0.3 ppm to farringtonite (crystalline $Mg_3 (PO_4)_2$) [176].

From the above it is clear, that the sample S2 is a biphasic sample containing a HA

phase and Mg-Whitlockite phase as was also confirmed by XRD. By increasing the Mg substitution to higher levels, an increase in the peak broadening is observed for S3 and S4.

**Table 19:** ^{31}P MAS-NMR chemical shift and peak width at half maximum (FWHM) of five hydrothermal HA samples with different Mg substitutions: (S5) Ca/P = 1.39, (S1) Mg = 0.7wt%, (S2) Mg = 1.6wt%, (S3) Mg = 5.8wt%, (S4) Mg = 9.1wt%.

Sample	Description	Chemical shift (ppm)	FWHM (ppm)
S5	Hydrothermal HA, Ca/P = 1.39	2.8	1.11
S1	Hydrothermal HA, Mg = 0.7wt%	2.6	1.42
S2	Hydrothermal HA, Mg = 1.6wt%	2.4	1.88
		-0.3	-
S3	Hydrothermal HA, Mg = 5.8wt%	1.2	3.99
S4	Hydrothermal HA, Mg = 9.1wt%	1.6	6.40

Aramendía and co-workers reported MAS-NMR data on Mg orthophosphate systems and ascribed the peak at 1.1 ppm in the ^{31}P MAS-NMR spectra of Mg-P systems to phosphorus in un-calcined $Mg_3(PO_4)_2 \cdot 22H_2O$ [176]. *Miquel and co-workers* indicated that the appearance of ^{31}P NMR peak at 1.2 ppm represented one of the three phosphate species observed in β-TCP ($Ca_3(PO_4)_2$) [168]. Furthermore *Wu and co-workers* [177] reported that a peak at around 1.4 ppm was assigned to HPO_4^{2-} in brushite ($CaHPO_4 \cdot 2H_2O$). The FTIR band at around 875 cm^{-1} observed in all the FTIR spectra (paragraph 3.3.2) however, was thought to be due to the presence of HPO_4^{2-} groups and in support of the above *Legeros and co-workers* reported that HPO_4^{2-} was incorporated into the HA structure with increasing Mg concentration in the apatite lattice [83] Therefore, it can be concluded that a certain amount of HPO_4^{2-} is expected to be present in all samples with Mg substitution ranging from 0 to 9.1 wt%.

Finally, Figure 40 shows clearly that increasing the Mg substitution from 0 to 9.1 wt%, the peak intensity decreases consistently and the peak width increases. This can be caused due to an increase in the structure disorder which is likely originated from: (1) the incorporation of increased HPO_4^{2-} due to the increase in Mg concentration [83]; (2)

the increase in the excess Mg content located outside the HA lattice [173]; and (3) the incorporation of increased CO_3^{2-} inclusions [168].

3.4. Effect of Strontium substitutions on the apatite structure

3.4.1. X-ray diffraction studies

Figure 41 shows the powder XRD patterns of five HA samples with increased Sr substitution, ranging from 0 to 100 mol%. As mentioned earlier in paragraph *3.1.1*, all XRD peaks in the case of S16 correspond to HA. As Sr substitution increases from 0 to 100 mol%, two significant changes can be observed: (1) the XRD peaks shift towards to lower values of 2 theta and (2) the intensity of the XRD patterns is consistently increased. Both observations are expected as the smaller Ca ion is progressively substituted by the larger Sr ion in the apatite lattice [95]. Rietveld refinement was employed in order to confirm the above observations in the case of S16 (25 mol% Sr substitution) which is shown in Figure 42.

The Ca-Sr-HA sample contains 25 mol% Sr substitution and exhibits a hexagonal structure (space group of P6$_3$/m) and lattice parameters of $a = b$ =9.529 Å, and c =6.983 Å. *Posner and co-workers* reported that the lattice parameters of HA are $a = b = 9.432$ Å, $c = 6.881$ Å [40]. Comparing the lattice parameters of S16 and the reported HA [40], the lattice parameters measured for S16 are larger than the reported parameters for HA indicating that incorporation of Sr into HA leads to the expansion of the original apatite structure. This is in good agreement with the literature [20, 95].
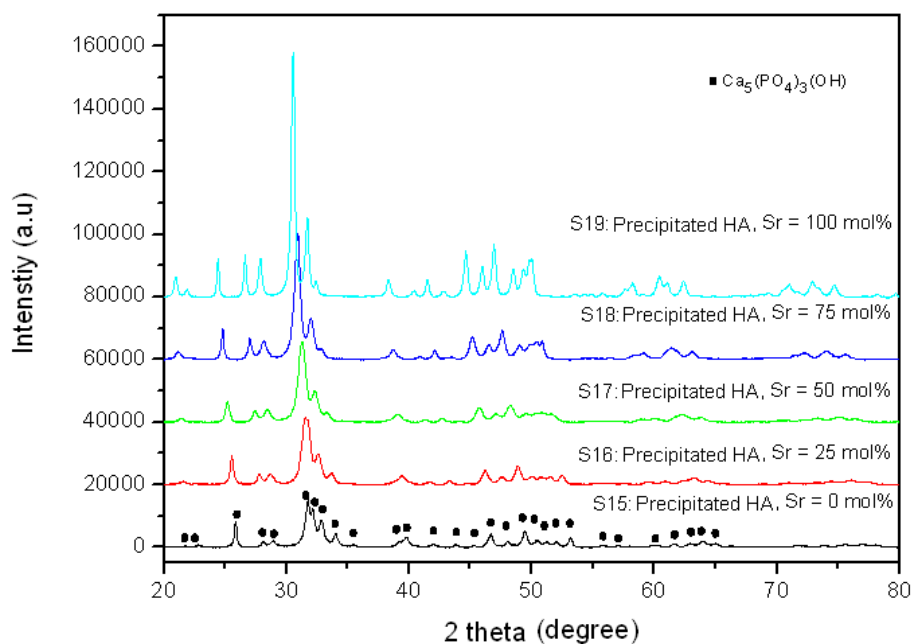
Figure 41: Powder XRD patterns of five precipitated HA samples with different Sr substitutions: (S15) Sr = 0 mol%, (S16) Sr = 25 mol%, (S17) Sr = 50 mol%, (S18) Sr = 75 mol%, (S19) Sr = 100 mol%.
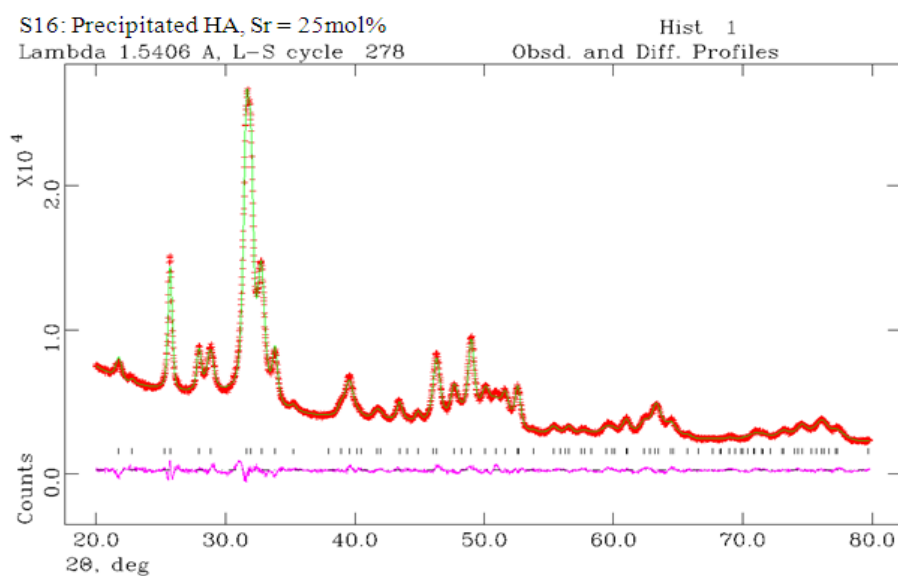
Figure 42: Rietveld refinement of (S16) precipitated HA, Sr = 25 mol%.

The XRD patterns of S15 and S19 in Figure 41 represent patterns of Sr free apatite and Sr substituted apatite, respectively. The XRD patterns in both cases exhibit well-defined and sharp peaks, indicating that both S15 and S19 are well-crystalline

materials. In order to study the effect of Sr substitution on the apatite crystallite size, the crystallite size of the HA samples with Sr substitution, ranging from 0 to 100 mol%, is calculated and summarized in Table 20. Peak broadening is observed in the case of partially substituted samples ranging from 25 to 75 mol% referred as Ca-Sr-HA samples (S16-S18). The peak broadening noticed in these three Ca-Sr-HA samples is due possibly to the smaller crystallite size. Similar observations were also reported by *Bigi and co-workers* [20].

Table 20: Expected Sr substitution, phase identification and crystallite size of five precipitated HA samples with different Sr substitutions.

Sample	Expected Sr substitution (mol%) in the solid phase	Phase identification	Crystallite size (nm)
S15	0	HA	16
S16	25	Ca-Sr-HA	11
S17	50	Ca-Sr-HA	10
S18	75	Ca-Sr-HA	11
S19	100	Sr-apatite	22

The relationship between the crystallite size of the apatite samples and the degree of Sr substitution from 0 to 100 mol% is shown in Figure 43.

Figure in graph: $y = 0.0039x^2 - 0.3406x + 16.457$, $R^2 = 0.9507$
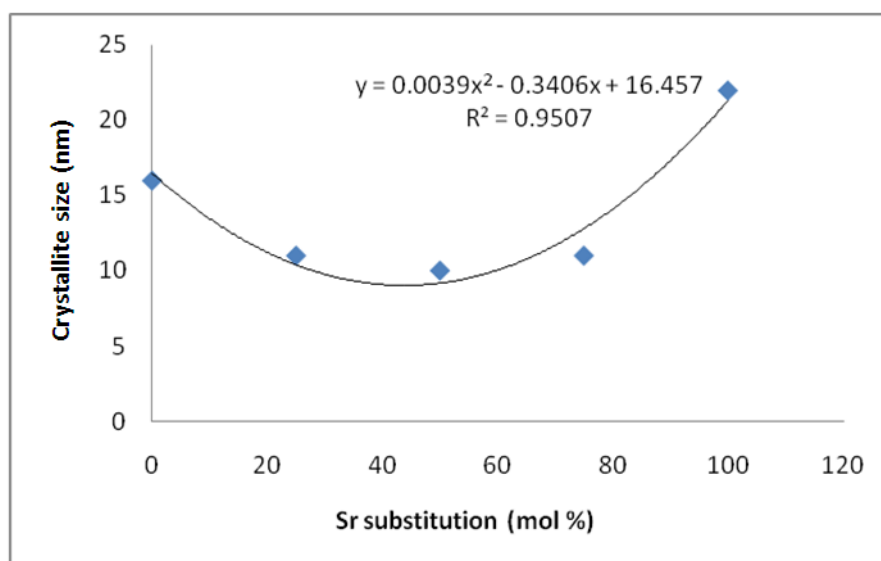
Figure 43: Changes of crystallite size with Sr substitution from 0 to 100 mol%.

As shown in Figure 43, the crystallite size of apatite is initially decreased with increasing Sr substitution from 0 to 50 mol%, and then begins to increase as Sr substitution becomes beyond 50 mol%. A similar observation was reported by *Li and co-workers*, who found that the crystallite size of a mixed cation Ca-Sr-HA decreased as Sr substitution increased from 0 to 15 % [130]. *O'Donnell and co-workers* reported, that the smallest crystallite size in a Ca-Sr-HA sample was obtained when Sr substitution reached 50% [95]. This is in good agreement with the present work as S17 contains 50 mol% Sr and exhibits the smallest apatite crystal size. Small crystal size normally suggests more disordered apatite structure [95]. *Bigi and co-workers* reported that TEM studies confirmed that the morphology of the apatite crystals exhibited perturbed shapes and less-defined edges when Sr concentration reached 50 mol% [20]. In addition, *Bigi and co-workers* also reported that both HA and fully Sr substituted apatite exhibited well defined apatite morphologies, with the latter case comprising of the largest crystallites [20]. These observations are in good agreement with the present XRD studies confirming that both apatite samples S15 and S19 are well-crystalline materials, and the largest crystallite size is indeed obtained in the case of S19 as shown in Table 20.

3.4.2. FTIR spectroscopy studies

Figure 44 shows the FTIR spectra of five HA samples with increased Sr substitution from 0 to 100 mol%. The absorption band positions and their assignments are summarized in Table 21.
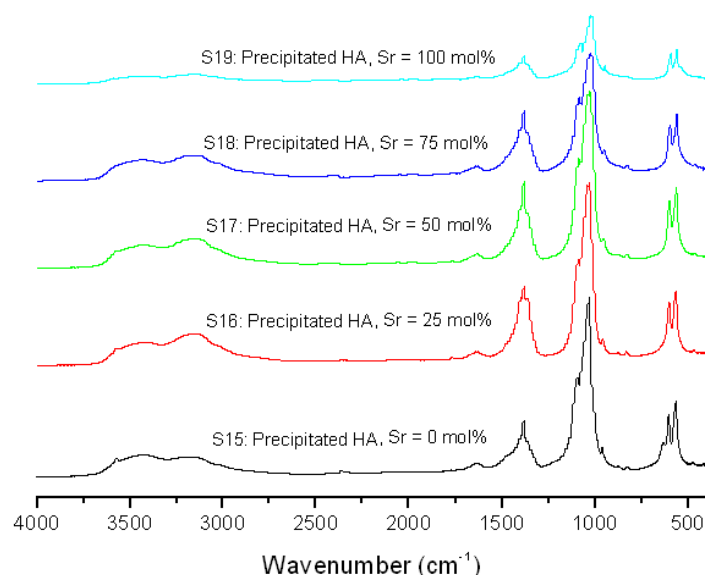
Figure 44: FTIR spectra of five precipitated HA samples with different Sr substitutions: (S15) Sr = 0 mol%, (S16) Sr = 25 mol%, (S17) Sr = 50 mol%, (S18) Sr = 75 mol%, (S19) Sr = 100 mol%.

The characteristic HA FTIR peaks appear in the FTIR spectra of all five apatite samples at 963 cm^{-1} (PO_4^{3-} v_1), 470 cm^{-1} (PO_4^{3-} v_2), 1029 and 1095 cm^{-1} (PO_4^{3-} v_3), and 561-601 cm^{-1} (PO_4^{3-} v_4) [36, 156-158] as well as the OH$^-$ libration and stretching mode at 634 and 3571 cm^{-1} [20, 36, 148, 157] as shown in Figure 44. Increasing the Sr substitution in the apatite structure, significant changes are observed in the peaks associated with PO_4^{3-} and OH$^-$ groups. As shown in Figure 45 (a) and (b), the v_1 P-O stretching mode is downshifted from 963 to 943 cm^{-1}, and the v_4 P-O stretching mode is downshifted from 561-601 to 555-588 cm^{-1} with increasing Sr substitution from 0 to 100 mol%. Similar observations were also made by other authors in the literature [20, 132, 178].
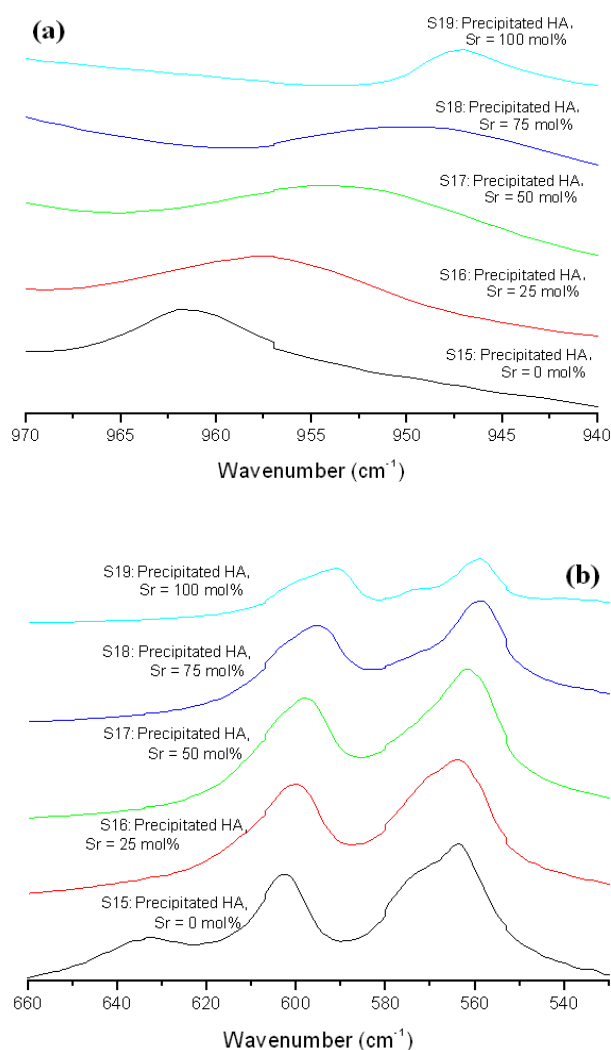
Figure 45: (a) The details of the v_1 P-O stretching mode for HA with Sr substitution in the range of 0 to 100 mol%; (b) The details of v_4 P-O stretching mode HA with Sr substitution in the range of 0 to 100 mol%.

Fowler reported FTIR studies in a series of apatite samples with different cationic substitution (Ca, Sr and Ba) [178]. They observed linear downshifts in the internal PO_4^{3-} modes in the apatite samples associated with decreased cationic radii [178]. They also reported that the observed shift in the PO_4^{3-} modes were mainly due to the decreased anion-anion repulsion accompanied by increased anion-anion separation [178]. Similarly, the shift of PO_4^{3-} v_1 mode and v_4 mode to lower wave numbers observed in the present apatite samples with increasing Sr substitution, reflects the increase in the cation size in the apatite lattice due to the substitution of Sr for Ca.

It should be noticed, that with increasing the Sr substitution in the apatite lattice, a new peak appears at around 1772 cm^{-1} in all Sr containing apatite samples. Considering the absence of such band in the case of the Sr free sample S15, the appearance of the band at around 1772 cm^{-1} in all other samples is likely due to the incorporation of Sr into the apatite lattice using as a chemical reactant $Sr(NO_3)_2$. Therefore, the band at around 1772 cm^{-1} in the FTIR spectra could be possibly associated with the presence of a small fraction of local impurities.

In the spectra of the above precipitated apatite samples the region of 1540-1300 cm^{-1} is probably associated with the presence of CO_3^{2-} ions. As reported in the literature [113, 114, 158, 160], the CO_3^{2-} bands are expected to appear in the region of 1580-1400 cm^{-1}. On the other hand, the central band position at around 1384 cm^{-1} can be assigned to residual nitrate groups [152, 161]. More importantly, a small shoulder observed in the case of S15 at around 1443 cm^{-1} can be associated with the presence of B-type CO_3^{2-} groups [113, 159, 160]. Although such an absorption band is not present in the Sr containing apatite samples (S16-S19), the possibility of the presence of CO_3^{2-} ions in all the chemical precipitated apatite samples cannot be excluded [114, 179, 180], and more details are provided in paragraph *3.4.3*.

Table 21: Peak assignment of FTIR spectra for (S15) precipitated HA, Sr = 0 mol%, (S16) precipitated HA, Sr = 25 mol%, (S17) precipitated HA, Sr = 50 mol%, (S18) precipitated HA, Sr = 75 mol%, (S19) precipitated HA, Sr = 100 mol%.

S15: Precipitated HA, Sr = 0mol%	S16: Precipitated HA, Sr = 25mol%	S17: Precipitated HA, Sr = 50mol%	S18: Precipitated HA, Sr = 75mol%	S19: Precipitated HA, Sr = 100mol%	Assignment	Reference
470	470	470	463	456	O-P-O bending mode v_2	[36, 156-158]
561-601	561-601	561-601	555-595	555-588	O-P-O bending mode v_4	[36, 156-158]
634	553-620	551-625	547-618	535	OH$^-$ libration mode	[20, 36, 148, 157]
878	878	871	$\sim$898	878	B-site CO_3 vibration mode v_2/ HPO_4^{2-}	[113, 159, 160]/ [152, 156, 162]
963	957	950	949	943	P-O stretching vibration mode v_1	[36, 156-158]
826, 831, 878, 1378	831, 878, 1378, 1772	831, 871, 1378, 1766	825, 871, 1378, 1772	831, 878, 1378, 1766	Residual nitrate	[152, 161]
1029, $\sim$1095	1029, $\sim$1082	$\sim$1029, $\sim$1082	$\sim$1029, $\sim$1081, $\sim$1128	$\sim$1023, $\sim$1075	P-O stretching vibration mode v_3	[36, 156-158]
$\sim$1443	1306-1556	1292-1542	1292-1582	1292-1563	A-type/ B-type CO_3 vibration mode v_3	[113, 114, 159, 160, 179, 180]
1634, 3010, 3188, 3431	1634, $\sim$3016, 3148, 3424	1634, $\sim$3010, 3148, 3424	1634, 3016, 3148, 3437	1634, 3015, 3148, 3424	Adsorbed water	[158, 161]
$\sim$2371	$\sim$2365	2411	$\sim$2431	$\sim$2378	CO_2 in air	[106]
3571	3576	3576	3582	3589	OH$^-$ stretching mode	[20, 36, 148, 157]

3.4.3. Raman spectroscopy studies

Figure 46 shows the Raman spectra of five HA samples with increased Sr substitution from 0 to 100 mol%. The Raman peak positions and their assignments are summarized in Table 22.
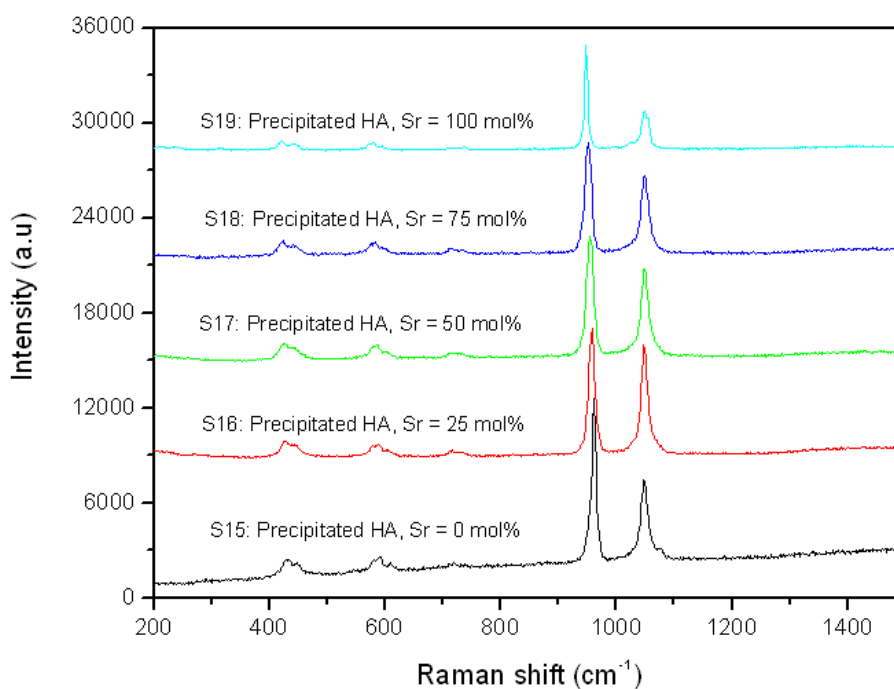

Figure 46: Raman spectra of five precipitated HA samples with different Sr substitutions: (S15) Sr = 0 mol%, (S16) Sr = 25 mol%, (S17) Sr = 50 mol%, (S18) Sr = 75 mol%, (S19) Sr = 100 mol%.

As shown in Figure 46, in the case of S15 four HA characteristic peaks appear at 961 cm^{-1} (PO$_4^{3-}$ mode v_1), 450-400 cm^{-1} (PO$_4^{3-}$ mode v_2), 1076-1028 cm^{-1} (PO$_4^{3-}$ mode v_3), and 610-579 cm^{-1} (PO$_4^{3-}$ mode v_4) [10, 121] as it has been mentioned earlier. By increasing Sr substitution from 0 to 100 mol%, a downshift of the PO$_4^{3-}$ mode v_1 from 961 to 948 cm^{-1} is observed. The relationship between the Raman peak positions of PO$_4^{3-}$ mode v_1 with increasing Sr substitution from 0 to 100 mol% is plotted in Figure 47 shown below.
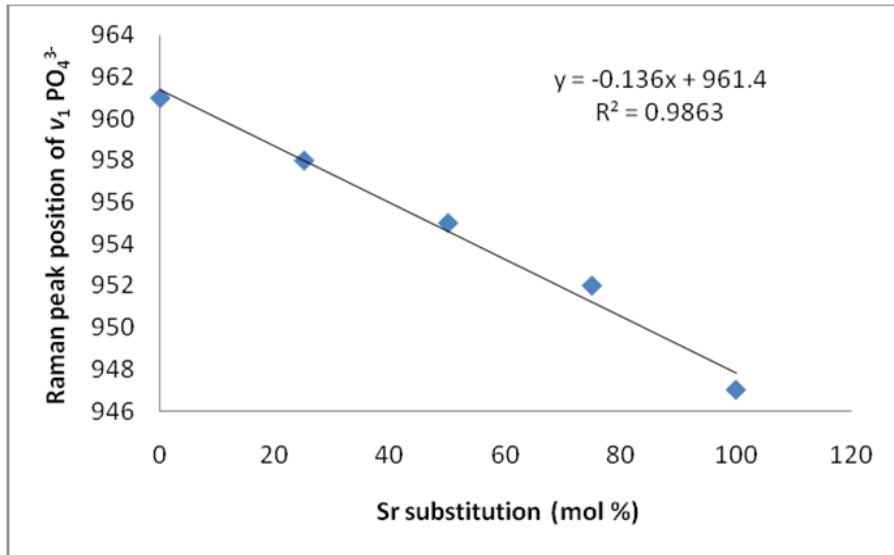
Figure 47: The changes of the Raman peak positions of v_1 PO_4^{3-} with Sr substitution from 0 to 100 mol%.

In Figure 52, a linear decrease of the Raman peak positions of PO_4^{3-} mode v_1 with increasing Sr substitution from 0 to 100 mol% is observed. A similar Raman shift was also noticed by *Donnell and co-workers* [95], who suggested that the shift was due to the smaller cation size of Ca being substituted by the larger cation of Sr in the apatite lattice. This can be explained by the Szigeti relationship [181], as shown in Equation 14.

$$f = \frac{1}{c}\sqrt{\frac{k}{\mu}},$$
(14)

where f is the frequency of vibration, c is the velocity of light in vacuum (2.998×10^8 ms^{-1}), k is the bond force constant (typically in Nm^{-1}) and μ is the reduced mass of two bonding atoms (equal to $m_1 m_2 / (m_1 + m_2)$). It is known that Ca-O and Sr-O have similar bond enthalpies, which are 402.1 and 425.5 KJ mol^{-1}, respectively. The k for Ca-O and Sr-O is expected to be similar, too. Therefore, when Sr substitutes Ca, μ increases and thus f decreases [95] confirming our FTIR results which support the idea that Sr enters the apatite lattice.

As briefly discussed in paragraph *3.1.3*, the Raman peaks in the region around 713 cm^{-1} appear only in the case of precipitated apatite samples (S15-S19) as shown in Figure 46.

According to the literature, the peaks that appear at around 690, 716, and 751 cm^{-1} are associated with CO_3^{2-} mode v_4 vibrations [164]. Therefore, it can be suggested, that the Raman peaks present in the region of 713-737 cm^{-1} in all precipitated apatite samples can be attributed to the presence of CO_3^{2-} ions. However, as no CO_3^{2-} source was used during the synthesis of the above samples, the appearance of the CO_3^{2-} peaks in the Raman spectra could be caused by the fact that all experimental procedures were carried out in air [106]. The above Raman studies support the FTIR results discussed in paragraph *3.4.2* and confirm the presence of CO_3^{2-} content in all chemical precipitated apatite samples.

Table 22: Peak assignment of Raman spectra for (S15) precipitated HA, Sr = 0 mol% (S16) precipitated HA, Sr = 25 mol%, (S17) precipitated HA, Sr = 50 mol%, (S18) precipitated HA, Sr = 75 mol%, and (S19) precipitated HA, Sr = 100 mol%.

S15: Precipitated HA, Sr = 0 mol%	S16: Precipitated HA, Sr = 25 mol%	S17: Precipitated HA, Sr = 50 mol%	S18: Precipitated HA, Sr = 75 mol%	S19: Precipitated HA, Sr = 100 mol%	Assignment	Reference
430, 446	428, ∼444	425, 438	426, 439	422, 440	PO_4^{3-} v_2 mode	[10, 121]
578, 594, 610	576, 590, 605	∼580, 587, ∼602	576, 584, ∼598	∼572, 580, 596	PO_4^{3-} v_4 mode	[10, 121]
961	958	955	952	947	PO_4^{3-} v_1 mode	[10, 121]
1048, 1076	1048	1048	1048	1024, 1048, 1054	PO_4^{3-} v_3 mode	[10, 121]
1076	-	-	-	-	B-site CO_3^{2-} mode v_1	[121]
∼716	713	∼718	∼711, ∼731	∼719, 737	CO_3^{2-} mode v_4	[164]

3.4.4. ^{31}P MAS-NMR spectroscopy studies

Figure 48 shows ^{31}P MAS-NMR spectra of five precipitated HA samples with different Sr substitutions. The ^{31}P chemical shift and their peak width at half maximum (FWHM) are listed in Table23.
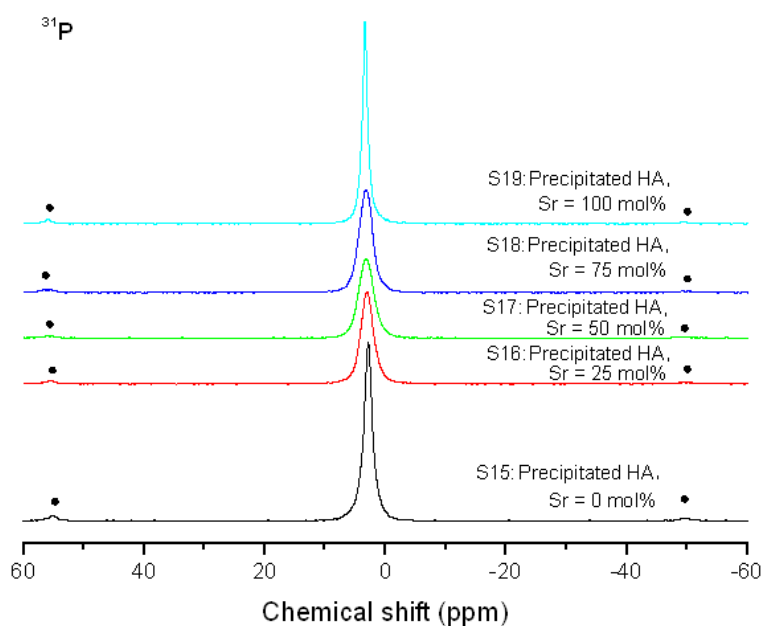
Figure 48: ^{31}P MAS-NMR spectra of five precipitated HA samples with different Sr substitutions: (S15) Sr = 0 mol%, (S16) Sr = 25 mol%, (S17) Sr = 50 mol%, (S18) Sr = 75 mol%, (S19) Sr = 100 mol%. The side bands are indicated by •

The characteristic peak of crystalline HA in the ^{31}P MAS-NMR spectra was reported in the literature to appear at 2.9 ppm [167, 168]. This is in good agreement with this work and specifically, the sample S15 exhibits a strong and sharp peak at 2.9 ppm as shown in Figure 48. By increasing Sr substitution from 0 to 100 mol%, there is a chemical shift from 2.9 to 3.4 ppm and all peaks are associated with phosphorus in an orthophosphate environment Q^0 [174, 175]. Both apatite samples with 0 (S15) and 100 mol% Sr substitution (S19), are exhibiting the smallest FWHM, and the higher peak intensity indicating that these two samples exhibit highly ordered apatite structure and also contain relatively larger apatite crystals. In the contrary, the middle three Ca-Sr-HA samples with Sr substitution, ranging from 25 to 75 mol%, exhibit larger FWHM together with less intensive peak intensity reflecting their smaller crystallite size and

possibly poorer degree of crystallinity. This is particularly obvious in the case of S17, which contains 50 mol% Sr. The above observations show an excellent agreement with the XRD results indicating that Sr enters into the apatite lattice substituting Ca.

In addition, the peak width and peak intensity seem to be affected by the increase in Sr substitution in the apatite lattice, and the relationship between the ^{31}P MAS-NMR FWHM and the increased Sr substitution from 0 to 100 mol% is plotted in Figure 49.

$$y = -0.0007x^2 + 0.0596x + 1.5649$$
$$R^2 = 0.9736$$
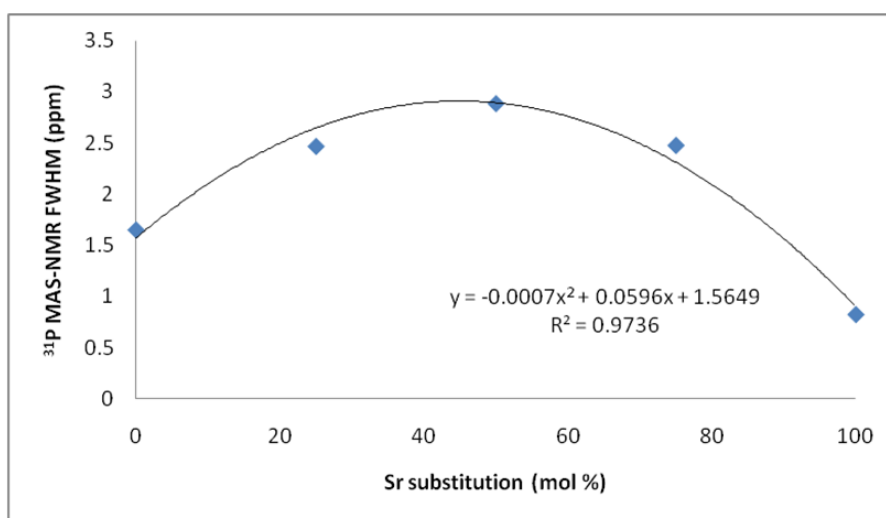
Figure 49: Changes of the ^{31}P MAS-NMR peak FWHM with increased Sr substitution from 0 to 100 mol%.

$$y = 0.0048x + 2.9$$
$$R^2 = 0.9474$$
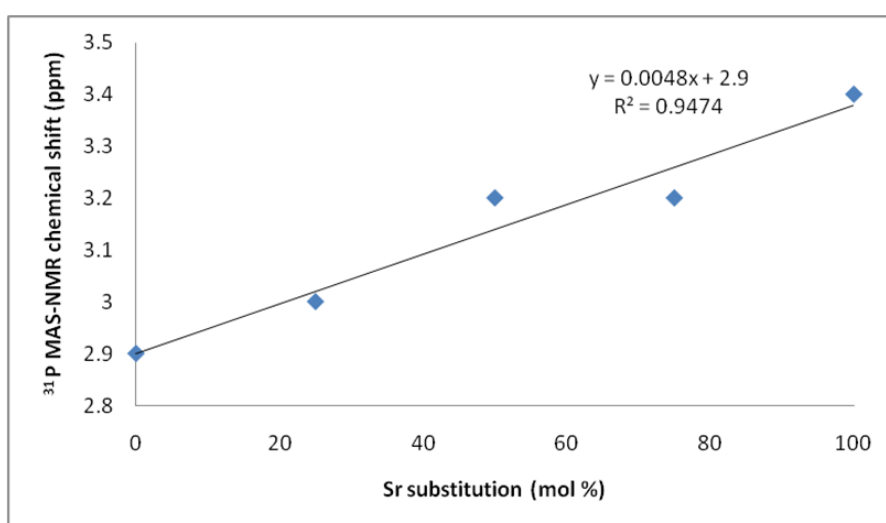
Figure 50: The changes of the chemical shift with increased Sr substitution from 0 to 100 mol%.

As presented in Figure 50, the chemical shift increases with increasing Sr substitution from 0 to 100 mol% and it seems that the chemical shift is strongly dependent on the cation field strength which is defined as the ratio of charge to cation radius [182].

Table 23: [31] P MAS-NMR chemical shift and peak width at half maximum (FWHM) of five precipitated HA samples with different Sr substitution: (S15) Sr = 0 mol%, (S16) Sr = 25 mol%, (S17) Sr = 50 mol%, (S18) Sr = 75 mol%, (S19) Sr = 100 mol%.

Sample	Expected Sr Substitution (mol%) in the Solid Phase	Chemical Shift (ppm)	FWHM (ppm)
S15	-	2.9	1.65
S16	25	3.0	2.47
S17	50	3.2	2.89
S18	75	3.2	2.48
S19	100	3.4	0.82

3.5. Effect of Silicon substitutions on the apatite structure

3.5.1. X-ray diffraction studies

Figure 51 shows the powder XRD patterns of six HA samples with different Si substitutions. Increasing Si substitution from 0 to 0.81 wt%, no significant changes are observed in Figure 51. Furthermore, there is no indication for the formation of any other secondary phase. This suggests that incorporation of Si into the HA samples does not have any effect on the phase composition or crystallographic structure. This is in good agreement with previously published data [134, 183, 184].
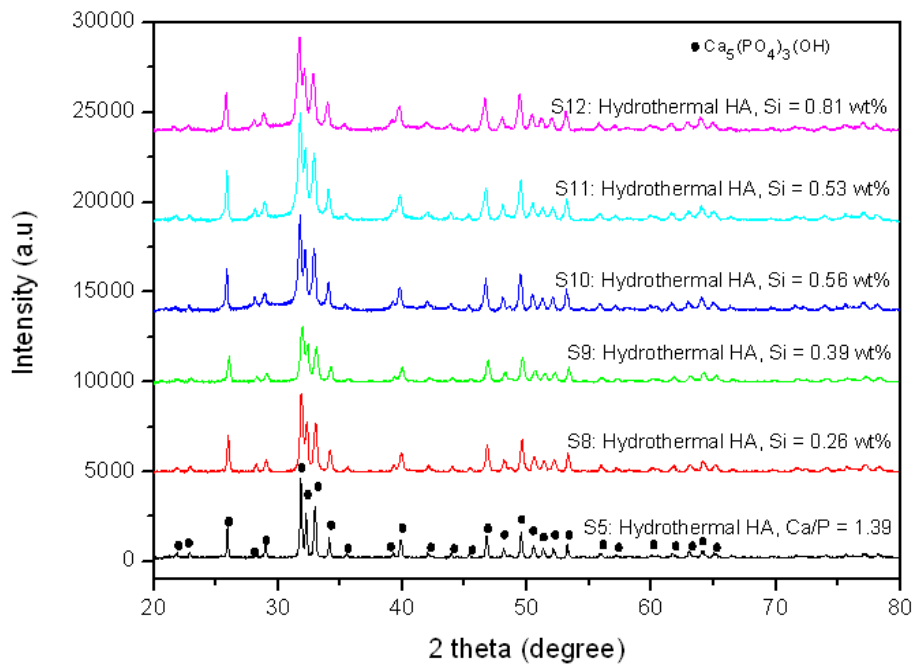
Figure 51: Powder XRD patterns of six hydrothermal HA samples with different Si substitution: (S5): Ca/P = 1.39, (S8) Si = 0.26 wt%, (S9) Si = 0.39 wt%, (S10) Si = 0.56 wt%, (S11) Si = 0.53 wt%, (S12) Si = 0.81 wt%.
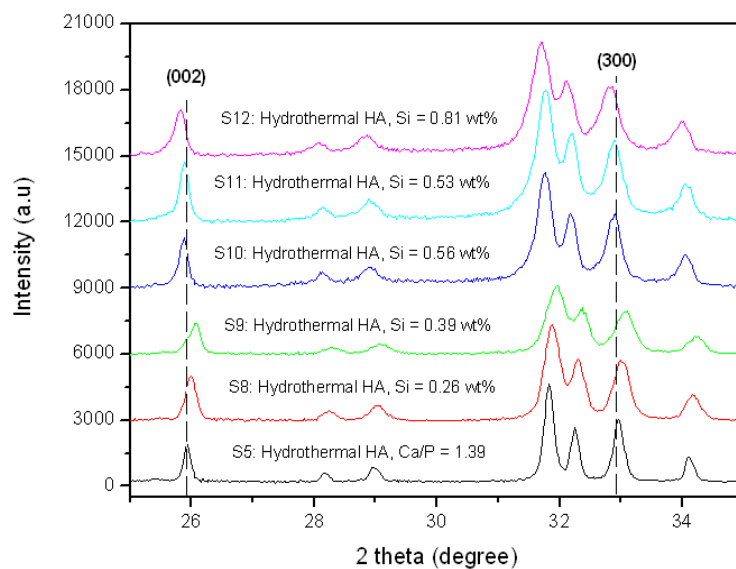
Figure 52: Powder XRD patterns of six HA samples with different Si substitution in the region of 25-35°.

Figure 52 shows clearly small changes in (002) and (300) reflections in the Si substituted apatite samples compared to the control hydrothermal apatite sample S5. By increasing Si substitution from 0 to 0.39 wt%, a shift of both (002) and (300) reflections toward higher values of 2 theta can be observed. The direction of the shift in (002) and

(300) reflections was related by other researchers to an increase or decrease of the a- and c-axis of the apatite lattice. Based on our data however it is not possible to make such correlations as we did not measure the a- and c-axis and we did not have similar pattern of changes as published elsewhere [96, 97, 124]. In addition, the peak intensity and peak width also vary with increasing Si substitution as shown in Figure 51. Such observations suggest that the apatite samples may have different crystallite size and possibly different crystallinity. The crystallite size of the above samples is calculated and presented in Table 24.

Table 24: Measured Si substitution, phase identification, and crystallite size of six hydrothermal HA samples with different Si substitutions: (S5): Ca/P = 1.39, (S8) Si = 0.26 wt%, (S9) Si = 0.39 wt%, (S10) Si = 0.56 wt%, (S11) Si = 0.53 wt%, (S12) Si = 0.81 wt%.

Sample	Measured Si substitution (wt%) in the solid phase	Phase identification	Crystallite size (nm)
S5	-	HA	42
S8	0.26	HA	24
S9	0.39	HA	19
S10	0.56	HA	23
S11	0.53	HA	10
S12	0.81	HA	12
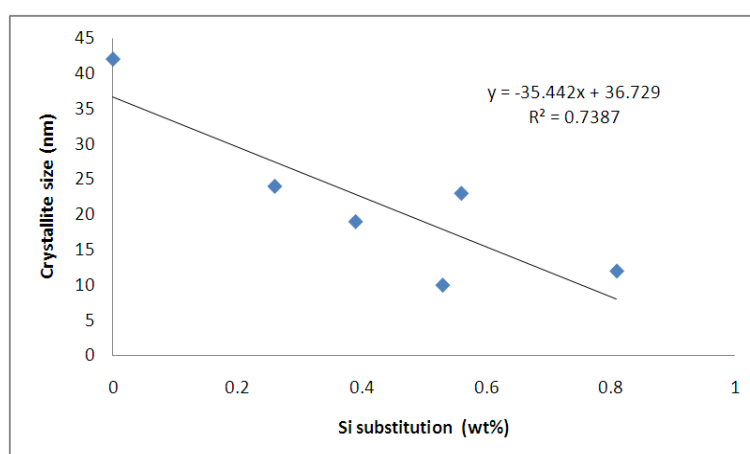
Figure 53: The changes of the crystallite size with increased Si substitution from 0 to 0.81 wt%.

In order to study the effect of Si substitution on the crystallite size of apatite, the crystallite size of the above samples is plotted against wt% Si substitution in Figure 53. As shown in Figure 53, a general decrease in the apatite crystallite size with increasing Si substitution is observed. However, such changes in the crystallite size should maybe not be attributed to the presence of Si solely as there is strong evidence of CO_3^{2-} substitution taken place during the synthesis of the apatite samples.

3.5.2. FTIR spectroscopy studies

Figure 54 shows the FTIR spectra of six HA samples with different Si substitutions. The absorption bands and their assignments are summarized in Table 25.
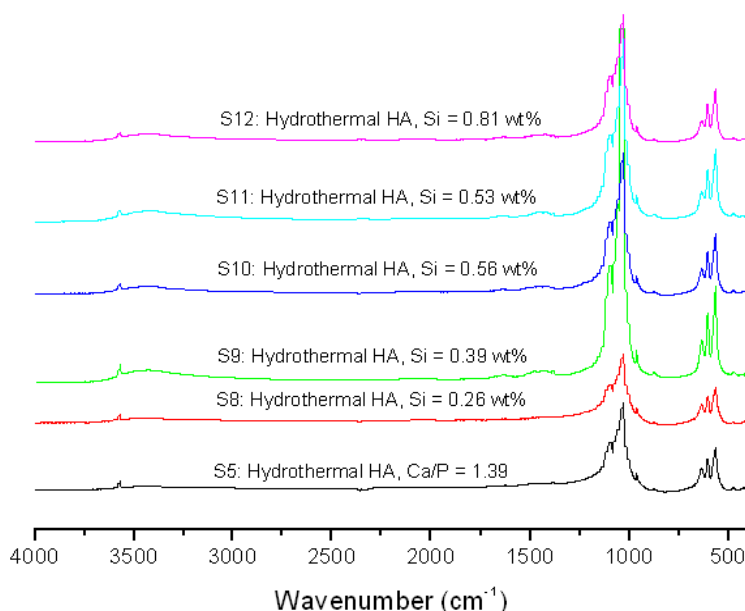
Figure 54: FTIR spectra of six hydrothermal HA samples with different Si substitutions: (S5): Ca/P = 1.39, (S8) Si = 0.26 wt%, (S9) Si = 0.39 wt%, (S10) Si = 0.56 wt%, (S11) Si = 0.53 wt%, (S12) Si = 0.81 wt%.

As described in paragraph *3.1.2*, in the case of S5 four PO_4^{3-} modes and two OH^- associated bands appear at 476 cm^{-1} (PO_4^{3-} v_2), 561-601 cm^{-1} (PO_4^{3-} v_4), 963 cm^{-1} (PO_4^{3-} v_1), 1029 and 1095 cm^{-1} (PO_4^{3-} v_3), and 634 cm^{-1} (OH^- libration) and 3571 cm^{-1} (OH^- stretching) [20, 36, 148, 156-158] assigned to characteristic bands of a HA structure. In addition, due to the appearance of absorption bands at 878 cm^{-1} and 1424-1483 cm^{-1}

associated with the B-type CO_3^{2-} vibration modes v_2 and v_3 [113, 159, 160], there is a strong evidence that CO_3^{2-} substitution takes place in the PO_4^{3-} tetrahedra of the apatite structure during synthesis. With increasing Si substitution from 0 to 0.81 wt% the same four PO_4^{3-} modes and two OH⁻ bands are also observed in the spectra of all samples.

Tang and co-workers reported, that with the substitution of SiO_4^{4-} into the HA structure for PO_4^{3-} tetrahedra, some loss of OH⁻ groups occur in order to maintain the charge balance [97]. Therefore, the intensity of the OH⁻ associated bands [20, 36, 148, 157] at 3571 and 634 cm⁻¹ would be expected to decrease with increasing Si substitution. However, this cannot be concluded from the FTIR spectra in Figure 54.

Leventouri and co-workers reported that two additional bands at 890 and 756 cm⁻¹ were observed in heat-treated 0.4 wt% Si-HA sample [133]. Additionally, *Gibson and co-workers* observed three additional bands at 954, 890, and 840 cm⁻¹ in the FTIR spectra of 0.4 wt% Si heat-treated HA sample [96]. *Tang and co-workers* further reported that a new band at 870 cm⁻¹ corresponded to Si-O vibration modes of SiO_4^{4-} groups was observed in the Si-substituted HA samples with Si substitution ranging from 0.8 to 4wt%; and another band at 800 cm⁻¹ assigned to Si-O-Si vibration mode when the Si reached to the higher concentration in the region of 1.5-4 wt% [97].
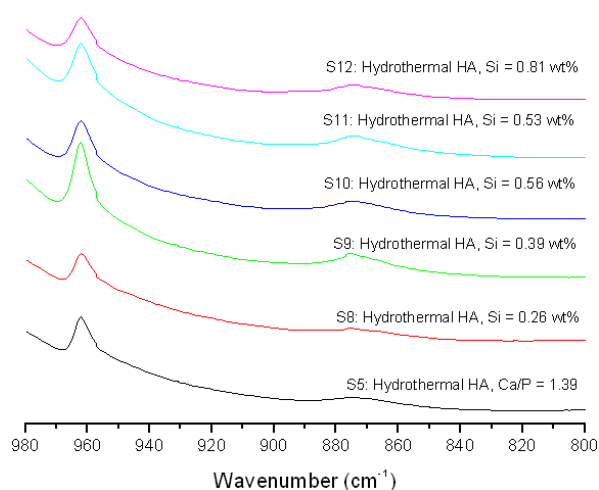
Figure 55: FTIR spectra of six hydrothermal HA samples with different Si substitution in the region of 980-800 cm⁻¹.

Looking closer in Figure 55, two absorption bands at 963 and 871 cm^{-1} are observed in all apatite samples, including S5 that has no Si substitution. It is considered therefore that the presence of the above two peaks cannot be related to the Si substitution. In the contrary, CO_3^{2-} [113, 159, 160], HPO_4^{2-} [152, 156], and residual nitrates [152, 161] can also appear at similar wave number positions and consequently both of the above bands should be associated with the presence of the above characteristic groups. It should be mentioned, that the absorption bands at 871 cm^{-1} and in the region of 1417-1489 cm^{-1} present in all Si-containing apatite samples (S9-S13) correspond to B-type CO_3^{2-} vibration modes v_2 and v_3 [113, 159, 160]. This suggests that CO_3^{2-} ions are present in the apatite structure of all the above samples.

Table 25: Peak assignment of FTIR spectra for (S5): hydrothermal HA, Ca/P = 1.39, (S8) hydrothermal HA, Si = 0.26 wt%, (S9) hydrothermal HA, Si = 0.39 wt%, (S10) hydrothermal HA, Si = 0.56 wt%, (S11) hydrothermal HA, Si = 0.53 wt%, (S12) hydrothermal HA, Si = 0.81 wt%.

S5: Hydrothermal HA, Ca/P = 1.39	S8: Hydrothermal HA, Si = 0.26 wt%	S9: Hydrothermal HA, Si = 0.39 wt%	S10: Hydrothermal HA, Si = 0.56 wt%	S11: Hydrothermal HA, Si = 0.53 wt%	S12: Hydrothermal HA, Si = 0.81 wt%	Assignment	Reference
476	476	476	470	476	476	O-P-O bending mode v_2	[36, 156-158]
561-601	561-608	561-601	561-601	561-608	561-608	O-P-O bending mode v_4	[36, 156-158]
634	634	634	634	634	634	OH$^-$ libration mode	[20, 36, 148, 157]
871	871	871	871	871	871	B-site CO_3 vibration mode v_2/ HPO_4^{2-}	[113, 159, 160]/ [152, 156, 162]
963	963	963	963	963	963	P-O stretching vibration mode v_1	[36, 156-158]
871, 1384	871, 1384	871, 1384	871, 1378	871, 1384	871, 1378	Residual nitrate	[152, 161]
1029, ~1095	1029, ~1095	~1035, ~1088	1028, ~1088	1029, ~1095	1029, ~1095	P-O stretching vibration mode v_3	[36, 156-158]
1424-1483	1432-1489	1424-1489	1424-1463	1417-1451	1424-1457	B-site CO_3^{2-} vibration mode v_3	[113, 159, 160]
1641, 3424	1641, 3431	1634, 3431	1634, 3431	1634, 3418	1634, 3424	Adsorbed water	[158, 161]
3571	3571	3571	3571	3571	3571	OH$^-$ stretching mode	[20, 36, 148, 157]

3.5.3. Raman spectroscopy studies

Figure 56 shows the Raman spectra of six HA samples with different Si substitutions. The Raman peak positions and their assignments are summarized in Table 26.
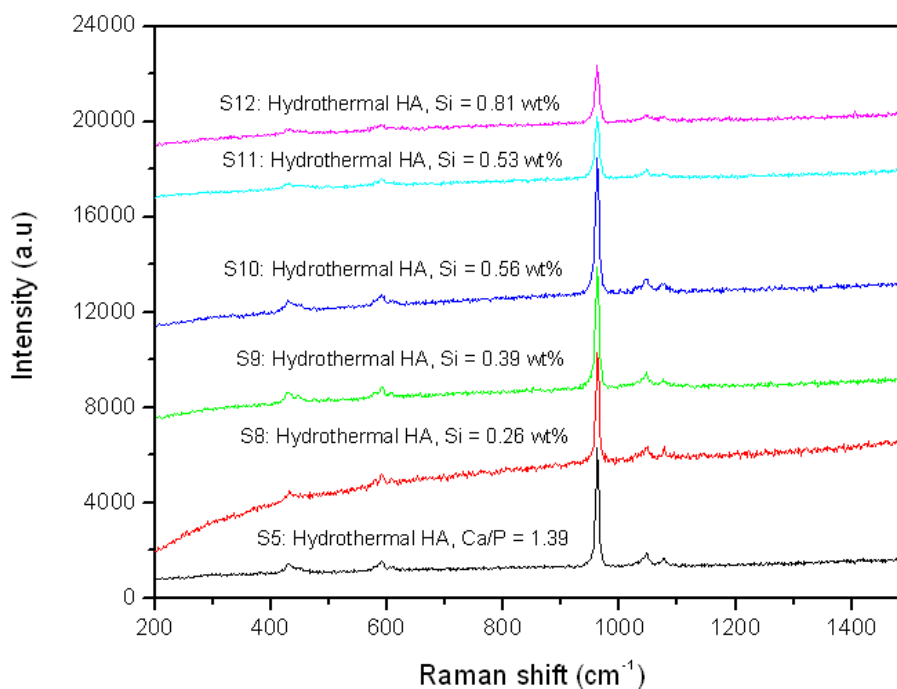

Figure 56: Raman spectra of six hydrothermal HA samples with different Si substitutions: (S5): Ca/P = 1.39, (S8) Si = 0.26 wt%, (S9) Si = 0.39 wt%, (S10) Si = 0.56 wt%, (S11) Si = 0.53 wt%, (S12) Si = 0.81 wt%.

The Raman spectra are in good agreement with the FTIR spectra showing that all samples exhibit the main characteristic bands for an apatite structure [10, 121]. In addition, because both PO_4^{3-} mode v_3 and B-type CO_3^{2-} mode v_1 may appear in the same Raman shift position [10, 121], the Raman peak at around 1076 cm^{-1} observed in all above samples can be assigned to the presence of both PO_4^{3-} mode v_3 and B-type CO_3^{2-} mode v_1. Irregular changes in the Raman peak intensity with increasing Si substitution are also observed. This suggests that crystallinity changes with increasing Si substitution [165], however, the pattern of changes is irregular. The suggests possible disorder in the apatite lattice due to the presence of varied amounts of CO_3^{2-} substitution associated with different Si substitutions. Furthermore, *Zou and co-workers* reported Raman peaks at 845, 890 and 949 cm^{-1} in 1.5 wt% Si substituted apatite samples [185].

These peaks are not present in our Raman spectra possibly due to the smaller Si substitution in our apatite samples.

Zou and co-workers [185] observed that in the Raman spectra both PO_4^{3-} and OH^- stretching modes were broader in the Si substituted HA samples. Additionally, they reported that when the Si substitution reached 1.5 wt% three additional peaks appeared at 845, 890 and 949 cm^{-1} [185]. In the present Raman studies, due to the Raman measurement range being limited in the region of 200-1500 cm^{-1}, the changes in the OH^- stretching mode with Si substitution cannot be considered, and a general peak broadening in the PO_4^{3-} mode v_1 at around 963 cm^{-1} is observed in almost all samples, except in the case of S12, as presented in Figure 57.
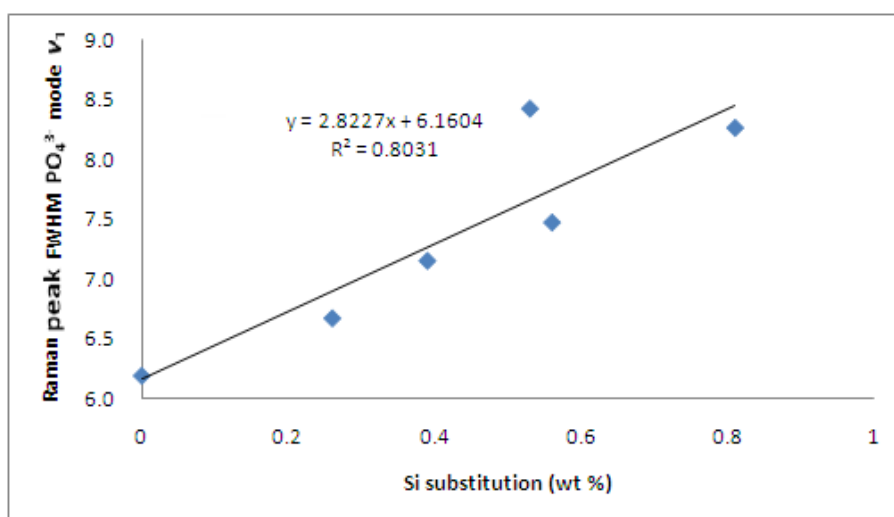
Figure 57: Changes in the Raman peak FWHM of the PO_4^{3-} mode v_1 with increasing Si substitution from 0 to 0.81 wt%.

As shown in Figure 57, the Raman FWHM of the PO_4^{3-} mode v_1 is generally increased with increasing Si substitution from 0 to 0.81 wt%. According to the literature, the peak broadening in the PO_4^{3-} mode v_1 should be due to the increased structure disordering induced by the presence of the substitution ions [173]. In addition, *De Mul and co-workers* suggested that the peak width of the PO_4^{3-} mode v_1 can be highly dependent also on the level of CO_3^{2-} substitution [82].

Table 26: Peak assignment of Raman spectra for (S5): hydrothermal HA, Ca/P = 1.39, (S8) hydrothermal HA, Si = 0.26 wt%, (S9) hydrothermal HA, Si = 0.39 wt%, (S10) hydrothermal HA, Si = 0.56 wt%, (S11) hydrothermal HA, Si = 0.53 wt%, (S12) hydrothermal HA, Si = 0.81 wt%.

S5: Hydrothermal HA, Ca/P = 1.39	S8: Hydrothermal HA, Si = 0.26wt%	S9: Hydrothermal HA, Si = 0.39wt%	S10: Hydrothermal HA, Si = 0.56wt%	S11: Hydrothermal HA, Si = 0.53wt%	S12: Hydrothermal HA, Si = 0.81wt%	Assignment	Reference
430, 446	430	431, 447	430, 453	432, ~445	~425, 433, 453	PO_4^{3-} v_2 mode	[10, 121]
578, 594, 610	578, 591, 610	574, 591, 607	592, 607	~581, 591, ~601	596	PO_4^{3-} v_4 mode	[10, 121]
961	963	963	963	963	963	PO_4^{3-} v_1 mode	[10, 121]
1048, 1076	1047, 1077	1047, 1075	1045, 1074	1045, ~1073	1045, 1073	PO_4^{3-} v_3 mode	[10, 121]
1076	1077	1075	1074	~1073	1073	B-site CO_3^{2-} mode v_1	[121]

3.5.4. ^{31}P MAS-NMR spectroscopy studies

Figure 58 shows ^{31}P MAS-NMR spectra of six HA samples with different Si substitutions. The ^{31}P chemical shift and full-width at half peak maximum are listed in Table 27.
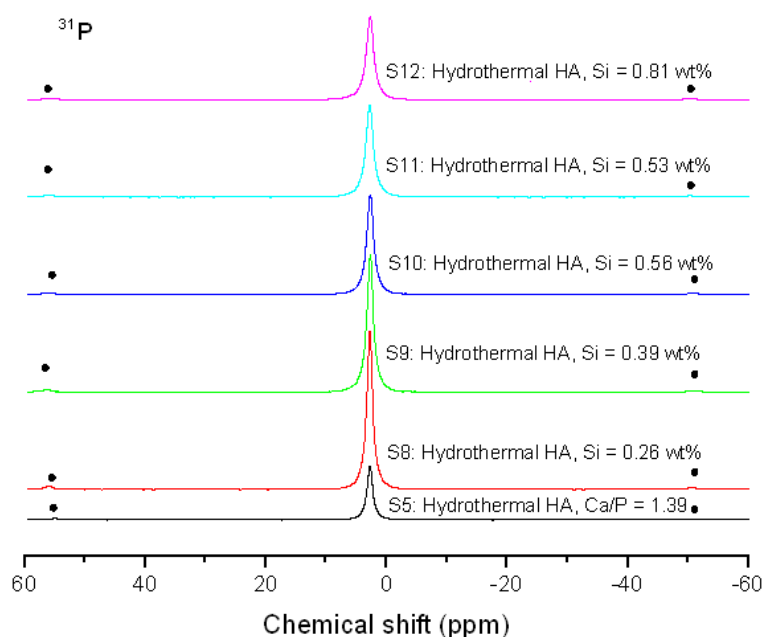
Figure 58: ^{31}P MAS-NMR spectra of six hydrothermal HA samples with different Si substitutions: (S5): Ca/P = 1.39, (S8) Si = 0.26 wt%, (S9) Si = 0.39 wt%, (S10) Si = 0.56 wt%, (S11) Si = 0.53 wt%, (S12) Si = 0.81 wt%. The side bands are indicated by •

As mentioned previously, in the case of S5, a single HA crystalline phase has been identified (also by XRD) that is associated with a peak at 2.8 ppm in the ^{31}P MAS-NMR spectrum [186].

By increasing Si substitution from 0 to 0.81 wt%, the peak shifts to ppm values from 2.6 to 2.9. No particular trend in the chemical shift was observed with increasing Si substitution but the local changes within the apatite lattice seem to affect slightly the chemical shift in the ^{31}P MAS-NMR spectra although the amount of Si in the substituted samples is rather small. This shows that ^{31}P MAS-NMR is a very sensitive technique for the local characterisation of the apatite lattice. Generally, all samples

exhibit clearly phosphorus in an orthophosphate environment.

On the other hand, the peak width and the peak intensity vary systematically with increasing Si substitution, as noticed in Figure 58 and Table 27. This observation is in good agreement with the XRD, FTIR and Raman data which clearly show that both Si substitution and the presence of CO_3^{2-} groups affect considerably the degree of crystallinity and the crystal size of the substituted apatite samples.

As mentioned previously, in the case of S5, a single HA crystalline phase has been identified (also by XRD) that is associated with a peak at 2.8 ppm in the ^{31}P MAS-NMR spectrum [186].

By increasing Si substitution from 0 to 0.81 wt%, the peak shifts to ppm values from 2.6 to 2.9. No particular trend in the chemical shift was observed with increasing Si substitution but the local changes within the apatite lattice seem to affect slightly the chemical shift in the ^{31}P MAS-NMR spectra although the amount of Si in the substituted samples is rather small. This shows that ^{31}P MAS-NMR is a very sensitive technique for the local characterisation of the apatite lattice. Generally, all samples exhibit clearly phosphorus in an orthophosphate environment. On the other hand, the peak width and the peak intensity vary systematically with increasing Si substitution, as noticed in Figure 58 and Table 27. This observation is in good agreement with the XRD, FTIR and Raman data, which clearly show that both Si substitution and the presence of CO_3^{2-} groups affect considerably the degree of crystallinity and the crystal size of the substituted apatite samples.

**Table 27:** ^{31}P MAS-NMR chemical shift and peak width at half maximum (FWHM) of six hydrothermal HA samples with different Si substitution: (S5): Ca/P = 1.39, (S8) Si = 0.26 wt%, (S9) Si = 0.39 wt%, (S10) Si = 0.56 wt%, (S11) Si = 0.53 wt%, (S12) Si = 0.81 wt%.

Sample	Measured Si substitution (wt%) in the Solid Phase	Chemical shift (ppm)	FWHM (ppm)
S5	-	2.8	1.11
S8	0.26	2.9	1.09
S9	0.39	2.6	1.20
S10	0.56	2.6	1.37
S11	0.53	2.9	1.49
S12	0.81	2.9	1.49

3.6. Effect of Carbonate substitutions on the apatite structure

3.6.1. X-ray diffraction studies

Figure 59 shows the powder XRD patterns of three HA samples with increased CO_3^{2-} substitution up to 21 wt%. Sample S5 is used as the control HA sample. By increasing CO_3^{2-} substitution to 5 wt% (sample S13) the XRD pattern remains almost identical to the XRD pattern of S5. This is in good agreement with the literature. For example, *De Mul and co-workers* reported that HA lattice was able to take up to 4.5 wt% of CO_3^{2-} without significant changes in the XRD pattern [82]. By further increasing the CO_3^{2-} substitution to 21 wt% (sample S14) on the other hand, results in the formation of a HA and a $CaCO_3$ crystalline phase, as shown in Figure 59. The formation of a biphasic material in the case of S14 indicates that the 21 wt% CO_3^{2-} is probably beyond the capacity of the apatite lattice to substitute CO_3^{2-} for PO_4^{3-} and implies that CO_3^{2-} substitution has a considerable effect on the apatite crystallization [83, 100] considering the decrease in the crystallite size with increasing CO_3^{2-} substitution, as shown in Table 28.
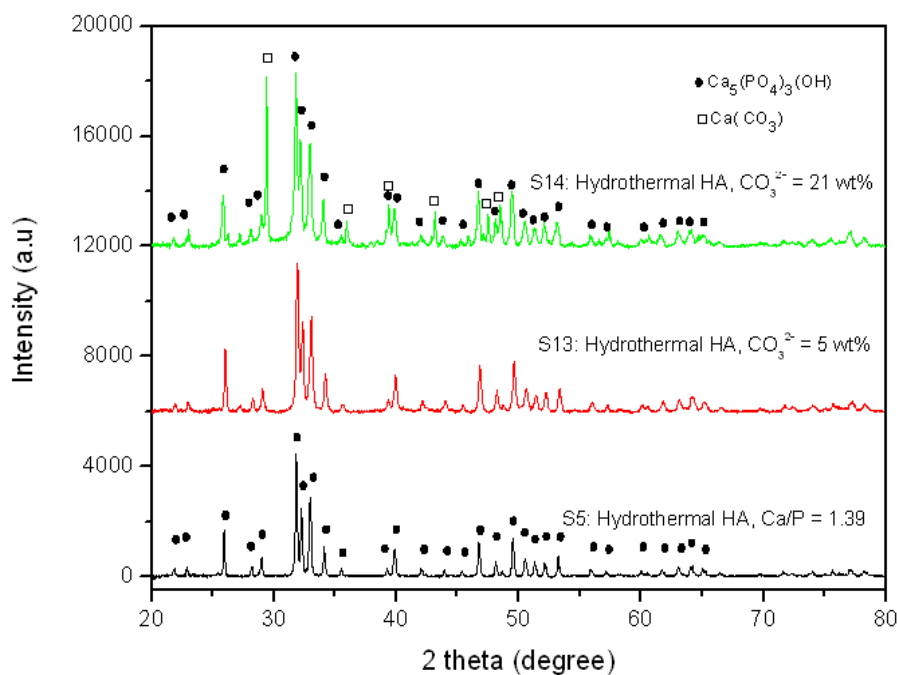
Figure 59: Powder XRD patterns of three different hydrothermal HA samples: (S5) Ca/P = 1.39, (S13) CO_3^{2-} = 5 wt%, (S14) CO_3^{2-} = 21 wt%.

Table 28: Measured CO_3^{2-} substitution, phase composition, and crystallite size of three hydrothermal HA samples: (S5) Ca/P = 1.39, (S13) CO_3^{2-} = 5 wt%, (S14) CO_3^{2-} = 21 wt%.

Sample	Measured CO_3^{2-} substitution (wt%) in the solid phase	Phase composition	Crystallite size (nm)
S5	-	HA	42
S13	5	HA	28
S14	21	53 wt% HA	16
		47 wt% CaCO$_3$	60

In addition, with increased CO_3^{2-} substitution from 0 to 21 wt%, several shifts in the XRD patterns are noticed, and particularly in the (002) and (300) reflection, as shown in Figure 60.
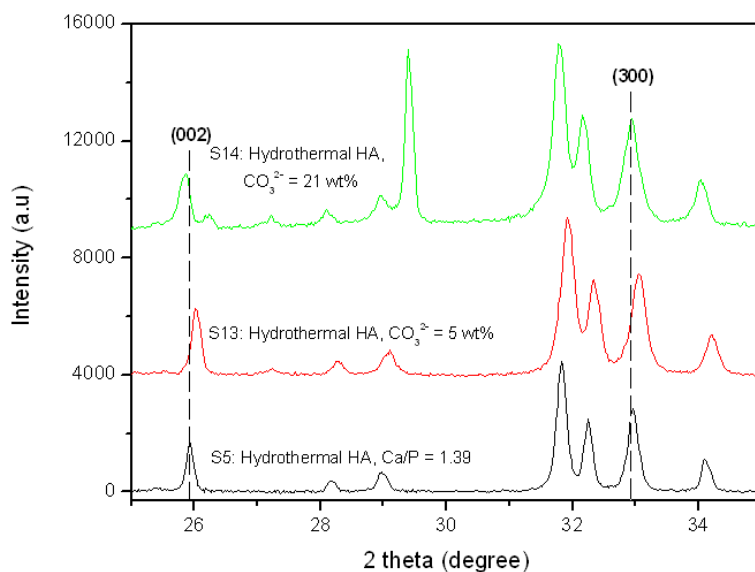
Figure 60: Powder XRD patterns of three different hydrothermal HA samples in the region of the 2 theta value from 25 to 35 degree: (S5) Ca/P = 1.39, (S13) CO_3^{2-} = 5 wt%, (S14) CO_3^{2-} = 21 wt%.

As observed in Figure 60, by increasing CO_3^{2-} to 5 wt% (S13), both (002) and (300) reflections shift to higher values of 2 theta. *Legeros and co-workers* reported a shift of the (300) reflection to higher 2 theta values and a shift of (002) to lower 2 theta values with CO_3^{2-} and suggested that this was due to decreased *a*-axis dimension and increased *c*-axis dimension with increasing substitution [124]. *Nelson and co-workers* also reported that the decrease in the *a*-axis and increase in the *c*-axis in the apatite lattice was a typical effect, brought by the incorporation of B-type CO_3^{2-} substitution into the HA structure [101]. However, it is not possible to reach a similar conclusion with the present results as it seems that both reflections shift to higher 2 theta values. A further increase in the CO_3^{2-} substitution to 21 wt% results in the shift of both (002) and (300) reflection to lower 2 theta values but no correlation can be possibly made to the observations that *Legeros and co-workers* and *Nelson and co-workers* have made as the observations made with the current data are not the same with the results published by the above authors. Comparing S13 and S14 it can be said that for S13 the (002) and (300) reflections shift towards the opposite direction compared to S14. This could be explained if HPO_4^{2-} ions or some entrapped water molecules were present in S14 [137, 138]. Finally, the degree of crystallinity seems to be the same for all samples as the peak intensity does not show significant changes across the substituted samples.

3.6.2. FTIR spectroscopy studies

Figure 61 shows the FTIR spectra of four HA samples with different CO_3^{2-} substitutions. The absorption band positions and their assignments are summarized in Table 29.
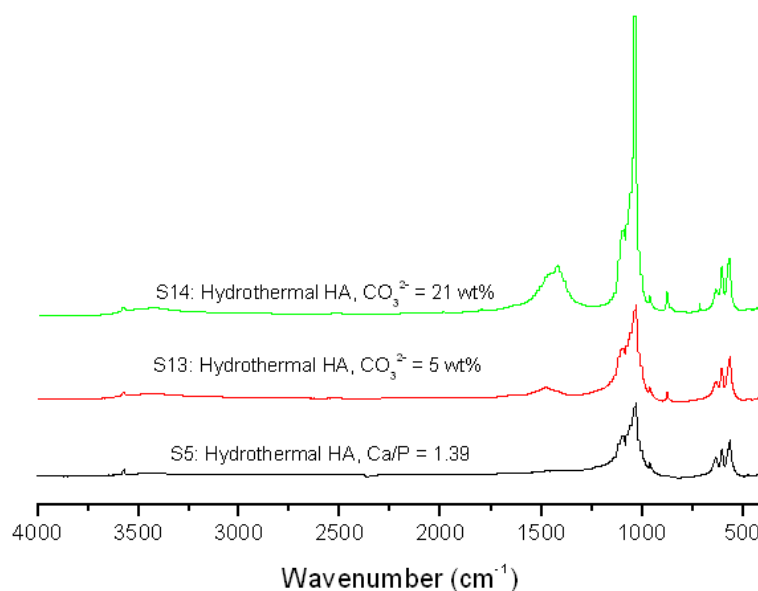
Figure 61: FTIR spectra of three different hydrothermal HA samples: (S5) Ca/P = 1.39, (S13) CO_3^{2-} = 5 wt%, (S14) CO_3^{2-}= 21 wt%.

All samples exhibit the characteristic HA apatite peaks that were mentioned earlier in this work and are shown in Figures 61 and 62.
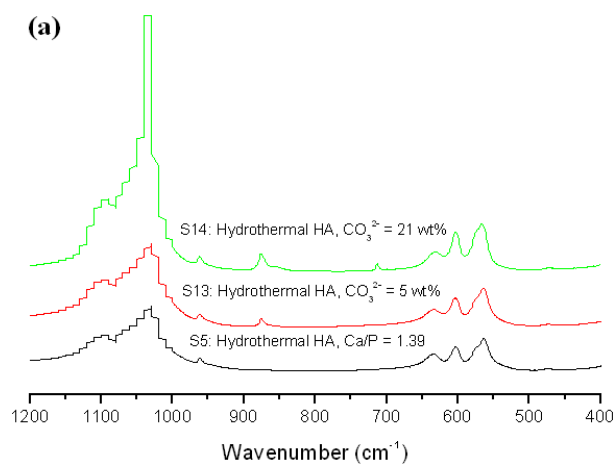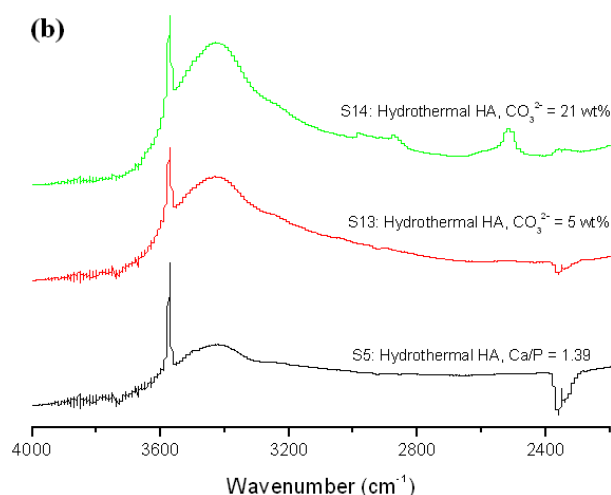
Figure 62: Details of (a) four PO_4^{3-} modes and OH^- libration mode, and (b) OH^- stretching mode of three hydrothermal HA samples: (S5) Ca/P = 1.39, (S13) CO_3^{2-} = 5 wt%, (S14) CO_3^{2-} = 21 wt%.

By increasing CO_3^{2-} substitution up to 21 wt% from S5 to S13 and S14, a slight shift of the main bands for both substituted samples is observed compared to the control sample S5. *Yasukawa and co-workers* observed a similar shift in the FTIR spectra of CO_3-HA samples with increasing the CO_3^{2-} concentration from 0.1 to 0.7 wt% [187]. As shown in Figure 62 (a), in the case of S14, a small band appears at 714 cm^{-1}. A similar peak at 718 cm^{-1} was reported by *E.I. Feki and co-workers* who assigned this peak to the B-type CO_3^{2-} v_4 mode in fluorinated apatite samples [188] whereas *Vagenas and co-workers* reported that the peak at 713 cm^{-1} corresponded most likely to calcite ($CaCO_3$) [189].

The appearance of several additional absorption bands in the region of 900-800 cm^{-1}, and 1600-1400 cm^{-1} as shown in Figure 63 (a) and (b), respectively, suggests that certain amount of CO_3^{2-} substitution has definitely taken place in the apatite lattice structure of both S13 and S14 [114, 190, 191].
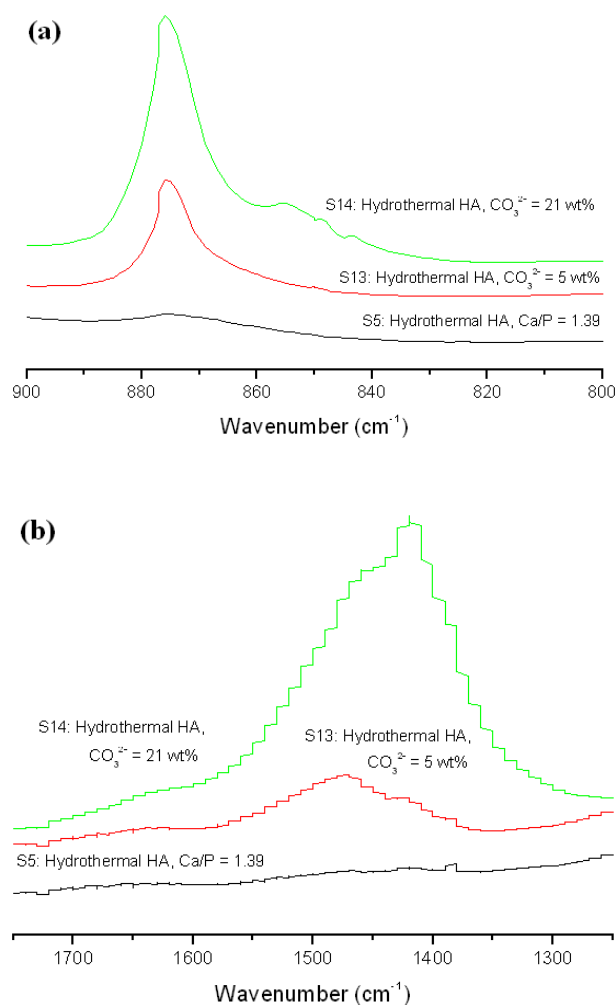
Figure 63: Details of (a) CO_3^{2-} mode v_2, and (b) CO_3^{2-} mode v_3 of three hydrothermal HA samples: (S5) Ca/P = 1.39, (S13) CO_3^{2-} = 5 wt%, (S14) CO_3^{2-} = 21 wt%.

As reported by *Landi and co-workers*, the FTIR bands at 880, 1450, and 1540 cm^{-1} were attributed to the typical A-type CO_3-HA, whereas the bands at 870, 1430, and 1450 cm^{-1} were due to the presence of B-type CO_3^{2-} substitution [179]. In addition, it was also reported that both A-type and B-type CO_3^{2-} substitutions can co-exist in the apatite lattice [179, 180]. This was evidenced by the presence of bands in the region of 877-844 cm^{-1} and 1560-1419 cm^{-1} that correspond to CO_3^{2-} mode v_2, and v_3, respectively [114]. Based on the above, it is clear that both A-type and B-type CO_3^{2-} are present in S13 and S14 as shown in Figure 63 (a) and (b).

Table 29: Peak assignment of FTIR spectra for three hydrothermal HA samples with different CO_3^{2-} substitutions: (S5) Ca/P = 1.39, (S13) CO_3^{2-} = 5 wt%, (S14) CO_3^{2-} = 21 wt%.

S5: Hydrothermal HA, Ca/P = 1.39	S13: Hydrothermal HA, CO_3^{2-} = 5wt%	S14: Hydrothermal HA, CO_3^{2-} = 21wt%	Assignment	Reference
476	476	476	O-P-O bending mode v_2	[36, 156-158]
561-601	563-604	566-603	O-P-O bending mode v_4	[36, 156-158]
634	633	632	OH^- libration mode	[20, 36, 148, 157]
-	-	714	B-type CO_3 vibration mode v_4 / $CaCO_3$	[189]
871	850, 876, 877	844, 849, 855, 876, 877	B-type/ A-type CO_3 vibration mode v_2	[114, 179, 180]
871	876, 877	876, 877	HPO_4^{2-}	[152, 156, 162]
963	961	962	P-O stretching vibration mode v_1	[36, 156-158]
871, 1384	877, 1364-1568	877, ~1378	Residual nitrate	[152, 161]
1029, ~1095	~1030, ~1095	~1036, ~1095	P-O stretching vibration mode v_3	[36, 156-158]
1424-1438	1423, 1477	1345-1580	B-type/ A-type CO_3 vibration mode v_3	[114, 179, 180]
1641, 3424	1650, 3429	1639, 3423	Adsorbed water	[158, 161]
2359	2351	-	CO_2 in air	[106]
3571	3571	3571	OH^- stretching mode	[20, 36, 148, 157]

3.6.3. Raman spectroscopy studies

Figure 64 shows the Raman spectra of three HA samples with different CO_3^{2-} substitutions. The Raman peak positions and their assignments are summarised in Table 30.
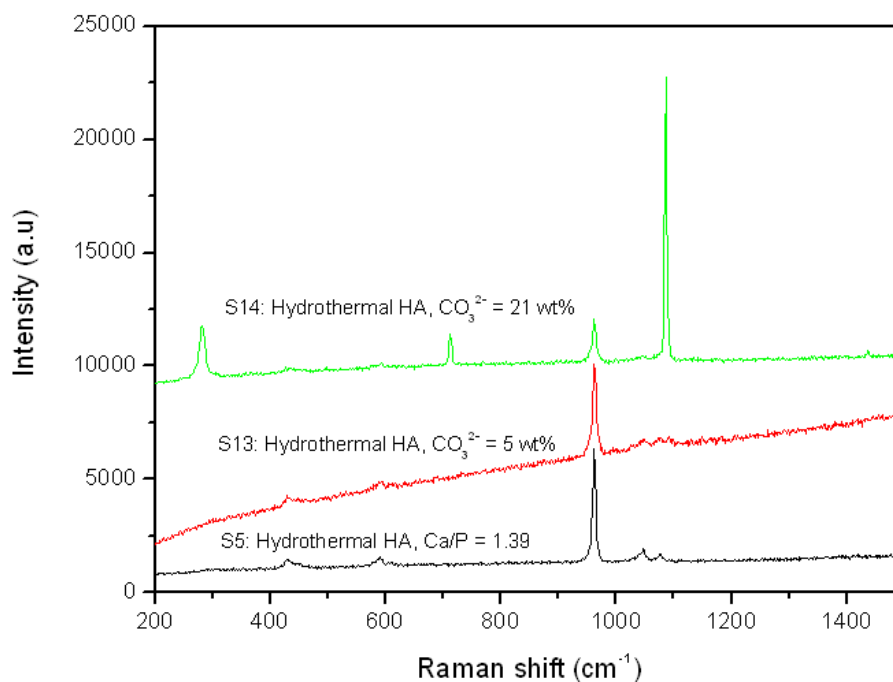
Figure 64: Raman spectra of three hydrothermal HA samples with different CO_3^{2-} substitutions: (S5) Ca/P = 1.39, (S13) CO_3^{2-} = 5 wt%, (S14) CO_3^{2-} = 21 wt%.

The Raman spectrum of S5 has already been described and discussed in paragraph *3.1.3*. In the case of S13 where CO_3^{2-} substitution is 5 wt% not significant changes are observed compared to the S5. The spectrum of S14 however shows 3 additional peaks at 284 cm^{-1} and 1086 cm^{-1} associated with the presence of $CaCO_3$ [192] and at 714 cm^{-1} associated with CO_3^{2-} v_4 mode vibrations [164]. *Penel and co-workers* also referred to a peak at 1076 cm^{-1} that was assigned to both PO_4^{3-} mode v_3 and B-type CO_3^{2-} mode v_1 [121]. It is not clear however, whether in the case of S14 the peak at 1086 cm^{-1} can be assigned to both PO_4^{3-} mode v_3 and B-type CO_3^{2-} mode v_1 vibrations but given that *Li and co-workers* clearly stated that the peak at 1086 cm^{-1} was present in the Raman spectrum of $CaCO_3$ [192], it is most likely that in the case of S14 this peak is associated

with the presence of B-type CO_3^{2-} [164].

De Mul and co-workers proposed an interesting method to determine the concentration of CO_3^{2-} content in the apatite samples, by comparing the Raman peak [82]. Figure 65 shows such a comparison among S5, S13 and S14. It can be concluded, that incorporating CO_3^{2-} into the apatite lattice the intensity of the peak associated with PO_4^{3-} mode v_1 decreases. This is an indication according to *Legeros and co-workers* [124] that by incorporating CO_3^{2-} in the apatite lattice results in more disordered apatite structures. The presence of CO_3^{2-} seems to interfere with the crystallization of apatite as well as it results in weakening effects in the chemical bonds of the apatite structure.
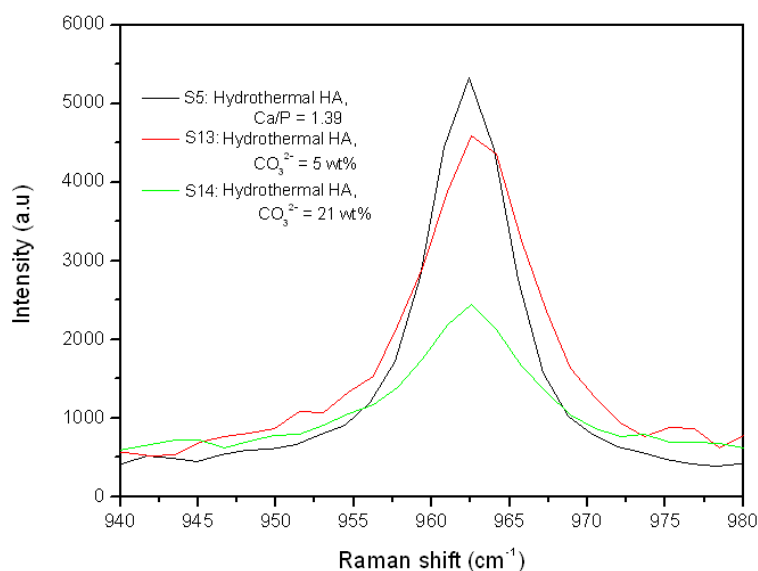
Figure 65: Details of PO_4^{3-} mode v_1 of three HA samples with different CO_3^{2-} substitution.

De Mul and co-workers suggested that the substituting limit of CO_3^{2-} in the apatite structure was approximately 4.5 wt%, and when the CO_3^{2-} content was beyond the substituting limit, the excess amount of CO_3 was located on the apatite crystallite surface with no further effect on the apatite lattice [82]. *Elliott* reported that the excess of CO_3^{2-} content could also be present in the form of amorphous $CaCO_3$ [46]. In the current situation, due to the small change in the peak width of PO_4^{3-} mode v_1 for S13 and S14, it is suggested that in the case of S14, was not complete. It is not possible to

accurately calculate the amount of CO_3^{2-} substitution in S14 based on the current data. However, it can be assumed that the max possible CO_3^{2-} substitution should be between 5 and 21 wt% and most likely closer to 5 wt%. The excess amount of CO_3^{2-} content is most likely adsorbed on the apatite surface or/ and present in amorphous $CaCO_3$ as suggested in the literature [46, 82]. However, in the present situation it was clear from the XRD data that S14 exhibits a crystalline phase of $CaCO_3$ as a secondary phase. The processing temperature during the hydrothermal synthesis was 400^oC higher than the actual crystallisation temperature of $CaCO_3$ at 357^oC as reported by *Koga and co-workers* [193].

Table 30: Peak assignment of Raman spectra for three hydrothermal HA samples with different CO_3^{2-} substitutions: (S5) Ca/P = 1.39, (S13) CO_3^{2-} = 5 wt%, (S14) CO_3^{2-} = 21 wt%.

S5: Hydrothermal HA, Ca/P = 1.39	S13: Hydrothermal HA, CO_3^{2-} = 5wt%	S14: Hydrothermal HA, CO_3^{2-} = 21wt%	Assignment	Reference
428, ~446	431	434	PO_4^{3-} v_2 mode	[10, 121]
~579, 591, ~609	590	593	PO_4^{3-} v_4 mode	[10, 121]
962	963	963	PO_4^{3-} v_1 mode	[10, 121]
1048, 1076	1028, 1046, 1076, 1090	1048, 1086	PO_4^{3-} v_3 mode	[10, 121]
1076	1076	-	B-site CO_3^{2-} mode v_1	[121]
-	-	284, 714, 1086, 1435	$CaCO_3$	[192]

3.6.4. ^{31}P MAS-NMR spectroscopy studies

Figure 66 shows the ^{31}P MAS-NMR spectra of S5, S13 and S14 with different CO_3^{2-} substitutions ranging from 0 to 21 wt%. The ^{31}P chemical shift and peak width at half maximum are listed in Table 31.
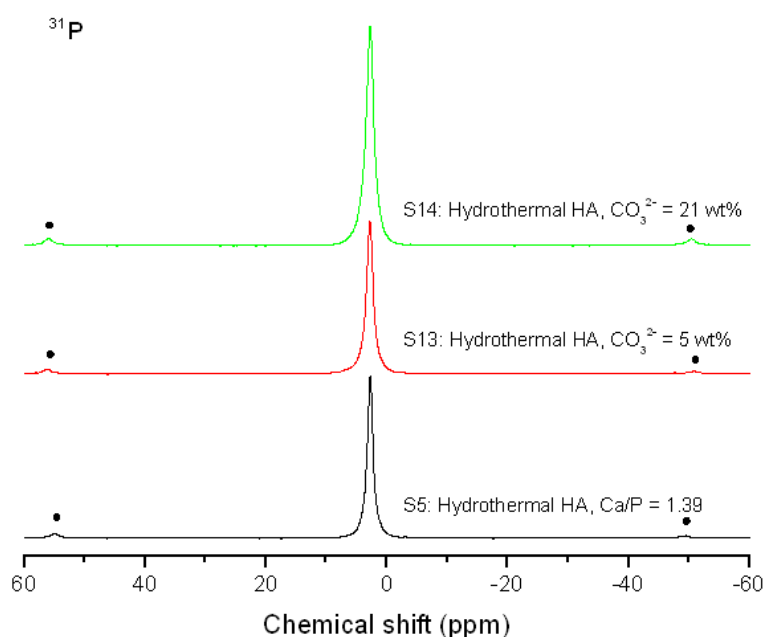
Figure 66: ^{31}P MAS-NMR spectra of three hydrothermal HA samples with different CO_3^{2-} substitutions: (S5) Ca/P = 1.39, (S13) CO_3^{2-} = 5 wt%, (S14) CO_3^{2-} = 21 wt%. The side bands are indicated by •

A single peak at 2.8 ppm is observed in the case of S5 whereas the peak for S13 and S14 shifts to 2.9 and 2.7 ppm, respectively. *Miquel and co-workers* assigned the chemical shift at 2.9 ppm to crystalline stoichiometric apatite structure [168]. The FWHM increases with increasing CO_3^{2-} as shown in Table 31. It is known that the peak broadening in the ^{31}P MAS-NMR spectra is usually accompanied with a reduction in the crystallite size as well as a reduction in the degree of crystallinity [168]. The increased ^{31}P MAS-NMR FWHM (Figure 66) with increasing CO_3^{2-}, suggests a decrease in the crystallite size and crystallinity of the apatite phase in the order of S5 > S13 > S14, which is in good agreement with the XRD results in paragraph *3.6.1* and Table 28. The largest FWHM in the case of S14 is probably due to the following factors: (1) the smallest apatite crystallite size [169]; (2) the poorest degree of crystallinity of

apatite [168], given by the highest amount of CO_3^{2-} in the apatite structure, and possible larger amount of excess CO_3^{2-} segregated at outside of the HA lattice, compared to S13.

Table 31: ^{31}P MAS-NMR chemical shift and peak width at half maximum (FWHM) of three hydrothermal HA samples with different CO_3^{2-} substitutions: (S5) Ca/P = 1.39, (S13) CO_3^{2-} = 5 wt%, (S14) CO_3^{2-} = 21 wt%.

Sample	Description	Chemical shift (ppm)	FWHM (ppm)
S5	Hydrothermal HA, Ca/P = 1.39	2.8	1.11
S13	Hydrothermal HA, CO_3^{2-} = 5 wt%	2.9	1.20
S14	Hydrothermal HA, CO_3^{2-} = 21 wt%	2.7	1.26

4. Conclusions

Effect of synthesis on the apatite structure

HA and substituted HA have been successfully prepared by using three different preparation methods; chemical precipitation method, bacterial biosynthesis, and hydrothermal method.

The formation of HA has been confirmed by the presence of the characteristic HA XRD pattern in all samples as well as by ^{31}P MAS-NMR spectroscopy that showed the presence of phosphorus in an orthophosphate environment in the region between 2.7-3.3 ppm. However, due to the variation of the peak width and/ or peak intensity in the XRD patterns and ^{31}P MAS-NMR spectra, there were changes in the crystallite size and the degree of crystallinity among the different samples studied. Comparing the HA samples prepared by different synthesis methods it was concluded, that the crystallite size ranged from 8 to 42 nm in the order:

S20 (biological HA) < S15 (precipitated HA) < S6 (hydrothermal HA, Ca/P = 1.42) < S5 (hydrothermal HA, Ca/P = 1.39)

The crystallite size and crystallinity are highly dependent on the processing parameters, such as temperature, time, and pH. From the FTIR and Raman studies, the changes in the crystallite size as well as the degree of the crystallinity of the HA samples were attributed to the presence of other foreign ions, such as CO_3^{2-}, HPO_4^{2-}, and/or residual nitrates (the latter is only true for the hydrothermal and precipitated HA samples).

All HA samples seem to contain both A-type and B-type CO_3^{2-}. Considering that no CO_3^{2-} source was applied during the synthesis with the exception of the biological HA, the presence of CO_3^{2-} in the HA samples, was attributed to the following reasons: (1) the presence of impurities in the starting materials; (2) the experimental steps were carried out in air.

Effect of ionic substitution on the apatite structure

In this project, the effect of five different substitutions, Zn^{2+}, Mg^{2+}, Sr^{2+}, Si/SiO_4^{4-}, and CO_3^{2-} were studied. Depending on the different size of substituted ions, as well as the degree of substitution, different results were obtained. Some of the substituted ions were actually integrated in the apatite lattice but some were either adsorbed on the surface of apatite crystals or present in other secondary phases or amorphous regions. Substitutions in the apatite lattice do not seem to be always unlimited. For some ions it was clear that only a small amount was able to become part of the apatite lattice. Generally, ionic substitution had a significant effect on the crystallite size, crystallinity and lattice parameters.

Effect of Zn^{2+} substitution in hydrothermal HA

There was only one sample with 2.6 wt% Zn^{2+} substitution (S7) that was compared with the control hydrothermal HA (Ca/P = 1.39). Generally, there was no strong evidence that Zn^{2+} was part of the apatite lattice. Not significant changes in the crystallite size or crystallinity were observed and the XRD pattern as well as the FTIR and Raman spectra did not show any indication that there was a strong effect of Zn^{2+} substitution on the apatite structure. Raman spectra showed a small decrease in the crystallinity of S7 which was attributed to the presence of B-type CO_3^{2-} ions, adsorbed water molecules, as well as residual nitrate groups, which were identified in the FTIR spectra. Generally, there are two reasons for the above observations: (1) the substitution of 2.6 wt% Zn is too small to induce any obvious changes in the apatite structure; (2) Zn might not have entered the apatite lattice at all, or at least not all of it, and instead, it was adsorbed on the crystallite surface or/ and present in the amorphous phase.

Effect of Mg^{2+} substitution in hydrothermal HA

Four hydrothermal Mg-containing samples with Mg substitution ranging from 0.7 to 9.1 wt% (S1-S4) were compared with a control hydrothermal HA (Ca/P = 1.39) sample. Generally, incorporation of 0.7 wt% Mg substitution (S1) was accepted in the HA

structure without showing strong effects on the apatite structure. However, the increasing Mg substitution from 1.6 to 9.1 wt% resulted in inhibiting the formation of apatite and favouring the formation of Mg-whitlockite. The crystallite size and the crystallinity of apatite and/ or Mg-whitlockite were varied, and that was most likely due to the presence of un-quantified amount of B-type CO_3^{2-}, residual nitrates, and HPO_4^{2-}, as well as associated with increased Mg substitution.

Effect of Sr^{2+} in precipitated HA

The effect of Sr^{2+} substitution from 0 to 100 mol% (S15-S19) in precipitated apatite structure was studied. Unlike the effect of Mg^{2+}, Sr^{2+} substituted easily Ca in the apatite lattice. Rietveld analysis suggested that the incorporation of 25 mol% Sr (S16) into precipitated HA expanded both the lattice parameters *a* and *c*. By increasing Sr substitution from 0 to 100 mol%, the crystallite size varied from 10 to 22 nm, and the smallest crystallite size was obtained when 50 mol% substitution occurred (S17), whereas the largest crystallite size was observed in the fully Sr substituted apatite sample (S19). Both FTIR and Raman analysis suggested that CO_3^{2-} was present in all precipitated apatite samples, whereas the FTIR spectra additionally indicated that there were residual nitrates and possibly a small fraction of HPO_4^{2-} as well. Furthermore, the Raman peak at around 1772 cm^{-1} was only observed in the Sr containing apatite samples suggested that this peak most likely derived from the chemical reactant of $Sr(NO_3)_2$.

Effect of Si/SiO_4^{4-} in hydrothermal HA

Four hydrothermal HA samples with various Si substitutions from 0.26 to 0.81 wt% (S8-S12) were compared with the control hydrothermal HA (Ca/P = 1.39) sample. In general, there was no obvious indication for the incorporation of Si into the HA structure. Therefore, it was considered that either the Si substitution was not entering in the apatite lattice at all, or the Si substitution concentration 0.81 wt% was too small to cause any effect on the structure of the apatite. On the other hand the crystallite size, crystallinity and the lattice parameters were found to vary randomly with increasing Si substitution.

Effect of CO$_3{}^{2-}$ in hydrothermal HA

Two hydrothermal CO$_3{}^{2-}$ substituted HA samples (S13-S14) with CO$_3{}^{2-}$ substitution of 5-21 wt% were studied and compared with the control hydrothermal HA (Ca/P = 1.39). The CO$_3{}^{2-}$ substituting limit should be within the range between 5 and 21 wt% in the apatite structure. Above 21 wt% substitution the formation of secondary phase of CaCO$_3$ in addition to HA was observed (S14). The presence of increased CO$_3{}^{2-}$ substitution from 0 to 21 wt% in the HA samples led to the reduction in the HA crystallite size from 42 to 16 nm. FTIR and Raman studies both confirmed that the presence of CO$_3{}^{2-}$ species. In addition, both XRD and Raman results suggested that the crystallite size and crystallinity were different for each sample due to the presence of CO$_3{}^{2-}$, residual nitrates, and possibly HPO$_4{}^{2-}$.

5. References

[1]   W. Suchanek and M. Yoshimura, "Processing and properties of hydroxyapatite-based biomaterials for use as hard tissue replacement implants," *Journal of Materials Research,* vol. 13, pp. 94-117 1998.

[2]   M. Vallet-Regí and J. M. González-Calbet, "Calcium phosphates as substitution of bone tissues," *Progress in Solid State Chemistry,* vol. 32, pp. 1-31, 2004.

[3]   M. C. Kuo and S. K. Yen, "The process of electrochemical deposited hydroxyapatite coatings on biomedical titanium at room temperature," *Materials Science and Engineering: C,* vol. 20, pp. 153-160, 2002.

[4]   T. J. Webster, C. Ergun, R. H. Doremus, R. W. Siegel, and R. Bizios, "Enhanced functions of osteoblasts on nanophase ceramics," *Biomaterials,* vol. 21, pp. 1803-1810, 2000.

[5]   T. J. Webster, C. Ergun, R. H. Doremus, R. W. Siegel, and R. Bizios, "Enhanced osteoclast-like cell functions on nanophase ceramics," *Biomaterials,* vol. 22, pp. 1327-1333, 2001.

[6]   S. Bose and S. K. Saha, "Synthesis of hydroxyapatite nanopowders via sucrose-templated sol-gel method," *Journal of the American Ceramic Society,* vol. 86, pp. 1055-1057, 2003.

[7]   J. L. Xu, K. A. Khor, Z. L. Dong, Y. W. Gu, R. Kumar, and P. Cheang, "Preparation and characterization of nano-sized hydroxyapatite powders produced in a radio frequency (rf) thermal plasma," *Materials Science and Engineering A,* vol. 374, pp. 101-108, 2004.

[8]   H. Suda, M. Yashima, M. Kakihana, and M. Yoshimura, "Monoclinic ↔ hexagonal phase transition in hydroxyapatite studied by X-ray powder

diffraction and differential scanning calorimeter techniques," *The Journal of Physical Chemistry,* vol. 99, pp. 6752-6754, 2002.

[9]   S.-H. Rhee, "Synthesis of hydroxyapatite via mechanochemical treatment," *Biomaterials,* vol. 23, pp. 1147-1152, 2002.

[10]   C. C. Silva, A. G. Pinheiro, M. A. R. Miranda, J. C. Góes, and A. S. B. Sombra, "Structural properties of hydroxyapatite obtained by mechanosynthesis," *Solid State Sciences,* vol. 5, pp. 553-558, 2003.

[11]   R. L. Stephen, H. C. Philip, A. M. Eugene, and A. C. Robert, "Forming method for apatite prostheses," *Journal of Biomedical Materials Research,* vol. 3, pp. 683-684, 1969.

[12]   X. Zhang and K. S. Vecchio, "Hydrothermal synthesis of hydroxyapatite rods," *Journal of Crystal Growth,* vol. 308, pp. 133-140, 2007.

[13]   J. Liu, X. Ye, H. Wang, M. Zhu, B. Wang, and H. Yan, "The influence of pH and temperature on the morphology of hydroxyapatite synthesized by hydrothermal method," *Ceramics International,* vol. 29, pp. 629-633, 2003.

[14]   C. R. Kothapalli, M. Wei, R. Z. Legeros, and M. T. Shaw, "Influence of temperature and aging time on HA synthesized by the hydrothermal method," *Journal of Materials Science: Materials in Medicine,* vol. 16, pp. 441-446, 2005.

[15]   A. A. Chaudhry, S. Haque, S. Kellici, P. Boldrin, I. Rehman, F. A. Khalid, and J. A. Darr, "Instant nano-hydroxyapatite: a continuous and rapid hydrothermal synthesis," *Chemical Communications,* vol. 21, pp. 2286-2288, 2006.

[16]   A. Jillavenkatesa and R. A. Condrate Sr, "Sol–gel processing of hydroxyapatite," *Journal of Materials Science,* vol. 33, pp. 4111-4119, 1998.

[17]   D. L. Shi and X. J. Wen, "Bioactive ceramics: structure, synthesis, and

mechanical properties," in *Introduction to biomaterials*, D. L. Shi, Ed.: Tsinghua University Press, 2006, pp. 16-17.

[18] N. Asaoka, S. Best, J. C. Knowles, and W. Bonfield, "Characterisation of hydroxyapatite precipitated from different reactants," in *Proceedings of the eighth international symposium on ceramics in medecine*, Ponte Vedra, Florida, 1995, pp. 331-337.

[19] M. H. Santos, M. d. Oliveira, L. P. d. F. Souza, H. S. Mansur, and W. L. Vasconcelos, "Synthesis control and characterization of hydroxyapatite prepared by wet precipitation process," *Materials Research,* vol. 7, pp. 625-630, 2004.

[20] A. Bigi, E. Boanini, C. Capuccini, and M. Gazzano, "Strontium-substituted hydroxyapatite nanocrystals," *Inorganica Chimica Acta,* vol. 360, pp. 1009-1016, 2007.

[21] M.-F. Hsieh, L.-H. Perng, T.-S. Chin, and H.-G. Perng, "Phase purity of sol-gel-derived hydroxyapatite ceramic," *Biomaterials,* vol. 22, pp. 2601-2607, 2001.

[22] Y. Masuda, K. Matubara, and S. Sakka, "Synthesis of hydroxyapatite from metal alkoxides through sol-gel technique," *Journal of the Ceramic Society of Japan,* vol. 98, pp. 1266-1277, 1990.

[23] H. Takahashi, M. Yashima, M. Kakihana, and M. Yoshimura, "Synthesis of stoichiometric hydroxyapatite by a gel route from the aqueous solution of citric and phosphonoacetic acids," *European Journal of Solid State and Inorganic Chemistry,* vol. 32, pp. 829-835, 1995.

[24] I.-S. Kim and P. N. Kumta, "Sol-gel synthesis and characterization of nanostructured hydroxyapatite powder," *Materials Science and Engineering B,*

vol. 111, pp. 232-236, 2004.

[25]   P. Yong, L. E. Macaskie, R. l. Sammons, and P. M. Marquis, "Synthesis of nanophase hydroxyapatite by a Serratia sp. from waste-water containing inorganic phosphate," *Biotechnology Letters,* vol. 26, pp. 1723-1730, 2004.

[26]   S. Bagheriasl, "The production and characterisation of PHB and HA from high and low phosphatise activity Serratia. sp cells," in *Department of Metallurgy and Materials*. vol. MRes in Biomaterials Birmingham: Univeristy of Birmingham, 2008, pp. 1-70.

[27]   L. L. Hench, "Bioceramics: from concept to clinic," *Journal of the American Ceramic Society,* vol. 74, pp. 1487-1510, 1991.

[28]   R. A. Laudise, *The growth of single crystals*. New York: Prentice Hall, 1970.

[29]   S. Koutsopoulos, "Synthesis and characterization of hydroxyapatite crystals: a review study on the analytical methods," *Journal of Biomedical Materials Research,* vol. 62, pp. 600-612, 2002.

[30]   J. C. Heughebaert, S. J. Zawacki, and G. H. Nancollas, "The growth of nonstoichiometric apatite from aqueous solution at 37°C : I. Methology and growth at pH 7.4," *Journal of Colloid and Interface Science,* vol. 135, pp. 20-32, 1990.

[31]   S. J. Zawacki, J. C. Heughebaert, and G. H. Nancollas, "The growth of nonstoichiometric apatite from aqueous solution at 37°C : II. Effects of pH upon the precipated phase," *Journal of Colloid and Interface Science,* vol. 135, pp. 33-44, 1990.

[32]   V. Hlady and H. Füredi-Milhofer, "Adsorption of human serum albumin on precipitated hydroxyapatite," *Journal of Colloid and Interface Science,* vol. 69, pp. 460-468, 1979.

[33]   C. Kothapalli, M. Wei, A. Vasiliev, and M. T. Shaw, "Influence of temperature and concentration on the sintering behavior and mechanical properties of hydroxyapatite," *Acta Materialia,* vol. 52, pp. 5655-5663, 2004.

[34]   F. Yoshinobu, Y. Hiroshi, K. Kunio, S. Tsugio, and O. Akitsugu, "Preparation of needle-like hydroxyapatite by homogeneous precipitation under hydrothermal conditions," *Journal of Chemical Technology & Biotechnology,* vol. 57, pp. 349-353, 1993.

[35]   I. Neira, F. Guitián, T. Taniguchi, T. Watanabe, and M. Yoshimura, "Hydrothermal synthesis of hydroxyapatite whiskers with sharp faceted hexagonal morphology," *Journal of Materials Science,* vol. 43, pp. 2171-2178, 2008.

[36]   K. H. Prakash, C. P. Ooi, R. Kumar, K. A. Khor, and P. Cheang, "Effect of super saturation level on the size and morphology of hydroxyapatite precipitate," 2006.

[37]   K. M. Bonthrone, J. Quarmby, C. J. Hewitt, V. J. M. Allan, M. Paterson-Beedle, J. F. Kennedy, and L. E. Macaskie, "The effect of the growth medium on the composition and metal binding behaviour of the extracellular polymeric material of a metal-accumulating Citrobacter sp," *Environmental Technology,* vol. 21, pp. 123 -134, 2000.

[38]   L. E. Macaskie, K. M. Bonthrone, P. Yong, and D. T. Goddard, "Enzymically mediated bioprecipitation of uranium by a Citrobacter sp.: a concerted role for exocellular lipopolysaccharide and associated phosphatase in biomineral formation," *Microbiology,* vol. 146, pp. 1855-1867, August 1, 2000 2000.

[39]   J. A. Dean, *Lange's handbook of chemistry,* 14th edition ed. New York McGraw-Hill, 1992.

[40] A. S. Posner, A. Perloff, and A. F. Diorio, "Refinement of the hydroxyapatite structure," *Acta Crystallographica,* vol. 11, pp. 308-309, 1958.

[41] X. Ma and D. E. Ellis, "Initial stages of hydration and Zn substitution/occupation on hydroxyapatite (0001) surfaces," *Biomaterials,* vol. 29, pp. 257-265, 2008.

[42] L. Calderín, M. J. Stott, and A. Rubio, "Electronic and crystallographic structure of apatites," *Physical Review B,* vol. 67, p. 134106, 2003.

[43] J. C. Elliott, *Structure and chemistry of the apatites and other calcium orthophosphates*. Amsterdam: Elsevier, 1994.

[44] J. C. Elliott, R. M. Wilson, and S. E. P. Dowker, *JCPDS-international centre for diffraction data,* vol. 45, pp. 172-181, 2002.

[45] J. M. Hughes and J. Rakovan, "The crystal structure of apatite, $Ca_5(PO_4)_3(F,OH,Cl)$," *Reviews in Mineralogy and Geochemistry,* vol. 48, pp. 1-12, 2002.

[46] J. C. Elliott, "Recent progress in the chemistry, crystal chemistry and structure of the apatites," *Calcified Tissue International,* vol. 3, pp. 293-307, 1969.

[47] C. A. Beevers and B. McIntyre, "The atomic structure of fluor-apatite and its relation to that of tooth and bone material," *Mineralogical Magazine,* vol. 27, pp. 254-257, 1946.

[48] R. A. Young, *Trans. N.Y. Acad. Sci. Ser,* vol. 29, pp. 949-959, 1967.

[49] M. I. Kay, R. A. Young, and A. S. Posner, "Crystal structure of hydroxyapatite," *Nature,* vol. 204, pp. 1050-1052, 1964.

[50] D. Arcos, J. Rodríguez-Carvajal, and M. Vallet-Regí, "Neutron scattering for the study of improved bone implants," *Physica B: Condensed Matter,* vol. 350, pp. E607-E610, 2004.

[51] R. A. Young and J. C. Elliott, "Atomic-scale bases for several properties of apatites," *Archives of Oral Biology,* vol. 11, pp. 699-707, 1966.

[52] T. Ikoma, A. Yamazaki, S. Nakamura, and M. Akao, "Preparation and structure refinement of monoclinic hydroxyapatite," *Journal of Solid State Chemistry,* vol. 144, pp. 272-276, 1999.

[53] J. C. Elliott, P. E. Mackie, and R. A. Young, "Monoclinic hydroxyapatite," *Science,* vol. 180, pp. 1055-1057, June 8, 1973 1973.

[54] K. Sudarsanan, P. E. Mackie, and R. A. Young, "Comparison of synthetic and mineral fluorapatite, $Ca_5 (PO_4)_3F$, in crystallographic detail," *Materials Research Bulletin,* vol. 7, pp. 1331-1337, 1972.

[55] H. B. Van Rees, M. Mengeot, and E. Kostiner, "Monoclinic-hexagonal transition in hydroxyapatite and deuterohydroxyapatite single crystals," *Materials Research Bulletin,* vol. 8, pp. 1307-1310, 1973.

[56] U. Heise, J. F. Osborn, and F. Duwe, "Hydroxyapatite ceramic as a bone substitute," *International Orthopaedics,* vol. 14, pp. 329-338, 1990.

[57] I. Khairoun, M. G. Boltong, F. C. M. Driessens, and J. A. Planell, "Limited compliance of some apatitic calcium phosphate bone cements with clinical requirements," *Journal of Materials Science: Materials in Medicine,* vol. 9, pp. 667-671, 1998.

[58] S. H. Zhu, B. Y. Huang, K. C. Zhou, S. P. Huang, F. Liu, Y. M. Li, Z. G. Xue, and Z. G. Long, "Hydroxyapatite nanoparticles as a novel gene carrier," *Journal of Nanoparticle Research,* vol. 6, pp. 307-311, 2004.

[59] C. Verwilghen, S. Rio, A. Nzihou, D. Gauthier, G. Flamant, and P. J. Sharrock, "Preparation of high specific surface area hydroxyapatite for environmental applications," *Journal of Materials Science,* vol. 42, pp. 6062-6066, 2007.

[60] S. Bailliez, A. Nzihou, E. Beche, and G. Flamant, *Process Safety and Environmental Protection,* vol. 82, p. 175, 2004.

[61] X. Chen, J. V. Wright, J. L. Conca, and L. M. Peurrung, *Environmental Science and Technology,* vol. 31, p. 624, 1997.

[62] N. C. Da Rocha, R. C. De Campos, A. M. Rossi, E. L. Moreira, F. Barbosa, and G. T. Moure, *Environmental Science and Technology* vol. 36, p. 1630, 2002.

[63] M. J. Phillips, J. A. Darr, Z. B. Luklinska, and I. Rehman, "Synthesis and characterization of nano-biomaterials with potential osteological applications," *Journal of Materials Science: Materials in Medicine,* vol. 14, pp. 875-882, 2003.

[64] K. D. Rogers and P. Zioupos, "The bone tissue of the rostrum of a mesoplodon densirostris whale: a mammalian biomineral demonstrating extreme texture," *Journal of Materials Science Letters,* vol. 18, pp. 651-654, 1999.

[65] M. A. Meyers, P.-Y. Chen, A. Y.-M. Lin, and Y. Seki, "Biological materials: structure and mechanical properties," *Progress in Materials Science,* vol. 53, pp. 1-206, 2008.

[66] S. Weiner and H. D. Wagner, "The material bone: structure-mechanical function relations," *Annual Review of Materials Science,* vol. 28, pp. 271-298, 1998.

[67] J. D. Pasteris, B. Wopenka, and E. Valsami-Jones, "Bone and tooth mineralization: why apatite?," *Elements,* vol. 4, pp. 97-104, 2008.

[68] S. V. Dorozhkin and E. Matthias, "Biological and medical significance of calcium phosphates," *Angewandte Chemie International Edition,* vol. 41, pp. 3130-3146, 2002.

[69] R. B. Martin and D. B. Burr, *The structure, function and adaptation of cortical bone*. New York Raven Press, 1989.

[70] A. L. Boskey, "Mineralization of bones and teeth," *Elements,* vol. 3, pp. 385-391, 2007.

[71] J. L. William, J. H. Karen, A. James, S. Min Ja, and F. M. Bruce, "Structural relations between collagen and mineral in bone as determined by high voltage electron microscopic tomography," *Microscopy Research and Technique,* vol. 33, pp. 192-202, 1996.

[72] P. Fratzl, N. Fratzl-Zelman, K. Klaushofer, G. Vogl, and K. Koller, "Nucleation and growth of mineral crystals in bone studied by small-angle X-ray scattering," *Calcified Tissue International,* vol. 48, pp. 407-413, 1991.

[73] N. E. Waters, "Some mechanical and physical properties of teeth," *Symposia of the Society for Experimental Biology,* vol. 34, pp. 99-135, 1980.

[74] M. L. Snead, Z. Danhong, Y. Lei, S. N. White, C. M. Snead, L. Wen, and M. L. Paine, "Protein self-assembly creates a nanoscale device for biomineralization," *Materials Science and Engineering: C,* vol. 26, pp. 1296-1300, 1999.

[75] R. Z. LeGeros, *Hydroxyapatite and related materials*. Boca Raton: CRC Press, 1994.

[76] V. Imbeni, R. K. Nalla, C. Bosi, J. H. Kinney, and R. O. Ritchie, "In vitro fracture toughness of human dentin," *Journal of Biomedical Materials Research Part A,* vol. 66A, pp. 1-9, 2003.

[77] R. K. Nalla, J. J. Kruzic, J. H. Kirmey, M. Balooch, J. W. Ager, and R. O. Ritchie, "Role of microstructure in the aging-related deterioration of the toughness of human cortical bone," *Materials Science and Engineering: C,* vol. 26, pp. 1251-1260, 1999.

[78] A. S. Posner, "Crystal chemistry of bone mineral," *Physiological Reviews,* vol. 49, pp. 760-792, 1969.

[79] R. A. Harper and A. S. Posner, "Measurement of non-crystalline calcium phosphate in bone mineral," *Proceedings of the Society for Experimental Biology and Medicine,* vol. 122, pp. 137-142, 1966.

[80] J. D. Termine and A. S. Posner, "Amorphous/crystalline interrelationships in bone mineral," *Calcified Tissue International,* vol. 1, pp. 8-23, 1967.

[81] M. Mathew and S. Takagi, "Structures of biological minerals in dental research," *Journal of Research of the National Institute of Standards and Technology,* vol. 106, pp. 1035-1044, 2001.

[82] F. F. M. De Mul, M. H. J. Hottenhuis, P. Bouter, J. Greve, J. Arends, and J. J. Ten Bosch, "Micro-Raman line broadening in synthetic carbonated hydroxyapatite," *Journal of Dental Research,* vol. 65, pp. 437-440, 1986.

[83] R. Z. LeGeros, *Calcium phosphates in oral biology and medicine*. Basel: Karger, 1991.

[84] G. Daculsi, J. M. Bouler, R. Z. LeGeros, and W. J. Kwang, "Adaptive crystal formation in normal and pathological calcifications in synthetic calcium phosphate and related biomaterials," *International Review of Cytology,* vol. 172, pp. 129-191, 1997.

[85] H. C. W. Skinner, "Biominerals," *Mineralogical Magazine* vol. 69, pp. 621-641, 2005.

[86] N. K. Tripathy, P. N. Patel, and A. Panda, "Preparation, IR, and lattice constant measurements of mixed (Ca + Cu + Zn) hydroxylapatites," *Journal of Solid State Chemistry,* vol. 80, pp. 1-5, 1989.

[87] A. Bigi, E. Foresti, M. Gandolfi, M. Gazzano, and N. Roveri, "Inhibiting effect of zinc on hydroxylapatite crystallization," *Journal of Inorganic Biochemistry,* vol. 58, pp. 49-58, 1995.

[88]   F. Miyaji, Y. Kono, and Y. Suyama, "Formation and structure of zinc-substituted calcium hydroxyapatite," *Materials Research Bulletin,* vol. 40, pp. 209-220, 2005.

[89]   M. O. Li, X. Xiao, R. Liu, C. Chen, and L. Huang, "Structural characterization of zinc-substituted hydroxyapatite prepared by hydrothermal method," *Journal of Materials Science: Materials in Medicine,* vol. 19, pp. 797-803, 2008.

[90]   S. V. Chiranjeevirao, J. Hemmerle, J. C. Voegel, and R. M. Frank, "A method of preparation and characterization of magnesium-apatites," *Inorganica Chimica Acta,* vol. 67, pp. 183-187, 1982.

[91]   P. N. Patel, "Magnesium calcium hydroxylapatite solid solutions: preparation, IR and lattice constant measurements," *Journal of Inorganic and Nuclear Chemistry,* vol. 42, pp. 1129-1132, 1980.

[92]   A. Bigi, G. Falini, E. Foresti, A. Ripamonti, M. Gazzano, and N. Roveri, "Magnesium influence on hydroxyapatite crystallization," *Journal of Inorganic Biochemistry,* vol. 49, pp. 69-78, 1993.

[93]   A. Yasukawa, S. Ouchi, K. Kandori, and T. Ishikawa, "Preparation and characterization of magnesium-calcium hydroxyapatites," *Journal of Materials Chemistry,* vol. 6, pp. 1401-1405, 1996.

[94]   I. V. Fadeev, L. I. Shvorneva, S. M. Barinov, and V. P. Orlovskii, "Synthesis and structure of magnesium-substituted hydroxyapatite," *Inorganic Materials,* vol. 39, pp. 947-950, 2003.

[95]   M. D. O'Donnell, Y. Fredholm, A. de Rouffignac, and R. G. Hill, "Structural analysis of a series of strontium-substituted apatites," *Acta Biomaterialia,* vol. 4, pp. 1455-1464, 2008.

[96]   I. R. Gibson, S. M. Best, and W. Bonfield, "Chemical characterization of

silicon-substituted hydroxyapatite," *Journal of Biomedical Materials Research,* vol. 44, pp. 422-428, 1999.

[97]   X. L. Tang, X. F. Xiao, and R. F. Liu, "Structural characterization of silicon-substituted hydroxyapatite synthesized by a hydrothermal method," *Materials Letters,* vol. 59, pp. 3841-3846, 2005.

[98]   E. Fujii, K. Kawabata, K. Ando, K. Tsuru, S. Hayakawa, and A. Osaka, "Synthesis and structural characterization of silica-hybridized hydroxyapatite with gas adsorption capability," *Journal of the Ceramic Society of Japan,* vol. 114, pp. 769-773, 2006.

[99]   A. R. Stéphane, N. Michel, B.-A. Didier, R. Christian, D. Philippe, S. Laurent, and J. M. Pierre, "Behavior of human osteoblastic cells on stoichiometric hydroxyapatite and type A carbonate apatite: Role of surface energy," *Journal of Biomedical Materials Research,* vol. 50, pp. 353-364, 2000.

[100] T. S. Sampath Kumar, I. Manjubala, and J. Gunasekaran, "Synthesis of carbonated calcium phosphate ceramics using microwave irradiation," *Biomaterials,* vol. 21, pp. 1623-1629, 2000.

[101] D. G. Nelson and J. D. Featherstone, "Preparation, analysis, and characterization of carbonated apatites," *Calcified Tissue International,* vol. 34 Suppl 2, pp. S69-81, 1982.

[102] M. Vignoles, G. Bonel, and R. Young, "Occurrence of nitrogenous species in precipitated B-type carbonated hydroxyapatites," *Calcified Tissue International,* vol. 40, pp. 64-70, 1987.

[103] J. Barralet, S. Best, and W. Bonfield, "Carbonate substitution in precipitated hydroxyapatite: an investigation into the effects of reaction temperature and bicarbonate ion concentration," *Journal of Biomedical Materials Research,* vol.

41, pp. 79-86, 1998.

[104] K. Haruo, I. Atsuo, M. Shunpei, L. Pierre, O. Kenji, I. Noboru, and T. Tetsuya, "Stimulatory effect of zinc-releasing calcium phosphate implant on bone formation in rabbit femora," *Journal of Biomedical Materials Research,* vol. 50, pp. 184-190, 2000.

[105] A. Grandjean-Laquerriere, P. Laquerriere, E. Jallot, J.-M. Nedelec, M. Guenounou, D. Laurent-Maquin, and T. M. Phillips, "Influence of the zinc concentration of sol-gel derived zinc substituted hydroxyapatite on cytokine production by human monocytes in vitro," *Biomaterials,* vol. 27, pp. 3195-3200, 2006.

[106] W. L. Suchanek, K. Byrappa, P. Shuk, R. E. Riman, V. F. Janas, and K. S. TenHuisen, "Preparation of magnesium-substituted hydroxyapatite powders by the mechanochemical-hydrothermal method," *Biomaterials,* vol. 25, pp. 4647-4657, 2004.

[107] W. Bonfield and I. R. Gibson, "Process for the preparation of magnisum and carbonate substituted hydroxyapatite," 1999.

[108] G. Dolci, R. Mongiorgi, R. Rrati, and G. Valdre, "Odontostomatologic use of apatite-based nanostructured materials," 1998.

[109] P. Meunier, C. Roux, E. Seeman, S. Ortolani, J. E. Badurski, T. D. Spector, J. Cannata, A. Balogh, E. M. Lemmel, S. Pors-Nielsen, R. Rizzoli, H. K. Genant, and J. Y. Reginster, "The effects of strontium ranelate on the risk of vertebral fracture in women with postmenopausal osteoporosis," *New England Journal of Medicine,* vol. 350, pp. 459-468, 2004.

[110] E. S. Thian, J. Huang, S. M. Best, Z. H. Barber, and W. Bonfield, "Silicon-substituted hydroxyapatite: the next generation of bioactive coatings,"

Materials Science and Engineering: C, vol. 27, pp. 251-256, 2007.

[111] A. E. Porter, N. Patel, J. N. Skepper, S. M. Best, and W. Bonfield, "Comparison of in vivo dissolution processes in hydroxyapatite and silicon-substituted hydroxyapatite bioceramics," *Biomaterials,* vol. 24, pp. 4609-4620, 2003.

[112] G. Gasquères, C. Bonhomme, J. Maquet, F. Babonneau, S. Hayakawa, T. Kanaya, and A. Osaka, "Revisiting silicate substituted hydroxyapatite by solid-state NMR," *Magnetic Resonance in Chemistry,* vol. 46, pp. 342-346, 2008.

[113] L. Yanbao, L. Dongxu, and W. Wenjian, "Preparation of nano carbonate-substituted hydroxyapatite from an amorphous precursor," *International Journal of Applied Ceramic Technology,* vol. 5, pp. 442-448, 2008.

[114] I. R. Gibson and W. Bonfield, "Novel synthesis and characterization of an AB-type carbonate-substituted hydroxyapatite," *Journal of Biomedical Materials Research,* vol. 59, pp. 697-708, 2002.

[115] R. Z. Legeros and J. P. Legeros, "Dense hydroxyapatite," in *An introduction to bioceramics*, L. L. Hench and J. Wilson, Eds. Singapore: World Scientific, 1993.

[116] E. E. Berry, "The structure and composition of some calcium-deficient apatites," *Journal of Inorganic and Nuclear Chemistry,* vol. 29, pp. 317-327, 1967.

[117] T. S. B. Narasaraju and D. E. Phebe, "Some physico-chemical aspects of hydroxylapatite," *Journal of Materials Science,* vol. 31, pp. 1-21, 1996.

[118] A. J. Ruys, "Silicon-doped hydroxyapatite," *Journal of the Australasian Ceramic Society,* vol. 29, pp. 71-80, 1993.

[119] L. Boyer, J. Carpena, and J. L. Lacout, "Synthesis of phosphate-silicate apatites at atomspheric pressure," *Solid State Ionics,* vol. 95, pp. 121-129, 1997.

[120] A. Ślósarczyk, Z. Paszkiewicz, and C. Paluszkiewicz, "FTIR and XRD evaluation of carbonated hydroxyapatite powders synthesized by wet methods," *Journal of Molecular Structure,* vol. 744-747, pp. 657-661, 2005.

[121] G. Penel, G. Leroy, C. Rey, and E. Bres, "MicroRaman spectral study of the PO_4 and CO_3 vibrational modes in synthetic and biological apatites," *Calcified Tissue International,* vol. 63, pp. 475-481, 1998.

[122] J. Elliott, D. Holcomb, and R. Young, "Infrared determination of the degree of substitution of hydroxyl by carbonate ions in human dental enamel," *Calcified Tissue International,* vol. 37, pp. 372-375, 1985.

[123] S. Barinov, J. Rau, S. Cesaro, J. Ďurišin, I. Fadeeva, D. Ferro, L. Medvecky, and G. Trionfetti, "Carbonate release from carbonated hydroxyapatite in the wide temperature rage," *Journal of Materials Science: Materials in Medicine,* vol. 17, pp. 597-604, 2006.

[124] R. Z. Legeros, O. R. Trautz, J. P. Legeros, E. Klein, and W. P. Shirra, "Apatite crystallites: effects of carbonate on morphology," *Science,* vol. 155, pp. 1409-1411, 1967.

[125] I. Atsuo, O. Kenji, N. Hiroshi, I. Noboru, and T. Tetsuya, "Preparation, solubility, and cytocompatibility of zinc-releasing calcium phosphate ceramics," *Journal of Biomedical Materials Research,* vol. 50, pp. 178-183, 2000.

[126] E. Fujii, M. Ohkubo, K. Tsuru, S. Hayakawa, A. Osaka, K. Kawabata, C. Bonhomme, and F. Babonneau, "Selective protein adsorption property and characterization of nano-crystalline zinc-containing hydroxyapatite," *Acta*

Biomaterialia, vol. 2, pp. 69-74, 2006.

[127] K. Matsunaga, "First-principles study of substitutional magnesium and zinc in hydroxyapatite and octacalcium phosphate," *The Journal of Chemical Physics,* vol. 128, pp. 245101-10, 2008.

[128] Y. Tang, H. F. Chappell, M. T. Dove, R. J. Reeder, and Y. J. Lee, "Zinc incorporation into hydroxylapatite," *Biomaterials,* vol. 30, pp. 2864-2872, 2009.

[129] A. Bigi, G. Falini, E. Foresti, M. Gazzano, A. Ripmonti, and N. Roveri, "Rietveld structure refinements of calcium hydroxylapatite containing magnesium," *Acta Crystallographica Section B,* vol. 52, pp. 87-92, 1996.

[130] Z. Y. Li, W. M. Lam, C. Yang, B. Xu, G. X. Ni, S. A. Abbah, K. M. C. Cheung, K. D. K. Luk, and W. W. Lu, "Chemical composition, crystal size and lattice structural changes after incorporation of strontium into biomimetic apatite," *Biomaterials,* vol. 28, pp. 1452-1460, 2007.

[131] M. Kikuchi, A. Yamazaki, R. Otsuka, M. Akao, and H. Aoki, "Crystal structure of Sr-substituted hydroxyapatite synthesized by hydrothermal method," *Journal of Solid State Chemistry,* vol. 113, pp. 373-378, 1994.

[132] J. Terra, E. R. Dourado, J. G. Eon, D. E. Ellis, G. Gonzalez, and A. M. Rossi, "The structure of strontium-doped hydroxyapatite: an experimental and theoretical study," *Physical Chemistry Chemical Physics,* vol. 11, pp. 568-577, 2009.

[133] T. Leventouri, C. E. Bunaciu, and V. Perdikatsis, "Neutron powder diffraction studies of silicon-substituted hydroxyapatite," *Biomaterials,* vol. 24, pp. 4205-4211, 2003.

[134] E. P. Alexandra, M. B. Serena, and B. William, "Ultrastructural comparison of

hydroxyapatite and silicon-substituted hydroxyapatite for biomedical applications," *Journal of Biomedical Materials Research Part A,* vol. 68A, pp. 133-141, 2004.

[135] R. Astala, L. Calderin, X. Yin, and M. J. Stott, "Ab initio simulation of Si-doped hydroxyapatite," *Chemistry of Materials,* vol. 18, pp. 413-422, 2005.

[136] R. Z. LeGeros, O. R. Trautz, E. Klein, and J. P. LeGeros, "Two types of carbonate substitution in the apatite structure," *Cellular and Molecular Life Sciences,* vol. 25, pp. 5-7, 1969.

[137] O. V. Frank-Kamenetskaya, "Structure, chemistry and synthesis of carbonate apatites — the main components of dental and bone tissues," in *Minerals as Advanced Materials I*, 2008, pp. 241-252.

[138] R. T. Otto, "X-ray diffraction of biological and synthetic apatites*," *Annals of the New York Academy of Sciences,* vol. 60, pp. 696-712, 1955.

[139] R. Legros, N. Balmain, and G. Bonel, "Structure and composition of the mineral phase of periosteal bone," *Journal of Chemical Research,* pp. 8-9, 1986.

[140] K. Beshah, C. Rey, M. J. Glimcher, M. Schimizu, and R. G. Griffin, "Solid state carbon-13 and proton NMR studies of carbonate-containing calcium phosphates and enamel," *Journal of Solid State Chemistry,* vol. 84, pp. 71-81, 1990.

[141] E. I. Hamilton, M. J. Minski, and J. J. Cleary, "The concentration and distribution of some stable elements in healthy human tissues from the United Kingdom. An environmental study," *Science of the Total Environment* vol. 1, pp. 341-374, 1973.

[142] M. Rercival, *Appl. Nutr. Sci. Rep,* vol. 5, p. 1, 1999.

[143] S. P. Nielsen, "The biological role of strontium," *Bone,* vol. 35, pp. 583-588,

2004.

[144] K. Schwarz, "A bound form of silicon in glycosaminoglycans and polyuronides," *Proceedings of the National Academy of Sciences USA,* vol. 70, pp. 1608-1612, 1973.

[145] E. M. Carlisle, "Silicon: a possible factor in bone calcification," *Science,* vol. 167, pp. 279-280, 1970.

[146] K. Schwarz and D. B. Milne, "Growth-promoting effects of silicon in rats," *Nature,* vol. 239, pp. 333 - 334, 1972.

[147] B. D. Cullity and S. R. Stock, *Elements of X-ray diffraction*, 3rd Edition ed.: Prentice Hall, 2001.

[148] I. Mobasherpour, M. S. Heshajin, A. Kazemzadeh, and M. Zakeri, "Synthesis of nanocrystalline hydroxyapatite by using precipitation method," *Journal of Alloys and Compounds,* vol. 430, pp. 330-333, 2007.

[149] S. W. K. Kweh, K. A. Khor, and P. Cheang, "The production and characterization of hydroxyapatite powders," *Journal of Materials Processing Technology,* vol. 89-90, pp. 373-377, 1999.

[150] M. H. Fathi and A. Hanifi, "Evaluation and characterization of nanostructure hydroxyapatite powder prepared by simple sol-gel method," *Materials Letters,* vol. 61, pp. 3978-3983, 2007.

[151] A. Siddharthan, S. K. Seshadri, and T. S. Sampath Kumar, "Rapid synthesis of calcium deficient hydroxyapatite nanoparticles by microwave irradiation," *Trends in Biomaterials and Artificial Organs* vol. 18, pp. 110-113, 2005.

[152] S. Raynaud, E. Champion, D. Bernache-Assollant, and P. Thomas, "Calcium phosphate apatites with variable Ca/P atomic ratio I. Synthesis, characterisation and thermal stability of powders," *Biomaterials,* vol. 23, pp. 1065-1072, 2002.

[153] M. R. Saeri, A. Afshar, M. Ghorbani, N. Ehsani, and C. C. Sorrell, "The wet precipitation process of hydroxyapatite," *Materials Letters,* vol. 57, pp. 4064-4069, 2003.

[154] D. L. Shi, "Temperature effect on bioactivity," in *Intoduction to biomaterials*, D. L. Shi, Ed.: Tsinghua Univeristy Press, 2006, p. 103.

[155] A. Thackray, R. Sammons, L. Macaskie, P. Yong, H. Lugg, and P. Marquis, "Bacterial biosynthesis of a calcium phosphate bone-substitute material," *Journal of Materials Science: Materials in Medicine,* vol. 15, pp. 403-406, 2004.

[156] R. L. Sammons, A. C. Thackray, H. M. Ledo, P. M. Marquis, I. P. Jones, P. Yong, and L. E. Macaskie, "Characterisation and sintering of nanophase hydroxyapatite synthesised by a species of Serratia," *Journal of Physics: Conference Series,* vol. 93, pp. 1-7, 2007.

[157] T. Furuzono, D. Walsh, K. Sato, K. Sonoda, and J. Tanaka, "Effect of reaction temperature on the morphology and size of hydroxyapatite nanoparticles in an emulsion system," *Journal of Materials Science Letters,* vol. 20, pp. 111-114, 2001.

[158] M. Palard, E. Champion, and S. Foucaud, "Synthesis of silicated hydroxyapatite $Ca_{10}(PO_4)_{6-x}(SiO_4)_x(OH)_{2-x}$," *Journal of Solid State Chemistry,* vol. 181, pp. 1950-1960, 2008.

[159] Z. Li, P. Wang, and Z. Wu, "Preparation of nanosized hydroxyapatite particles at low temperatures," *Journal of Materials Science,* vol. 40, pp. 6589-6591, 2005.

[160] J. P. Lafon, E. Champion, and D. Bernache-Assollant, "Processing of AB-type carbonated hydroxyapatite $Ca_{10-x}(PO_4)_{6-x}(CO_3)_x(OH)_{2-x-2y}(CO_3)_y$ ceramics with controlled composition," *Journal of the European Ceramic Society,* vol. 28, pp.

139-147, 2008.

[161] S. Kannan, I. A. F. Lemos, J. H. G. Rocha, and J. M. F. Ferreira, "Synthesis and characterization of magnesium substituted biphasic mixtures of controlled hydroxyapatite/β-tricalcium phosphate ratios," *Journal of Solid State Chemistry,* vol. 178, pp. 3190-3196, 2005.

[162] J. C. Heughebaert, in *Insititut national polytechnique* Toulouse, 1977.

[163] R. Smith and I. Rehman, "Fourier transform Raman spectroscopic studies of human bone," *Journal of Materials Science: Materials in Medicine,* vol. 5, pp. 775-778, 1994.

[164] M. Nishino, S. Yamashita, T. Aoba, M. Okazaki, and Y. Moriwaki, "The Laser-Raman spectroscopic studies on human enamel and precipitated carbonate-containing apatites," *Journal of Dental Research,* vol. 60, pp. 751-755, 1981.

[165] P. N. de Aza, C. Santos, A. Pazo, S. de Aza, R. Cusco, and L. Artus, "Vibrational properties of calcium phosphate compounds. 1. Raman spectrum of β-Tricalcium Phosphate," *Chemistry of Materials,* vol. 9, pp. 912-915, 1997.

[166] S. Dorozhkin, "A hierarchical structure for apatite crystals," *Journal of Materials Science: Materials in Medicine,* vol. 18, pp. 363-366, 2007.

[167] J. L. Miquel, L. Facchini, A. P. Legrand, C. Rey, and J. Lemaitre, "Solid state NMR to study calcium phosphate ceramics," *Colloids and Surfaces,* vol. 45, pp. 427-433, 1990.

[168] J. L. Miquel, L. Facchini, A. P. Legrand, X. Marchandise, P. Lecouffe, M. Chanavaz, M. Donazzan, C. Rey, and J. Lernaitre, "Characterisation and conversion study into natural living bone of calcium phosphate bioceramics by solid state NMR spectroscopy," *Clinical Materials,* vol. 5, pp. 115-125, 1990.

[169] C. Jäger, T. Welzel, W. Meyer-Zaika, and M. Epple, "A solid-state NMR investigation of the structure of nanocrystalline hydroxyapatite," *Magnetic Resonance in Chemistry,* vol. 44, pp. 573-580, 2006.

[170] W. Kolodziejski, "Solid-state NMR studies of bone," in *New Techniques in Solid-State NMR*, 2005, pp. 235-270.

[171] E. Landi, G. Logroscino, L. Proietti, A. Tampieri, M. Sandri, and S. Sprio, "Biomimetic Mg-substituted hydroxyapatite: from synthesis to in vivo behaviour," *Journal of Materials Science: Materials in Medicine,* vol. 19, pp. 239-247, 2008.

[172] L. W. Schroeder and M. Mathew, "Cation ordering in $Ca_2La_8(SiO_4)_6O_2$," *Journal of Solid State Chemistry,* vol. 26, pp. 383-387, 1978.

[173] S. Sprio, G. Pezzotti, G. Celotti, E. Landi, and A. Tampieri, "Raman and cathodoluminescence spectroscopies of magnesium-substituted hydroxyapatite powders," *Journal of Material Research,* vol. 20, pp. 1009-1016 2005.

[174] M. Braun, P. Hartmann, and C. Jana, "^{19}F and ^{31}P NMR spectroscopy of calcium apatites," *Journal of Materials Science: Materials in Medicine,* vol. 6, pp. 150-154, 1995.

[175] R. J. Kirkpatrick and R. K. Brow, "Nuclear magnetic resonance investigation of the structures of phosphate and phosphate-containing glasses: a review," *Solid State Nuclear Magnetic Resonance,* vol. 5, pp. 9-21, 1995.

[176] M. A. Aramendía, V. Borau, C. Jiménez, J. M. Marinas, F. J. Romero, and J. R. Ruiz, "XRD and solid-state NMR study of magnesium oxide-magnesium orthophosphate systems," *Journal of Solid State Chemistry,* vol. 135, pp. 96-102, 1998.

[177] W. Yaotang, M. J. Glimcher, C. Rey, and J. L. Ackerman, "A unique protonated

phosphate group in bone mineral not present in synthetic calcium phosphates," *Journal of Molecular Biology,* vol. 244, pp. 423-435, 1994.

[178] B. O. Fowler, "Infrared studies of apatites. I. Vibrational assignments for calcium, strontium, and barium hydroxyapatites utilizing isotopic substitution," *Inorganic Chemistry,* vol. 13, pp. 194-207, 2002.

[179] E. Landi, G. Celotti, G. Logroscino, and A. Tampieri, "Carbonated hydroxyapatite as bone substitute," *Journal of the European Ceramic Society,* vol. 23, pp. 2931-2937, 2003.

[180] J. V. Rau, S. N. Cesaro, D. Ferro, S. M. Barinov, and I. V. Fadeeva, "FTIR study of carbonate loss from carbonated apatites in the wide temperature range," *Journal of Biomedical Materials Research Part B: Applied Biomaterials,* vol. 71B, pp. 441-447, 2004.

[181] J. M. Parker and A. B. Seddon, "Infrared-transmitting optical fibres," in *High-performance glasses*, M. Cable and J. M. Parker, Eds. London: Blackie, 1992, pp. 252-286.

[182] J. Wu and J. F. Stebbins, "Effects of cation field strength on the structure of aluminoborosilicate glasses: high-resolution ^{11}B, ^{27}Al and ^{23}Na MAS NMR," *Journal of Non-Crystalline Solids,* vol. 355, pp. 556-562, 2009.

[183] N. Patel, S. M. Best, W. Bonfield, I. R. Gibson, K. A. Hing, E. Damien, and P. A. Revell, "A comparative study on the in vivo behavior of hydroxyapatite and silicon substituted hydroxyapatite granules," *Journal of Materials Science: Materials in Medicine,* vol. 13, pp. 1199-1206, 2002.

[184] C. M. Botelho, M. A. Lopes, I. R. Gibson, S. M. Best, and J. D. Santos, "Structural analysis of Si-substituted hydroxyapatite: zeta potential and X-ray photoelectron spectroscopy," *Journal of Materials Science: Materials in*

Medicine, vol. 13, pp. 1123-1127, 2002.

[185] S. Zou, J. Huang, S. Best, and W. Bonfield, "Crystal imperfection studies of pure and silicon substituted hydroxyapatite using Raman and XRD," *Journal of Materials Science: Materials in Medicine,* vol. 16, pp. 1143-1148, 2005.

[186] W. P. Aue, A. H. Roufosse, M. J. Glimcher, and R. G. Griffin, "Solid-state phosphorus-31 nuclear magnetic resonance studies of synthetic solid phases of calcium phosphate: potential models of bone mineral," *Biochemistry,* vol. 23, pp. 6110-6114, 2002.

[187] A. Yasukawa, K. Kandori, and T. Ishikawa, "TPD-TG-MS study of carbonate calcium hydroxyapatite particles," *Calcified Tissue International,* vol. 72, pp. 243-250, 2003.

[188] H. El Feki, C. Rey, and M. Vignoles, "Carbonate ions in apatites: infrared investigations in the v_4 CO_3 domain," *Calcified Tissue International,* vol. 49, pp. 269-274, 1991.

[189] N. V. Vagenas, A. Gatsouli, and C. G. Kontoyannis, "Quantitative analysis of synthetic calcium carbonate polymorphs using FT-IR spectroscopy," *Talanta,* vol. 59, pp. 831-836, 2003.

[190] M. Vignoles, G. Bonel, D. Holcomb, and R. Young, "Influence of preparation conditions on the composition of type B carbonated hydroxyapatite and on the localization of the carbonate ions," *Calcified Tissue International,* vol. 43, pp. 33-40, 1988.

[191] R. Murugan and S. Ramakrishna, "Production of ultra-fine bioresorbable carbonated hydroxyapatite," *Acta Biomaterialia,* vol. 2, pp. 201-206, 2006.

[192] H. Li, B. S. Ng, K. A. Khor, P. Cheang, and T. W. Clyne, "Raman spectroscopy determination of phases within thermal sprayed hydroxyapatite splats and

subsequent in vitro dissolution examination," *Acta Materialia,* vol. 52, pp. 445-453, 2004.

[193]   N. Koga, Y. Nakagoe, and H. Tanaka, "Crystallization of amorphous calcium carbonate," *Thermochimica Acta,* vol. 318, pp. 239-244, 1998.